TKK Dissertations 228
Espoo 2010

COMPUTATIONAL MODELING OF CATIONIC LIPID BILAYERS IN SALINE SOLUTIONS

Doctoral Dissertation

Markus Miettinen

Aalto University
School of Science and Technology
Faculty of Information and Natural Sciences
Department of Applied Physics

TKK Dissertations 228
Espoo 2010

COMPUTATIONAL MODELING OF CATIONIC LIPID BILAYERS IN SALINE SOLUTIONS

Doctoral Dissertation

Markus Miettinen

Doctoral dissertation for the degree of Doctor of Science in Technology to be presented with due permission of the Faculty of Information and Natural Sciences for public examination and debate in Auditorium K at the Aalto University School of Science and Technology (Espoo, Finland) on the 5th of June 2010 at 10 o'clock.

Aalto University
School of Science and Technology
Faculty of Information and Natural Sciences
Department of Applied Physics

Aalto-yliopisto
Teknillinen korkeakoulu
Informaatio- ja luonnontieteiden tiedekunta
Teknillisen fysiikan laitos

Distribution:
Aalto University
School of Science and Technology
Faculty of Information and Natural Sciences
Department of Applied Physics
P.O. Box 11100 (Otakaari 1 M)
FI - 00076 Aalto
FINLAND
URL: http://tfy.tkk.fi/
Tel. +358-9-470 23101
Fax +358-9-470 23155
E-mail: Eija.Jarvinen@tkk.fi

ISBN 978-952-60-3193-4
ISBN 978-952-60-3194-1 (PDF)
ISSN 1795-2239
ISSN 1795-4584 (PDF)
URL: http://lib.tkk.fi/Diss/2010/isbn9789526031941/

TKK-DISS-2768

Paino Pärnäset Oy
Espoo 2010

Aalto University

ABSTRACT OF DOCTORAL DISSERTATION	AALTO UNIVERSITY SCHOOL OF SCIENCE AND TECHNOLOGY P.O. BOX 11000, FI-00076 AALTO http://www.aalto.fi

Author Markus Miettinen

Name of the dissertation

Computational modeling of cationic lipid bilayers in saline solutions

Manuscript submitted January 25th 2010	Manuscript revised April 26th 2010
Date of the defence June 5th 2010	
☒ Monograph	☐ Article dissertation (summary + original articles)
Faculty	Faculty of Information and Natural Sciences
Department	Department of Applied Physics
Field of research	F039Z Engineering Physics, Theoretical and Computational Physics
Opponent(s)	Univ.-Doz. Dr. Georg Pabst (pre-examiners prof. Roland Faller and prof. Amadeu Sum)
Supervisor	Prof. Risto Nieminen
Instructor	Prof. Mikko Karttunen

Abstract

Based on computer simulations performed at single-molecule resolution, the effects of monovalent NaCl salt on cationic DMTAP/DMPC (dimyristoyltrimethylammoniumpropane/dimyristoylphosphatidylcholine) lipid bilayer systems are discussed. The monograph reviews, revises and expands the previously published work on how NaCl affects the structural and electrostatic [1] and the dynamic [2] properties of these systems.

The effects of NaCl depended qualitatively on the cationic DMTAP lipid fraction. When the fraction was low, NaCl had a notable effect of the structural properties of the bilayer, decreasing the area per lipid, increasing the tail order, reorienting the DMPC head groups, and increasing the average electrostatic potential difference over the head group region. At high DMTAP fraction there was scarcely an effect when NaCl was added.

The reason for this dichotomy was the ability of the Na^+ ions to bind with the DMPC lipid carbonyl oxygens at low DMTAP fraction and to tie 2 to 4 DMPCs into a dynamic complex. At high DMTAP fraction the binding of Na^+ was prevented by the high positive surface charge of the bilayer.

The lateral diffusion of Na^+ ions within the carbonyl region had two qualitatively different modes. Na^+ ions bound to a DMPC diffused very slowly, whereas the free Na^+ ions traveled rapidly within the carbonyl region. The combined effect of the two motions appeared as Na^+ ions hopping from one DMPC carbonyl oxygen to the next.

[1] A. A. Gurtovenko, M. S. Miettinen, M. Karttunen, and I. Vattulainen.
Effects of monovalent salt on cationic lipid membranes as revealed by molecular dynamics simulations.
J. Phys. Chem. B, 109: 21126–34 (2005).

[2] M. S. Miettinen, A. A. Gurtovenko, I. Vattulainen, and M. Karttunen.
Ion dynamics in cationic lipid bilayer systems in saline solutions.
J. Phys. Chem. B, 113: 9226–34 (2009).

Keywords	cationic lipid, DMTAP, DMPC, bilayer, NaCl, molecular dynamics, ion dynamics		
ISBN (printed)	ISBN 978-952-60-3193-4	ISSN (printed)	ISSN 1795-2239
ISBN (pdf)	ISBN 978-952-60-3194-1	ISSN (pdf)	ISSN 1795-4584
Language	English	Number of pages	97
Publisher	Markus Miettinen		
Print distribution	Department of Applied Physics, P.O. Box 11100 (Otakaari 1 M), FI–00076 Aalto, Finland		
☒ The dissertation can be read at http://lib.tkk.fi/Diss/2010/isbn9789526031941			

Aalto-yliopisto

VÄITÖSKIRJAN TIIVISTELMÄ	AALTO-YLIOPISTO TEKNILLINEN KORKEAKOULU PL 11000, 00076 AALTO http://www.aalto.fi

Tekijä Markus Miettinen

Väitöskirjan nimi

Computational modeling of cationic lipid bilayers in saline solutions

Käsikirjoituksen päivämäärä 25. tammikuuta 2010	Korjatun käsikirjoituksen päivämäärä 26. huhtikuuta
Väitöstilaisuuden ajankohta 5. kesäkuuta 2010	
☒ Monografia	☐ Yhdistelmäväitöskirja (yhteenveto + erillisartikkelit)
Tiedekunta	Informaatio- ja luonnontieteiden tiedekunta
Laitos	Teknillisen fysiikan laitos
Tutkimusala	F039Z Teknillinen fysiikka, teoreettinen ja laskennallinen fysiikka
Vastaväittäjä(t)	Univ.-Doz. Dr. Georg Pabst (esitarkastajat prof. Roland Faller ja prof. Amadeu Sum)
Työn valvoja	Prof. Risto Nieminen
Työn ohjaaja	Prof. Mikko Karttunen

Tiivistelmä

Ruokasuolan (NaCl) vaikutusta positiivisesti varattuihin DMTAP/DMPC (dimyristyylitrimetyyliammonium-propaani/dimyristyylifosfatidyylikoliini) lipidikaksoiskerroksiin tutkittiin yksittäisten atomien erottelutarkkuudella suoritettujen tietokonesimulaatioiden avulla. Väitöskirja läpikäy, tarkentaa ja laajentaa aiempia julkaisujamme ruokasuolan aiheuttamista rakenteellisista ja sähköstaattisista [1] sekä dynaamisista [2] muutoksista.

Ruokasuolan vaikutukset riippuivat vahvasti kationisen DMTAP-lipidin määrästä kaksoiskerroksessa. Määrän ollessa vähäinen NaCl muutti selvästi kaksoiskerroksen rakennetta: lipidikohtainen ala kutistui, hännät järjestyivät, DMPC-lipidin pääryhmät pyrkivät poispäin kalvosta ja sähköinen jännite pääryhmien yli lisääntyi. Määrän ollessa suuri vaikutusta ei juurikaan ollut.

Tämä kahtiajakoisuus johtui Na^+-ionien kyvystä sitoutua sähköstaattisesti DMPC-lipidien karbonyylihappiin (kiinnittäen kahdesta neljään DMPC:tä toisiinsa), kun DMTAP-osuus kaksoiskerroksessa oli pieni. Korkeilla DMTAP-pitoisuuksilla kalvon suuri positiivinen pintavaraus esti natriumin sitoutumisen.

Na^+-ionien diffuusio kalvon pinnassa koostui kahdesta hyvin erilaisesta liikkeestä. Lipideihin sitoutuneet ionit diffuntoituivat hyvin hitaasti, kun taas karbonyylialueen sitoutumattomat ionit etenivät erittäin nopeasti. Näiden kahden yhdistelmänä Na^+-ionien liike oli kuin levotonta hypähtelyä yhden DMPC-lipidin karbonyylihapesta seuraavaan.

[1] A. A. Gurtovenko, M. S. Miettinen, M. Karttunen, and I. Vattulainen.
Effects of monovalent salt on cationic lipid membranes as revealed by molecular dynamics simulations.
J. Phys. Chem. B, 109: 21126–34 (2005).

[2] M. S. Miettinen, A. A. Gurtovenko, I. Vattulainen, and M. Karttunen.
Ion dynamics in cationic lipid bilayer systems in saline solutions.
J. Phys. Chem. B, 113: 9226–34 (2009).

Asiasanat kationinen lipidi, DMTAP, DMPC, NaCl, molekyylidynamiikka, ionien dynamiikka	
ISBN (painettu) ISBN 978-952-60-3193-4	ISSN (painettu) ISSN 1795-2239
ISBN (pdf) ISBN 978-952-60-3194-1	ISSN (pdf) ISSN 1795-4584
Kieli englanti	Sivumäärä 97
Julkaisija Markus Miettinen	
Painetun väitöskirjan jakelu Teknillisen fysiikan laitos, PL 11100 (Otakaari 1 M), FI–00076 Aalto	
☒ Luettavissa verkossa osoitteessa http://lib.tkk.fi/Diss/2010/isbn9789526031941	

Statement of contribution

The author has played an active role in all stages of the research reported in this thesis.

Concerning the structural properties, reported in Sec. 4.1, the author took part in the data analysis for the original publication [1], done together with Andrey Gurtovenko, Ilpo Vattulainen, and Mikko Karttunen. The main author for the publication was Andrey Gurtovenko, who ran the simulations and was chiefly responsible for planning the study, writing the publication, as well as the analysis.

For the thesis, however, the author reproduced with a larger data set almost all the analysis of the original publication [1] as well as performed analysis of additional properties. For this he wrote his own analysis codes and conducted the analysis. On the basis of the analysis he substantially expanded and revised the results of the original publication [1].

Concerning the dynamical properties, reported in Sec. 4.2, the author carried out the simulations, planned the analysis, wrote the analysis codes, performed the analysis and principally wrote the publication [2], done together with Andrey Gurtovenko, Ilpo Vattulainen, and Mikko Karttunen. In the thesis, this work is presented in a slightly expanded form.

Tytöilleni Tuijalle, Pörrölle ja Hellälle

Foreword

The research I present in this thesis has been carried out in the Helsinki University of Technology during 2004–2009. During these years I have worked at two laboratories. I started at the Laboratory of Computational Engineering as a member of the Biophysics and Statistical Mechanics Group lead by academy research fellow Mikko Karttunen. When Mikko obtained his professorship in the University of Western Ontario in Canada at the end of 2005, I was relocated to the Laboratory of Physics and became a member of the Biological and Soft Matter Group there — but Mikko still remained my instructor.

I am thankful to Mikko for his support over the years, and in particular for his hospitality during my three long-term visits to London, Ontario. During those trips we ran hundreds of kilometers together, discussing science among other important aspects of life.

I wish to thank my initial supervisor, professor Kimmo Kaski, for encouraging me to move to the Laboratory of Physics; my deepest gratitude goes to my final supervisor, professor Risto Nieminen, as well as to the head of the Biological and Soft Matter Group, professor Ilpo Vattulainen, for their help during that transition.

With regards to work presented in this thesis, there is one person I wish to thank more than anyone else: Dr. Andrey Gurtovenko, who kindly welcomed me to take part in his cationic lipid simulation project, and who patiently waited for the publication concerning the dynamical aspects to find its final form.

With pleasure I acknowledge the importance of the continuous financial support from the National Graduate School in Materials Physics, as well as of the grants from the Finnish Academy of Science and Letters, the Finnish Cultural Foundation, the Finnish Foundation for Technology Promotion, the Magnus Ehrnrooth Foundation, and the HPC-Europa Transnational Access Program. I would also like to thank the computing resources provided by the Finnish IT Center for Science and the HorseShoe supercluster at the University of Southern Denmark.

I thank the pre-examiners of this thesis, professors Roland Faller and Amadeu Sum for their comments and encouragement. Also, I am thankful to Dr. Georg Pabst for accepting to act as my opponent.

For all the delightful discussions, beers and joy we have had, I would like to thank all my coworkers and colleagues around the globe: Alex, Andrew, Artturi, Ben, Cristiano, Emma, Emma, Emppu, Giulia, Halim, Hanne, Hector, Jaakko, Jarkko, Jason, Jelena, Jirasak, Jukka, Julia, Lei, Liam, Lorna, Luca, Marco, Maria, Marja, Marko, Martin, Matti, Michael, Mohsen, Niloufar, Olli, Pawel, Perttu, Peter, Petri, Praveen, Ramin, Razvan, Riku, Sami, Samuli, Sanja, Sarah, Sebastian, Sigga, Susanna, Suvi, Teemu, Tomek, Ville, Wei, Xiang,... and you, if you scan through the list and can not find your name despite you think it ought to be there. I was certain I forgot someone. Please punch me. Oh, and I thank Eija Järvinen for all the help and humor over the years. She has tough knuckles, I do not want to be punched by her.

I am very grateful to all my folks outside the scientific circles for providing an invaluable counterbalance to my work: Aila, Antti, Amande, Ari, Eero, Frank, Hanna, Heikki, Ilkka, Jaakko, Jay, Jari, Johannes, Juha, Jukka, Jussi, Jyry XL basketball, Kari, Lelia, Lumi, Margus, Marianne, Micaela, Mikko, Nisäkkäät floorball, Olli-Pekka, Pauli, Pekka, Sami, Sisu, Stefe, Taina, Taneli, Tapio, Teemu, Teemu, Tommi, Toni, Tuomas, Turo, Ukri, Veera, Vesa, Ville, Ville, Ville, Visa,... did I miss one Ville?

In particular, I want to express my deepest gratitude and respect to my mother, father, and sister, who have supported and understood me throughout my life. I feel privileged to be part of our family.

Finally, and most importantly, thank you Tuija for your unceasing love, appreciation and encouragement.

Berlin May 17, 2010

Markus Miettinen

Contents

Chapter 1

Overview

In this thesis we study lipid membranes at single-molecule resolution using computer simulations, a rapidly developing scientific tool between experiments and theory (Fig. 1.1). Despite its power of opening a window from which to view the structural and dynamic features of a given molecular system, the simulational approach is by no means self-contained. Let us use Fig. 1.1 to position the present work among other possible[1] related scientific activities.

The **real system** here is a particular lipid membrane under physiological conditions. In more detail, a cationic DMTAP/DMPC (dimyristoyltrimethylammoniumpropane/dimyristoylphosphatidylcholine) bilayer. Seldom is the real system such that it can be directly assessed experimentally, but some controlled modifications are required when **designing experiments**. Experimental setups may, for example, involve using a supported membrane or a monolayer, or pressures, temperatures and buffer solutions outside the physiological range. **Performing experiments** (calorimetry, X-ray and neutron diffraction, nuclear magnetic resonance, single particle tracking, fluorescence correlation spectroscopy, atomic force microscopy, . . .) on these modified systems provides **experimental results**: phase transition temperatures, average areas occupied per lipid, evidence on lipid head group orientations, estimates of lipid lateral diffusion coeffiecients, images of possible lipid–ion complexes, . . .

To go beyond mere data collecting, theoretical constructs capable of explaining the observed data and predicting possible unforeseen features of the real system are created,

[1] A feature missing on Fig. 1.1 is the motivation for the study. Science does not necessarily need external incentives. Curiosity is enough. It is, however, delightful to know that detailed understanding of positively charged lipid bilayers is of practical biomedical interest due to their applicability in gene and drug delivery.

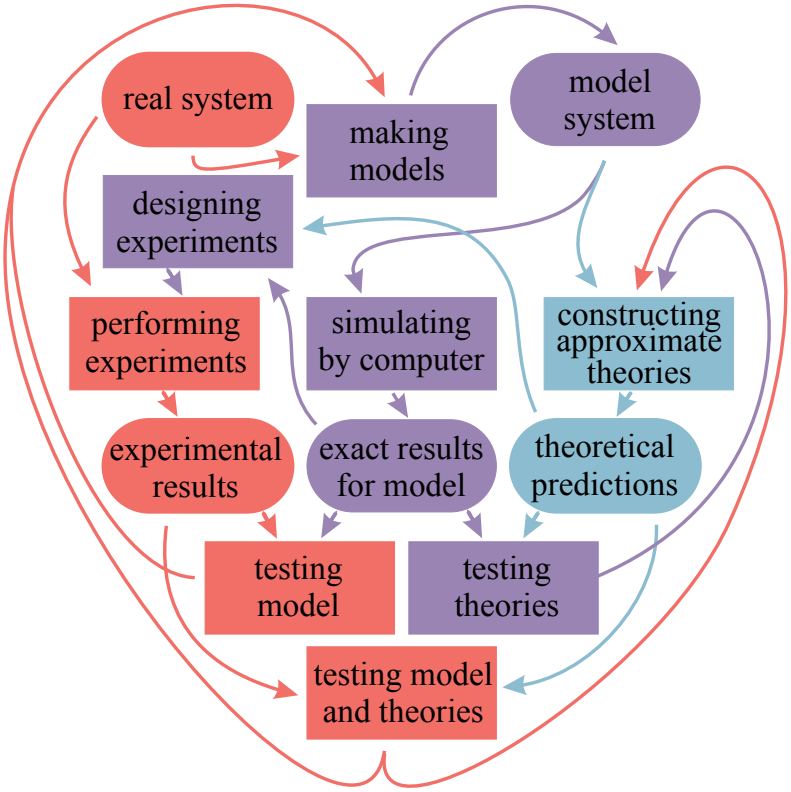

Figure 1.1: The role of computer simulations in the process of natural sciences.

making models based on the real system and possible earlier models, theories, and experiments. An infinite bilayer of DMTAP and DMPC lipids surrounded with water molecules and Na^+ and Cl^- ions is our **model system**. It is still too complex to be worked out on pen and paper, for which further **theoretical approximations** are needed. Representing the charged bilayer as a smooth impenetrable wall with constant surface charge density and assuming the surrounding ions to be point-like and uncorrelated, the system can be solved analytically to produce **theoretical predictions** of the electrostatic potential profiles and ion distributions surrounding the lipid bilayer.

By the immense growth in computational power during the last few decades, an alternative route on studying the model system has surfaced. **Simulating by computer** it is possible to study a model system comprising DMTAP and DMPC lipids, water molecules and ions, all described in full molecular detail, and to produce **exact results for the model**. This allows for separately **testing model** and **testing theories**, because properties measurable experimentally (area per lipid, head group orientiation, ...) as well as theoretical predictions (potential profiles, ion distributions, ...) can be calculated from the simulation. In addition, it is possible to study exactly the molecular mechanisms of the phenomenon of interest, "to see inside the sample", and to validate interpretations of experiments. All this is the subject of the present work. The structure of the rest of the thesis is as follows.

Chapter 2 provides background on lipid membranes, starting from general subjects such as their importance as biological structures and going to rather detailed topics such as ways of characterizing the electrostatic properties of charged membrane systems.

Chapter 3 reviews the main aspects of the research method used in this work, the molecular dynamics simulations, and describes the particular model parameters employed.

Chapter 4 presents and discusses the results of the molecular dynamics simulations performed. It comprises two sections, each based on work previously published in peer-reviewed journals. Section 4.1 discusses the structural [1] and Sec. 4.2 the dynamical [2] properties of the lipid bilayer system under study. Almost all the results presented in the Section 4.1 have been, however, reanalyzed from the currently available data, which is considerably more extensive than in the original publication [1], and some of the results have gone through even qualitative changes. The discussion of electrostatic properties, in particular, has been thoroughly revised.

Chapter 5 ends the thesis to a summary and conclusions.

Chapter 2

Background on lipid membranes

A general understanding of the system under study is needed to successfully set up, perform and analyze any simulation (Fig. 1.1). To this end, this chapter aims to review the most relevant features of lipid membranes systems.

Firstly, Sec. 2.1 sets the stage by discussing biological matter in general and the prevalence of lipid bilayers in it. Section 2.2 then focuses on describing the lipids themselves, after which Sec. 2.3 discusses the superstructures formed of lipid building blocks, mainly focusing on their bilayers. Finally, Sec. 2.4 strives to explain what is so special about cationic membrane systems.

2.1 Biological matter

Let us make a thought experiment. Take a random specimen that you think would qualify as biological matter: a flower, a rat, an ant, a bacterium, a thyme leaf, a spleen, a shark, an elephant's trunk, a spruce. Or take a human. Then do what a physicist loves to do. Simplify. Try to find the essence of the specimen; make a zeroth order approximation.

You will come to the conclusion that you are studying, at the face of it, water (Fig. 2.1).

Clearly H_2O, with its two hydrogens and one oxygen (Fig. 2.2), is The Biomolecule. It is fascinating how something so seemingly simple can give rise to such a broad palette of exceptional material properties. Water expands when it solidifies. It is densest at 4 K above the freezing point. The freezing and boiling points, heat capacity, relative

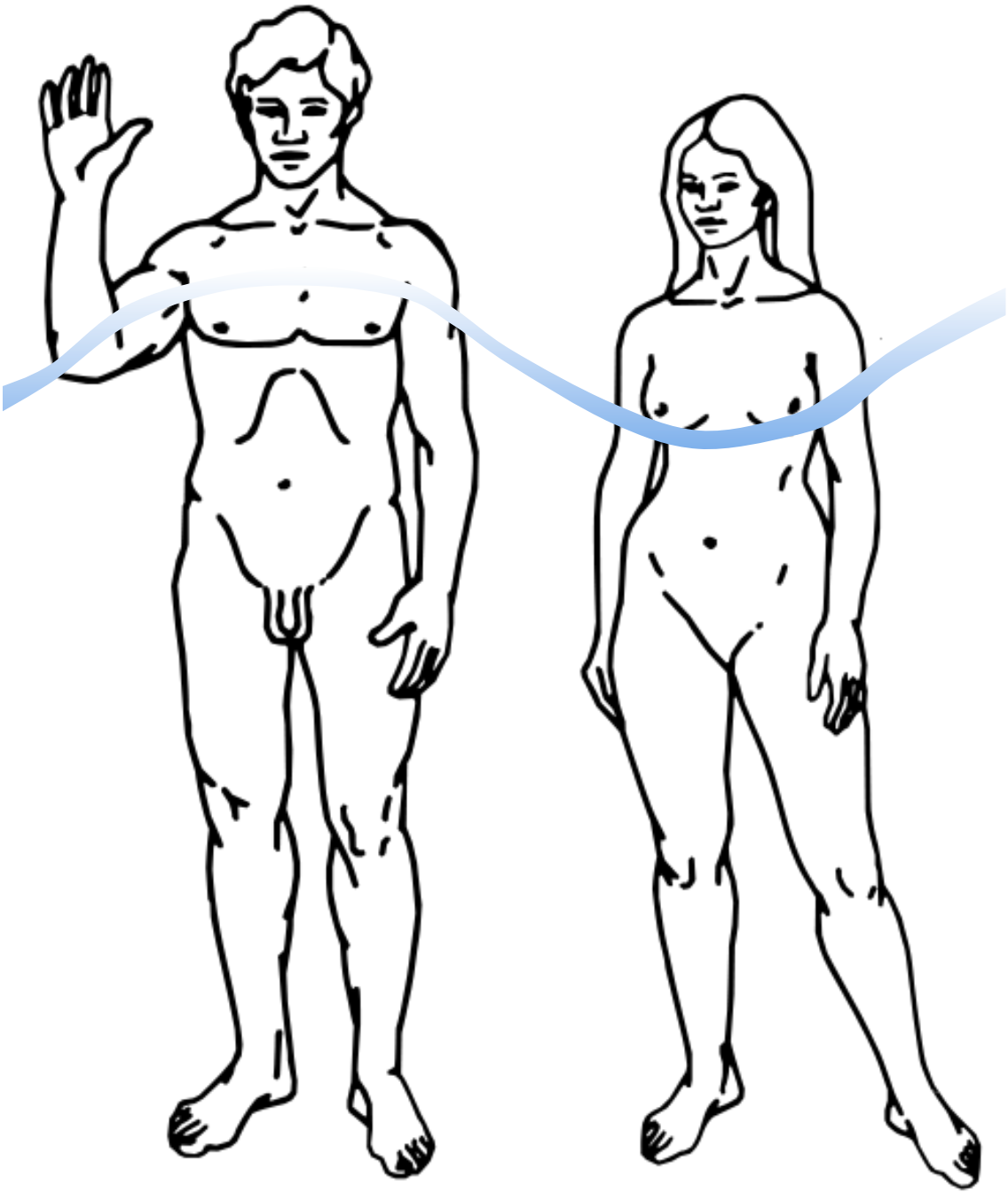

Figure 2.1: More than half (as roughly illustrated by the wavy line) of human body weight is water. The male and female figures as pictured on the Pioneer 11 plate by NASA [3].

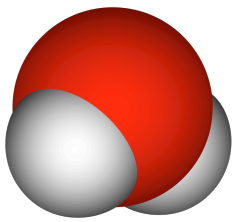

Figure 2.2: A water molecule. Oxygen in red, hydrogens in white. [3]

permittivity and surface tension are abnormally high. The viscosity is odd. And this is just a start of a list of dozens of peculiriaties, many of which are crucial to life as we know it [4, 5].

And yet, despite the importance and seeming simplicity, there still exists no molecular model that could properly describe water [6]. In fact, even the structure of liquid water is still under debate [7, 8] and considered to be one of the most outstanding problems in science [9]. We often rationalize the observed features of water by the polarity, small size and asymmetric shape of H_2O—and above all by its ability to partake in four hydrogen bonds leading to a tetrahedral network [10]—but still, as Philip Ball [11] brutally puts it: "No one really understands water."

But although water is intriguing and we do not fully understand it, it is still far from the whole story when it comes to biological matter. As often happens, the zeroth order approximation does provide an exciting angle on the system, but misses all those features that we wished to understand. Clearly biological matter is inhomogeneous and anisotropic matter, and characterized by structure and organization at many levels. If we allow a bit more terms in our imaginary expansion, we will see that all the examples above comprise cells. And the cells themselves are filled with structure of their own, most of which is made of membranes (Fig. 2.3).

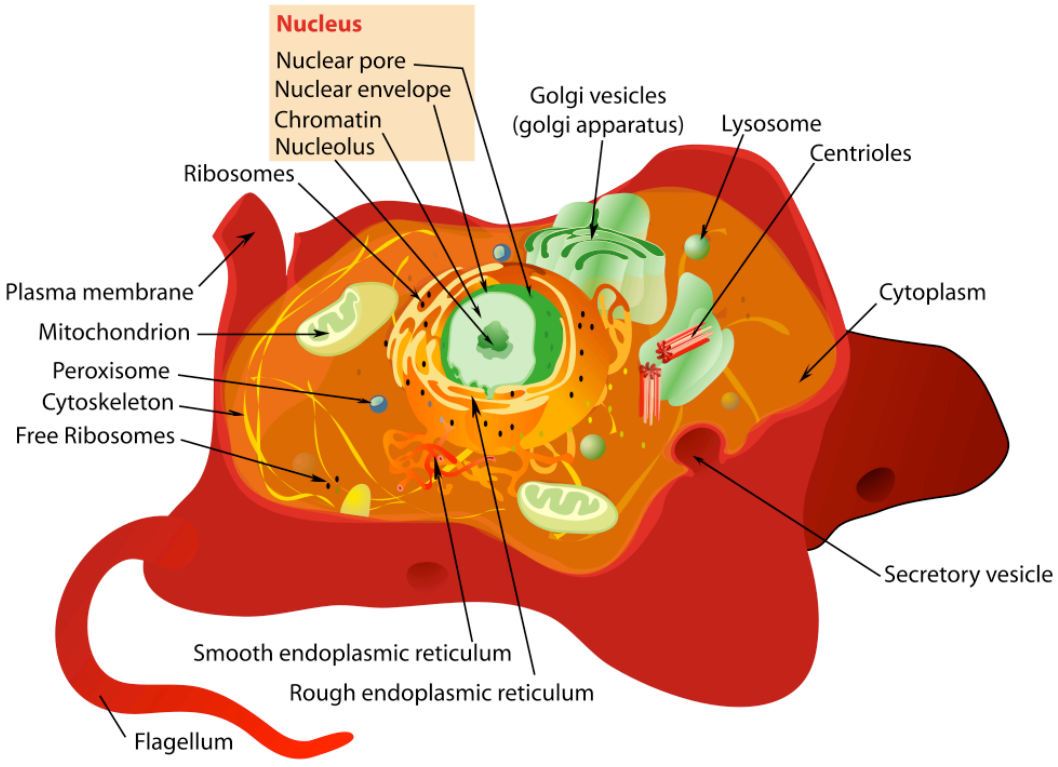

Figure 2.3: Animal cell. Cartoon by Mariana Ruiz Villarreal. [3]

Membranes enclose the cell and bind many of its organelles. In addition to this structural function, they serve as platforms for intracellular processes and as pathways for molecular traffic and signaling. Let us quickly go through some of the most important membranes in an animal cell and their main functions.

The double membrane of the nuclear envelope isolates the genetic material, kept in the nucleus, from the cellular cytoplasm. Its outer membrane continues as the endoplasmic reticulum, forming an extensive maze of interconnected tubules and vesicles, held together by the cytoskeleton. Part of the endoplasmic reticulum has a "rough" appearance; this is caused by the ribosomes, the cell's protein factories, which attach to the rough endoplasmic reticulum during protein translation. The smooth endoplasmic reticulum is the main site for lipid synthesis [12]. The nascent proteins and lipids are then transported in vesicles to the Golgi apparatus for final modifications before continuing in vesicles to their target destinations. After having served their purpose, they are recycled in the lysosomes, vesicles bound by a single membrane and filled with degradative enzymes. Energy for the cell is produced at the tightly folded inner membrane of the mitochondria.

The cell membrane (Fig. 2.4) forms a barrier that safeguards the contents of the cell from the surroundings. Its core, like the core of all biomembranes, is formed by a phospholipid bilayer. Into this core various proteins of differing biological functions (transporters, receptors, enzymes) are attached and embedded. The third main component of biomembranes, the carbohydrates, are attached to the proteins and lipids.

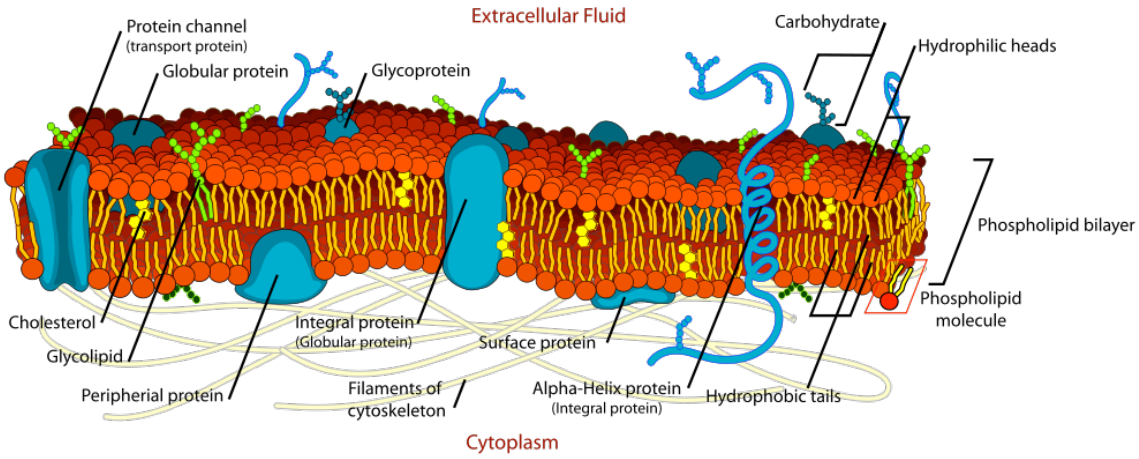

Figure 2.4: Plasma membrane. Cartoon by Mariana Ruiz Villarreal. [3]

The physical properties of the membrane are quite amazing. It is very flexible. Even better, it can seal itself if ruptured. And despite all its moldability it is a very efficient permeability barrier to ions and other molecular substances. These intuitively contrasting

abilities are not provided by the carbohydrates, nor the proteins, but by the lipid bilayer core, a self-organized superstructure of uncountable numbers of lipid molecules. Let us next study in more detail these clever soft bricks comprising the foundations of all biomembranes, the lipids.

2.2 Lipids

In addition to forming cellular structures (Fig. 2.4), naturally occurring lipids function as energy storage as well as signaling devices. It is not trivial to list the necessary and sufficient conditions for a molecule to be a lipid. They form a diverse group, and trying to catch all the exceptions one is quickly knee-deep in technicalities. For us a description of their typical properties suffices.

Lipids are small. At least when compared to DNA and proteins, the two other key biological macromolecules. A typical biolipid weighs $\lesssim 1$ kDa and in its common conformation fits into a cylinder that has diameter $\lesssim 1$ nm and height $\gtrsim 1$ nm.

Lipids have a hydrophobic (nonpolar) part, archetypically composed of (hydrocarbon) chains commonly called tails. In addition, they can have a hydrophilic (polar) part, commonly called a head. Figure 2.5 is a schematic drawing of such a polar lipid molecule.

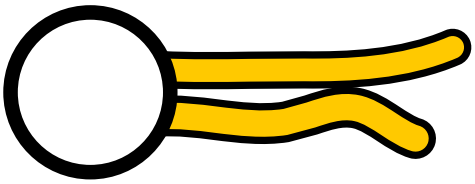

Figure 2.5: Schematic of a polar lipid, highlighting its amphiphilic nature: hydrophilic head (white circle) connected to hydrophobic tails (yellow). Adapted from a cartoon by Mariana Ruiz Villarreal. [3]

The tail typically comprises hydrocarbon chains. The ease of C–C bond rotations makes the lipids (in comparison to DNA and proteins) rather flexible biomolecules. Most biolipids contain two different hydrocarbon chains, one of which is unsaturated [13], that is, has one or more double C–C bonds[1]. A standard chain has 14 to 22 carbons and up to six double bonds.

[1] A double C–C bond has two isomers: cis and trans. Nature prefers the cis, which leads to kinkier tails and livelier membranes. The trans tails are straight and stiff and thus boring and bad for health.

The polar head can be either neutral or charged. For example the (glycero)phospholipids, the most abundant class of lipids in cellular membranes [14], has five main headgroups: two[2] neutral (zwitterionic), and three[3] negative (anionic) [13]. In fact, the charged biolipids are almost exclusively anionic, with only two known cationic (positive) exceptions: sphingosine [15] and oleamide [16].

Note, however, that not all lipids appear as Fig. 2.5. Cholesterol, for example, classifies as a lipid, although instead of two flexible chains its hydrophobic tail is a stiff and bulky steroid ring stucture (with a tiny hydrocarbon stub in the end) and its head just a simple small OH group.

The ample choice of tails and heads allows a huge variation; thousands of different types of lipids have been found in biomembranes [17]. One of the key questions in contemporary lipid research is to find out the cause of this plentifulness. Is it just a redundant side effect of evolution or diversity absolutely required for survival?

2.3 Lipid membranes

Because of their hydrophobic tails, lipids dissolve poorly in water. As a small aside: the word 'hydrophobic' is actually somewhat misleading. A substance that has this property is not actually 'scared' of water, but rather it is the water that prefers not to interact with the intruder. Say, if a lipid tail is in contact with water, the nearby H_2O molecules prefer to orient such that they maintain hydrogen bonds with other H_2O molecules. Because of this stubbornness, the number of conformations available for them is drastically smaller than in bulk water. The entropic penalty coming from this is considered to be the main source of the hydrophobic effect [10].

Getting back to the main topic: In a watery environment, lipids organize in such a way that the contact between water and tails is minimized. In particular, if the lipids are polar, they form superstructures (Fig. 2.6) in which the hydrophilic heads interact with water and protect the hydrophobic tails.

The actual shape of the superstructure depends on the average shape of the lipid (essentially the difference of the space required by the head and by the tail). In addition to micelles, vesicles and bilayers (Fig. 2.6), many other intriguing phases are possible [18].

[2] Phosphatidylcholine and phosphatidylethanolamine.
[3] Phosphatidylserine, phosphatidylglycerol and phosphatidylinositol.

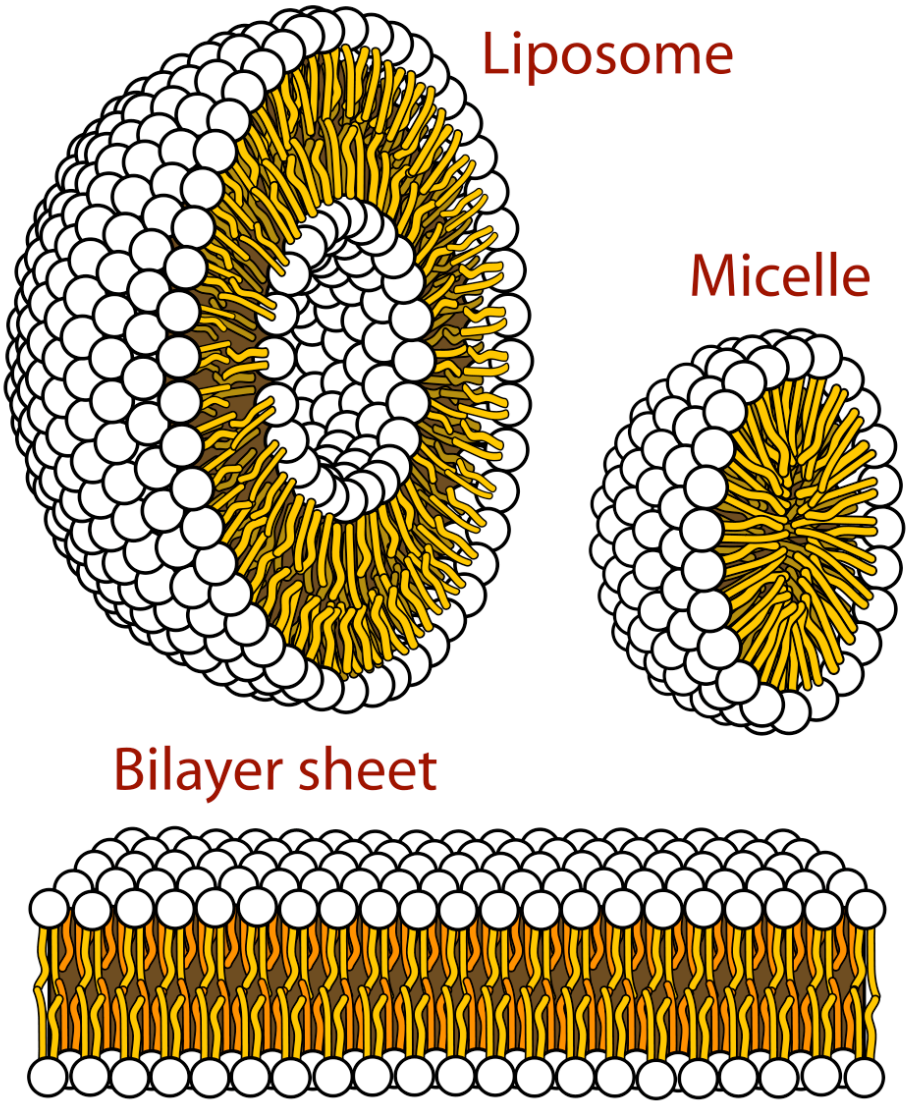

Figure 2.6: Some lipid superstructures. The self-organized structures owe their existence to water: the hydrophilic heads (Fig. 2.5) orient towards the aqueous surroundings, the tails try to hide away. Cartoon by Mariana Ruiz Villarreal [3].

A bilayer is preferred when the lipid is approximately cylindrical. Even non-cylindrical lipids can be packed into bilayers, but the more the average lipid shape deviates from cylindrical (bigger head with shorter tail / smaller head with longer tail) the less stable the bilayer will be, as the built-in frustration increases with curvature stress. In the present study we shall work exclusively with bilayers.

Under physiological conditions bilayers of most biologically relevant lipid species are lively structures. They are characterized by fast diffusion of lipids along the membrane, rapidly reorienting tails and consequently a highly disordered hydrocarbon core, plus a liquid-like arrangement of headgroups on the surface [19–21]. This state is referred to as the liquid–disordered phase [13].

If we, however, lower temperature below T_m, the main phase transition temperature, the bilayer undergoes a first order phase transition into what is known as the solid–ordered phase [22]. This state is pretty much the exact opposite of the lively liquid–disordered phase. The lateral diffusion is reduced to a hundredth of what it was in the liquid–disordered phase [13]. The tails are hardly moving, but point towards the bilayer center almost fully extended. The lipids are packed tightly and the headgroups have hexagonal order [19–21]. The biological functionality is lost.

Clearly for biological function the softness of the bilayer is of paramount importance. A soft, lively bilayer reacts to external stresses not by breaking, but by flexing and stretching. Should it rupture, it quickly heals itself due to its innate ability of self-organization. The source for softness lies in the flexibility and disorder of the tails. This in turn is due to thermal energy, which above T_m is able to cause frequent rotations around the C–C bonds.

In addition to these conformational changes of the tail, taking place in a few picoseconds, several other thermally driven lipid motions, spanning a wide variety of time scales, take place in the biologically relevant liquid disordered phase [13]. Partial protrusions of single molecules into the water phase, and their quick returns back to the bilayer, take just a few picoseconds. Rotations of lipids around their axis perpendicular to the membrane take place on nanosecond time scales. The lateral diffusion of lipids along the membrane plane has a characteristic scale of a few tens of nanoseconds. The so called flip-flop, an event in which a lipid head moves from one monolayer to the other through the hydrophobic core of the membrane, is very rare. The process itself takes place rapidly, in nanoseconds, but a given lipid typically experiences only one in hours, possibly days. The actual rates of all these motions naturally depend on the lipid molecule in question as well as on the external conditions.

Liquid–disordered bilayers exhibit, in addition to single lipid motions, a variety of collective motions [13]. For example bilayer undulations and bilayer thickness fluctuations are important membrane phenomena, although their rather large characteristic length scales make them difficult, if not impossible, to be studied using molecular modeling.

Finally, it is noteworthy that most of the interesting lipid bilayer systems do actually comprise more than just one single lipid species. This can naturally lead to a more complex phase behavior, depending on the mixing properties of the constituent lipids. If the lipids phase separate, various kinds of domains can be found, depending on the lipid composition and environmental conditions [23–26].

2.4 Cationic membranes

As we have seen in Sec. 2.1, lipid bilayers are one the most fundamental structures in biology. In addition, synthetic bilayer systems are widely used in numerous technological and medical applications [13]. Liposomes (Fig. 2.6), for example, are efficient delivery vehicles for transporting genetic material, proteins or drug molecules into cells [27, 28]. In cancer research, in particular, the drug carrying capacity of liposomes has been studied for decades [29, 30], and since the 1990's liposomally delivered anticancer drugs have been in clinical use [31].

As biomembranes and DNA have net negative charges, they prefer association with lipid surfaces that carry a net positive charge: the cationic membranes [32]. This has raised interest in using synthetic cationic lipids to build efficient non-viral transfer vehicles [33], and the complexes formed by DNA and cationic lipid bilayers have been extensively studied experimentally [34–36]. Presently they are widely used to deliver DNA into cultured cells, but the mechanism underlying the cationic lipid delivery of genes is still not fully understood [37]. Recently, the aptness of cationic lipids to deliver interfering RNA strands (used in the iRNA technique for post-transcriptionally knocking down the expression of a target gene) to the cytoplasm has drawn attention [38, 39].

Our focus will be on one particular set of cationic bilayers, those of binary DMTAP/DMPC (DiMyristoylTrimethylAmmoniumPropane / DiMyristoylPhosphatidylCholine, Fig. 2.7) lipid mixtures. The synthetic DMTAP lipid is cationic and thus responsible for the net positive charge of the whole bilayer; the naturally occurring DMPC is net neutral (zwitterionic), see Fig. 2.7. Their bilayers were experimentally found to form stable complexes with DNA [40–43]. In molecular dynamics simulation of the complexes, strong interactions between the DMTAP and DMPC heads appeared [44].

This finding prompted Gurtovenko and coworkers [45] to study pure binary DMTAP/DMPC bilayer systems, and to elucidate the effect of the DMTAP mole fraction, χ_{TAP}, on the structural and electrostatic properties of the bilayer. Their work is a prime example of how a molecular-level simulation can help to confirm a hypothesized mechanism behind observed macroscopically measured phenomena—or even to reveal previously unexpected mechanisms. Let us summarize their results.

The structural changes of the bilayer were intertwined with its electrostatic responses. A change of χ_{TAP} lead to (1) a nonmonotonic change in the average area per lipid, (2) clear reorientation of the DMPC heads, and (3) considerable changes in the electrostatic po-

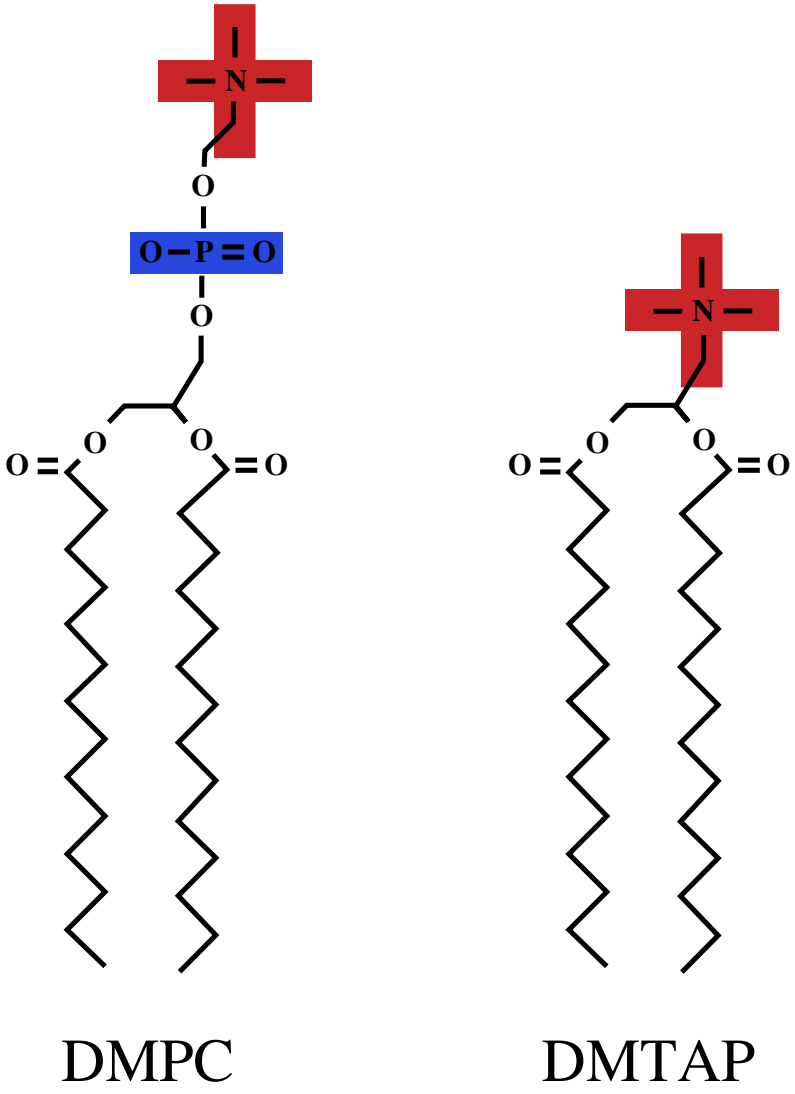

Figure 2.7: The two lipids that form the cationic bilayers have identical tails but differ in their head groups. DMPC is neutral (zwitterionic), DMTAP cationic.

tential profile across the bilayer. All these are changes that should play a role when the bilayer interacts with charged objects, DNA, proteins, drugs, or the cell surfaces.

The average area per lipid as a function of χ_{TAP} was a nonmonotonic (upwards concave) curve with a global minimum (0.58 ± 0.01 nm^2) at roughly equimolar lipid composition (upper panel in Fig. 2.8). In other words, small amounts of DMTAP lipids in an almost pure DMPC bilayer lead to compression of the bilayer. And vice versa, adding some DMPC lipids into an almost pure DMTAP bilayer had a similar compressing effect. Notably, a pure DMTAP bilayer had a considerable higher average area per lipid (0.71 ± 0.01 nm^2) than a pure DMPC bilayer (0.66 ± 0.01 nm^2). Clearly this nonmonotonic behavior is not explainable simply by steric interactions between the two lipid components, but some other competing phenomena have to play a role.

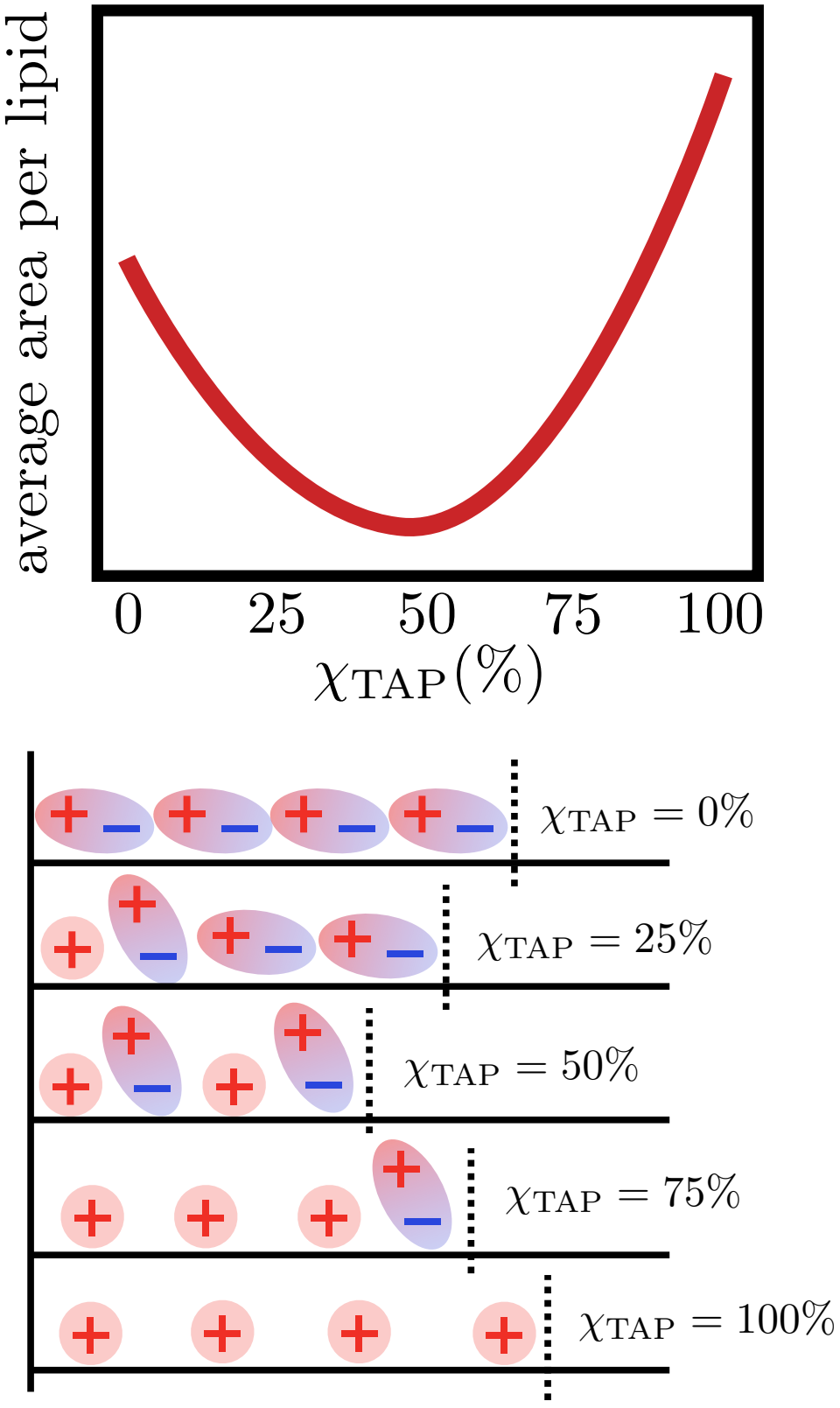

Figure 2.8: A qualitative reproduction of the main results of Gurtovenko and coworkers [45]. The upper panel shows how the average area per lipid as a function of χ_{TAP}, the DMTAP mole fraction, reached its minimum at equimolar lipid composition. The lower panel gives the schematic explanation suggested by Gurtovenko and coworkers to interpret their findings. In the lower panel only the lipid heads are drawn, compare to Fig. 2.7.

The DMPC head orientations were found to be affected by even trace amounts of DMTAP. The DMPC dipoles, aligned mostly along the bilayer plane in the pure DMPC bilayer, assumed orientations more and more along the bilayer normal with increasing χ_{TAP}. It seemed that the positively charged DMTAP heads forced the dipolar DMPC heads to rise and point up.

To explain these phenomena, Gurtovenko and coworkers suggested a simple schematic scenario, sketched in the lower panel of Fig. 2.8. It naturally connects the reduction of the average area per lipid to the reorientation of the DMPC dipolar heads, and this in turn to the electrostatic interactions between the heads of the two lipid components. According to the scenario, the bilayer compression at small χ_{TAP} arised from the reorientation of the DMPC heads when neighboring a DMTAP head. This reorientation lead to a smaller area per lipid per DMPC and thus a compression of the whole bilayer. An additional compressive factor was that the DMTAP heads are smaller in size than the DMPC heads. After reaching the equimolar composition, however, adding more DMTAP started to increase the average area per lipid. This was simply connected to the fact that neighboring DMTAP heads strongly repelled one another electrostatically, requiring more area per lipid.

Though this cartoon description was very simplified, it was able to quite nicely grasp the qualitative features observed. Later it has been corroborated by experimental findings [46] as well as theoretical work [47].

2.5 Electrostatics of lipid bilayers

When delivering their cargo to the target cells, the cationic membrane vehicles (Sec. 2.4) will be immersed in an aqueous solution of considerable ionic strength. The effect that the various ions in the physiological buffer (Na^+, Cl^-, K^+, Mg^{2+}, Ca^{2+}, ...) will have on the membrane will depend on the membrane structure and charge distribution [48]. The resulting distributions of ions and electrostatic potentials are the subject of the present section. The main focus is on the Poisson–Boltzmann theory (Sec. 2.5.1), which connects the ion distributions to the local electrostatic potential in a mean field way. Section 2.5.2 discusses the issue of calculating the electrostatic potential resulting from a given charge distribution in a system with nonhomogeneous relative permittivity.

2.5.1 Poisson–Boltzmann theory

The average ion distributions surrounding a charged surface are often described using a mean field approximation that treats ions implicitly as an ion cloud, the so-called Poisson–Boltzmann theory [18, 49]. It neglects fluctuations and correlations, the finite size of ions, and the discreteness of solvent, and therefore has obvious restrictions; pronounced deviations from its predictions emerge at the limit of high ion concentrations [50–52], as well as in the presence of large surface charge densities or multivalent ions [53–57]. There are several theories that go beyond the Poisson–Boltzmann approximation [58–63]. However, for many biologically relevant systems the Poisson–Boltzmann theory does provide a simple, intuitive and relevant picture of their electrostatic interactions.

The basic assumption underlying the Poisson–Boltzmann approach is that the local ion density $\rho(\boldsymbol{r})$ depends of the electrostatic potential energy $qV(\boldsymbol{r})$ according to the Boltzmann weight

$$\rho(\boldsymbol{r}) \sim e^{-qV(\boldsymbol{r})/k_BT}. \tag{2.1}$$

Here q is the charge of the ion, $V(\boldsymbol{r})$ the electrostatic potential at position $\boldsymbol{r}$, and k_BT the thermal energy. Consequently, in the Poisson–Boltzmann framework, if one knows the ion density ρ, one can trivially work out the electrostatic potential V, and the other way around. Before we go further into the actual theory, however, let us acquaint ourselves with the three important lengths characterizing the electrostatic interactions between a charged surface and its surrounding electrolyte. Note that, in keeping with the simulations in this work, we take the ions in the solution to be monovalent.

Bjerrum length is the yardstick of electrostatic physics. It is the distance at which the electrostatic energy between two unit charges equals the thermal energy

$$\ell_{\mathrm{B}} = \frac{e^2}{4\pi\epsilon_0\epsilon_r k_BT}. \tag{2.2}$$

Here e is the elementary charge, k_B is the Boltzmann constant, T is temperature, ϵ_0 is the vacuum permittivity and ϵ_r is the relative permittivity of the medium.

Concerning the electrostatics of a lipid bilayer, it is worth noting that at the water–membrane interface the Bjerrum length changes by a considerable amount. In bulk water at 323 K, $\epsilon_r \approx 70$, such that $\ell_{\mathrm{B}} \approx 0.74$ nm. In contrast, inside the hydrophobic core of the membrane, ϵ_r is much lower (≈ 2) and the Bjerrum length much larger ($\ell_{\mathrm{B}} \approx 26$ nm).

Gouy–Chapman length is a characteristic of charged walls. It is the distance at which the electrostatic energy between a monovalent counter ion and the wall becomes equal to the thermal energy

$$b = \frac{e}{2\pi|\sigma|\ell_{\mathrm{B}}}. \tag{2.3}$$

The model wall is infinite, smooth, impenetrable, and has a uniform surface charge density σ. Its counter ions form a diffuse cloud next to the wall surface, such that together with the oppositely charged wall they create an electric double layer. The Gouy–Chapman length is also a measure for the counter ion cloud thickness, as half of the counter ions reside within b from the wall [49]. For lipid bilayers b is typically a few Ångströms.

Debye–Hückel length is a characteristic of an electrolyte containing both negative and positive ions. Also known as the electrostatic screening length, it can be interpreted [49] as the characteristic distance beyond which the electrostatic interaction of a given ion pair is (exponentially) strongly screened by the other ions in the solution

$$\lambda_{\mathrm{D}} = \frac{1}{\sqrt{8\pi\ell_{\mathrm{B}}\rho_{\mathrm{s}}}}. \tag{2.4}$$

Here ρ_{s} is the average number density of the (symmetric monovalent) salt in the solution. The Debye–Hückel screening length decreases when the concentration of ions in solution goes up. For instance, at 323 K in 0.1 M aqueous solution of monovalent salt $\lambda_{\mathrm{D}} = 0.95$ nm, whereas at 1.0 M salt concentration λ_{D} decreases to 0.30 nm.

Within a wide range of length scales ℓ_{B}, b, and λ_{D}, the distribution of ions in an electrolyte solution surrounding a charged macroscopic object is described by the Poisson–Boltzmann theory [63]. The theory handles ions using a mean field approach; each ion experiences a smoothed averaged potential coming from the cloud of all other ions, but individual pair interactions are not explicitly considered. In other words, the theory assumes the thermodynamical equilibrium ion densities to follow the Boltzmann distribution

$$\rho_{\pm}(\boldsymbol{r}) = \rho_{\pm}^{0} \exp\left(\mp\frac{eV(\boldsymbol{r})}{k_B T}\right). \tag{2.5}$$

Here $\rho_{\pm}^{0}$ are the respective average ion densities of monovalent cations $(+)$ and anions $(-)$ at $V \to 0$. Combining Eq. (2.5) with the Poisson equation[4]

$$\frac{\partial}{\partial \boldsymbol{r}} \cdot \frac{\partial}{\partial \boldsymbol{r}} V(\boldsymbol{r}) = -\frac{\rho(\boldsymbol{r})}{\epsilon_0 \epsilon_r} \tag{2.6}$$

[4]Note that a homogeneous relative permittivity $\partial\epsilon_r(\boldsymbol{r})/\partial\boldsymbol{r} = 0$ is assumed.

relates the electrostatic potential $V(\boldsymbol{r})$ to the charge density $\rho(\boldsymbol{r}) = e\,(\rho_+(\boldsymbol{r}) - \rho_-(\boldsymbol{r}))$ and gives the Poisson–Boltzmann equation

$$\frac{\partial}{\partial \boldsymbol{r}} \cdot \frac{\partial}{\partial \boldsymbol{r}} V(\boldsymbol{r}) = \frac{e}{\epsilon_0 \epsilon_r} \left(\rho_-^0 \exp\left(+\frac{eV(\boldsymbol{r})}{k_B T} \right) - \rho_+^0 \exp\left(-\frac{eV(\boldsymbol{r})}{k_B T} \right) \right). \tag{2.7}$$

To obtain $V(\boldsymbol{r})$ and $\rho_\pm(\boldsymbol{r})$, the Poisson–Boltzmann equation (2.7) is solved subject to appropriate boundary conditions. This is how the surroundings of the ions, for example the surface of a charged bilayer, enter the theory.

To gain insight into the distributions of monovalent ions surrounding a cationic lipid bilayer in water (the system simulated in this work), the Poisson–Boltzmann results for a planar surface with a constant surface charge density $\sigma > 0$ are valuable. In the simplest salt-free case, when only monovalent counterions are present, the potential profile

$$V(z) = V_0 - \frac{2k_B T}{e} \ln(z + b), \tag{2.8}$$

and the corresponding counter ion number density profile

$$\rho_-(z) = \frac{1}{2\pi \ell_B} \frac{1}{(z+b)^2} \tag{2.9}$$

result at distance z from the charged wall.

The situation becomes more involved when salt is added to the system. For the case of monovalent ions the potential profile at distance z from the wall then is

$$V(z) = -\frac{2k_B T}{e} \ln \frac{1 - \gamma e^{-z/\lambda_\mathrm{D}}}{1 + \gamma e^{-z/\lambda_\mathrm{D}}}, \tag{2.10}$$

and the ion number density profiles

$$\rho_\pm(z) = \rho_\mathrm{s} \left(\frac{1 \mp \gamma e^{-z/\lambda_\mathrm{D}}}{1 \pm \gamma e^{-z/\lambda_\mathrm{D}}} \right)^2. \tag{2.11}$$

Here $\rho_\mathrm{s} = \rho_\pm^0 = \rho_\pm(\infty)$ is the salt number density in bulk water. The constant γ is a function of b and λ_D,

$$\gamma = -\frac{b}{\lambda_\mathrm{D}} + \sqrt{\left(\frac{b}{\lambda_\mathrm{D}} \right)^2 + 1}.$$

For lipid bilayer systems it is of interest to study a case in which there are two walls close to one another. This corresponds, for example, to the situation in a lipid bilayer stack. In

the absence of added salt the two-plate case results in the potential profile

$$V(z) = -\frac{k_B T}{e} \ln\left(\cos^2(Kz)\right) \tag{2.12}$$

and the counter ion density profile

$$\rho_-(z) = \frac{\rho_\mathrm{m}}{\cos^2(Kz)}. \tag{2.13}$$

Note that here $z = 0$ is the midplane of the water slab, and the two walls lie at $z = \pm d/2$. The constant $K = \sqrt{2\pi\ell_B\rho_\mathrm{m}}$ and $\rho_\mathrm{m} = \rho_-(0)$. For the two-plate case with added salt, the exact solution is not expressible explicitly, but only as an elliptic integral [49].

It is worth noting that even if the Poisson–Boltzmann equation is analytically unsolvable for many realistic systems, it still permits a numerical solution and obtaining the ion profiles as well as the free energies of complex systems. A lipid membrane, for example, is never the idealized impenetrable homogenously charged wall assumed by the analytically solvable models, but rather the very structure of the wall is modified by its interactions with the electrolyte. The membrane can bend, change its local charge density, and vary locally in roughness. Nevertheless, if the average charge distribution of the membrane is known, the Poisson–Boltzmann theory is capable of quite accurately predicting the surrounding ion profiles [64].

2.5.2 Potential calculation

The average electrostatic potential profile $V(z)$ of a membrane is of interest not only because of the direct connection to the Poisson–Boltzmann theory (Sec. 2.5.1), but in particular as the potential differences play a crucial role in many biologically relevant systems. The most obvious example being the -70 mV resting potential across a neuronal membrane.

To calculate $V(z)$ from a simulation one should start with the Maxwell's first equation

$$\frac{\partial}{\partial \boldsymbol{r}} \cdot \boldsymbol{D}(\boldsymbol{r}) = \rho(\boldsymbol{r}). \tag{2.14}$$

Here the electric displacement field $\boldsymbol{D}(\boldsymbol{r}) = \epsilon_0 \boldsymbol{E}(\boldsymbol{r}) + \boldsymbol{P}(\boldsymbol{r})$, where $\boldsymbol{E}(\boldsymbol{r})$ is the electric field and $\boldsymbol{P}(\boldsymbol{r})$ is the polarization at position $\boldsymbol{r}$. If the medium is linear and isotropic, one can adequately approximate that $\boldsymbol{P}(\boldsymbol{r}) \sim \boldsymbol{E}(\boldsymbol{r})$ and $\boldsymbol{D}(\boldsymbol{r}) \approx \epsilon_0 \epsilon_r(\boldsymbol{r}) \boldsymbol{E}(\boldsymbol{r})$. Inserting this

into Eq. (2.14) gives

$$\frac{\partial}{\partial \boldsymbol{r}} \cdot (\epsilon_r(\boldsymbol{r})\boldsymbol{E}(\boldsymbol{r})) = \frac{\rho(\boldsymbol{r})}{\epsilon_0}.$$

The electric field can be obtained from the electrostatic potential $\boldsymbol{E}(r) = -\partial/\partial \boldsymbol{r} \cdot V(\boldsymbol{r})$, and therefore

$$\frac{\partial}{\partial \boldsymbol{r}} \cdot \left(\epsilon_r(\boldsymbol{r}) \frac{\partial}{\partial \boldsymbol{r}} V(\boldsymbol{r}) \right) = -\frac{\rho(\boldsymbol{r})}{\epsilon_0}. \tag{2.15}$$

For the potential profile $V(z)$, one actually averages the system over time as well as over the directions parallel to the membrane (xy). The average relative permittivity profile and the average electrostatic potential profile therefore depend only on z and we get

$$\frac{\partial}{\partial z} \left(\epsilon_r(z) \frac{\partial}{\partial z} V(z) \right) = -\frac{\rho(z)}{\epsilon_0}.$$

This can be simply doubly intgrated to get the potential

$$V(z) = -\frac{1}{\epsilon_0} \int_0^z \frac{1}{\epsilon_r(z')} \int_0^{z'} \rho(z'') dz'' dz'. \tag{2.16}$$

Here the position $z = 0$ is typically taken to be the center of the bilayer or the center of the water slab. At these points both the electrostatic potential and the electric field can be chosen to be simultaneously zero because of symmetry.

In contrast to Eq. (2.16), the relative permittivity profile $\epsilon_r(z)$ is typically not taken into account when calculating $V(z)$ from simulations [65, 66]. The reason for this omission is that it is thought that by including the partial charges (of water molecules) into $\rho(z)$, the polarization issue is taken care of correctly. This, however, is not the case, but the structure of the medium (in the form of the permittivity profile $\epsilon_r(z)$) has to be given as an input, if the Maxwell's first equation is to be used to determine $V(z)$. The problem is, of course, that the permittivity profile $\epsilon_r(z)$ is not known. Indeed, the best way of determining $V(z)$ would be to measure directly the average electrostatic potential experienced by a test charge at z.

Chapter 3

Background on molecular dynamics

Many interesting systems in chemistry, physics and biology are considered to be classical many-body systems. In other words, they consist of a set of atoms that can be treated using classical mechanics; no quantum mechanical effects are needed for a sufficient description. In molecular dynamics simulations the equations of motion governing the microscopic time evolution of these systems are solved numerically subject to appropriate boundary conditions.

The history of the method is long, and over decades it has evolved into an important and widely used theoretical tool [67]. Nowadays it allows detailed modelling of a wide range of systems—including many biologically relevant systems such as proteins [68]. It opens a window into the microscopic dynamical behaviour of the individual atoms that make up a given system. In addition to this, molecular dynamics can be used for sampling various statistical mechanical ensembles to determine equilibrium properties [69].

The methodology of molecular dynamics is based on the principles of classical mechanics, which will be briefly discussed in Sec. 3.1. Then we shall review the main aspects of molecular dynamics methodology: the force fields (Sec. 3.2), boundary conditions (Sec. 3.3), and numerical integrators (Sec. 3.4). Finally in Sec. 3.5 we list the particular simulation protocols used in this work.

3.1 Hamiltonian dynamics

The physical state of a d-dimensional system comprising N classical particles is at any given time t specified by the coordinates $\boldsymbol{q}(t) = (\boldsymbol{q}_1(t)\, \boldsymbol{q}_2(t) \cdots \boldsymbol{q}_N(t))$ and momenta $\boldsymbol{p}(t) = (\boldsymbol{p}_1(t)\, \boldsymbol{p}_2(t) \cdots \boldsymbol{p}_N(t))$, with each $\boldsymbol{q}_i(t)$ being the d-dimensional position vector and $\boldsymbol{p}_i(t) = m_i d\boldsymbol{q}_i(t)/dt$ the momentum vector of particle i. Hence, each distinct state of the system corresponds to a distinct point $\boldsymbol{\Gamma}(t) = (\boldsymbol{q}_1(t) \cdots \boldsymbol{q}_N(t)\, \boldsymbol{p}_1(t) \cdots \boldsymbol{p}_N(t))$ in a $2dN$-dimensional space called the phase space [70]. The Hamiltonian H of such a system, subject only to interparticle interactions, is

$$H(\boldsymbol{p}, \boldsymbol{q}) \equiv \sum_{i=1}^{N} \frac{\boldsymbol{p}_i^2}{2m_i} + U(\boldsymbol{q}), \tag{3.1}$$

where $U(\boldsymbol{q})$ is the interparticle potential. The time evolution of the system is then represented by the Hamilton's equations of motion

$$\begin{cases} \dot{\boldsymbol{q}}_i = \dfrac{\partial H(\boldsymbol{p}, \boldsymbol{q})}{\partial \boldsymbol{p}_i} = \dfrac{\boldsymbol{p}_i}{m_i} \\ \dot{\boldsymbol{p}}_i = -\dfrac{\partial H(\boldsymbol{p}, \boldsymbol{q})}{\partial \boldsymbol{q}_i} = -\dfrac{\partial U(\boldsymbol{q})}{\partial \boldsymbol{q}_i} = \boldsymbol{F}_i(\boldsymbol{q}), \end{cases} \tag{3.2}$$

where $\boldsymbol{F}_i$ is the force acting on particle i. These equations of motion are time reversible and conserve the Hamiltonian, i.e., $dH/dt = 0$. This is equal to conservation of energy, which allows linking molecular dynamics to statistical mechanics.

A system evolving under the Hamilton's equations is constrained on a constant energy hypersurface $H(\boldsymbol{p}, \boldsymbol{q}) = E$ of the phase space. In an archetypal molecular dynamics simulation two additional quantities, the number of particles N and the volume of the system V, are fixed. Consequently, a trajectory consisting of a series of states, each having the same N, V and E (in other words, a trajectory comprising a series of microcanonical ensemble members) is produced.

Let us assume that the system will visit, given an infinite amount of time, all the points on the hypersurface; in other words, that all the members of the microcanonical ensemble will be generated by the dynamical trajectory. If this is true, then averaging an observable $A = A(\boldsymbol{p}(t), \boldsymbol{q}(t))$ over the trajectory homogeneously in time

$$\bar{A} = \lim_{t \to \infty} \frac{1}{t} \int_0^t A\left(\boldsymbol{p}(t'), \boldsymbol{q}(t')\right) dt' \tag{3.3}$$

equals averaging it over all the states of the microcanonical ensemble

$$\langle A \rangle_{NVE} = \frac{1}{\Omega \, h^{dN} N!} \iint_V A(\boldsymbol{p}, \boldsymbol{q}) \, \delta \left(H(\boldsymbol{p}, \boldsymbol{q}) - E \right) d\boldsymbol{q} \, d\boldsymbol{p}, \tag{3.4}$$

where h is Planck's constant and Ω the microcanonical partition function

$$\Omega(N, V, E) = \frac{1}{h^{dN} N!} \iint_V \delta \left(H(\boldsymbol{p}, \boldsymbol{q}) - E \right) d\boldsymbol{q} \, d\boldsymbol{p}.$$

This key assumption $\bar{A} = \langle A \rangle_{NVE}$ is known as the ergodic hypothesis [71].

3.2 Force fields

The single most important component of a successful biomolecular simulation is the force field. It is the very core of molecular dynamics simulations, the set of functions and parameters that go into the interparticle potential $U(\boldsymbol{q})$ of the Hamiltonian in Eq. (3.1). The force field, above all, determines the behavior of a simulated system.

It is unfortunate, therefore, that among the various components of molecular dynamics simulations, the force fields currently belong to the less-advanced ones. Or as Herman Berendsen [72] formulates it: "The fact that there are many force fields in use, often developed along different routes, based on different principles, using different data, specialized for different applications and yielding different results, is a warning that the theory behind force fields is not in a good shape."

In particular, the current force fields do not comprise terms that could be routinely transferred between different molecules and that would be valid in many different environments and conditions. This is mostly due to non-additivity of the terms, as well as omission of contributions dependent on the conditions. As most force fields contain parameters that are fit to experimental data, an error or omission in one term is compensated by (errors in) the other terms, making the entire sum of terms not accurate when used for other environments or conditions than those the parameters originally were adjusted for [72].

Despite this critique, it is true that if the force field has been constructed cafefully, it will work fine close to the conditions for which it has been adjusted. It will, therefore, be able to provide important insights on the behavior of the system under study.

The force fields typically used for biomolecular modeling can be commonly written as a

following sum of contributions:

$$\begin{aligned} U &= U_{\text{non-bonded}} + U_{\text{bonded}} \\ &= U_{\text{L-J}} + U_{\text{Coulomb}} + U_{\text{length}} + U_{\text{angle}} + U_{\text{torsion}}. \end{aligned} \tag{3.5}$$

Here the first equality highlights the distinction between those interactions that exist between all atoms (non-bonded) and those that take place only between atoms covalently bound together (bonded). For the practical implementation of the simulation, the essential difference is that for the non-bonded interactions the list of the participating atoms has to be regularly updated as the distances between atoms change, whereas for the bonded interactions a fixed list can be made.

The non-bonded interactions in Eq. (3.5) have two contributions:

(1) $U_{\text{L-J}}$ actually involves two terms: the excluded volume repulsion at short and the dispersive attraction at long distances between a pair of atoms (i, j). Typically it is the Lennard-Jones potential $U^{ij}_{\text{L-J}} = C_{12}/r^{12}_{ij} - C_6/r^6_{ij}$.

(2) U_{Coulomb} describes the electrostatic interaction of a pair of atoms (i, j). This is simply the electrostatic potential $U^{ij}_{\text{Coulomb}} = q_i q_j / 4\pi\epsilon_0 r_{ij}$. Here q_i and q_j, the electric charges of the atoms i and j, can be partial charges to describe the polarization of the molecule in question.

The Lennard-Jones parameters C_{12} and C_6 may be obtained experimentally from crystal structures or by fitting simulation results to properties such as liquid density. The partial charges are generally determined from quantum mechanical calculations.

The bonded interactions in Eq. (3.5) have three contributions:

(1) U_{length} imposes the covalent bond length r_{ij} between a pair of atoms (i, j). Typically this is taken to be a harmonic potential $U^{ij}_{\text{length}} = k_r(r_{ij} - r_0)^2/2$.

(2) U_{angle} imposes the bond angle θ_{ijk} of three consecutive atoms (i, j, k). Typically a harmonic potential $U^{ijk}_{\text{angle}} = k_\theta(\theta_{ijk} - \theta_0)^2/2$.

(3) U_{torsion} imposes the dihedral angle ϕ_{ijkl} between four consecutive atoms. Typically described as a periodic function $U^{ijkl}_{\text{torsion}} = k_\phi\,(1 + \cos(3\phi_{ijkl} - \phi_0))$. The angle ϕ_{ijkl} describes a rotation around the central (j, k) bond. Often there are additional terms (1–4 interactions) between atoms i and l to make the minima of the periodic function different. In addition, to keep planar groups

planar and to prevent flipping between mirror images, the so-called improper dihedrals (extra harmonic restraints imposed on ϕ_{ijkl}) are commonly applied.

The various parameters $(k_r, r_0, k_\theta, \theta_0, k_\phi, \phi_0, \ldots)$ naturally depend on the bond in question. They are obtained from quantum mechanical calculations and calibrated on experimental data. Experimental values for the bonded parameters can be obtained for example with spectroscopic techniques and X-ray crystallography [73].

All this said, often in molecular dynamics simulations one does not even attempt to represent the covalent bonds by terms in the interparticle potential, because the very high frequency vibrations of the bonds should rather be treated quantum mechanically than using the classical approximation [73, 74]. Instead, the bonds are constrained to have fixed length (and possibly angle). This is achieved during the simulation by determining a constraint force (for each constraint at every time step) in such a way that the constraint is exactly satisfied at the end of the time step. For a molecule with many constraints, this leads to a set of coupled equations. The set of equations can be solved either in an iterative fashion, so as to satisfy each constraint in turn until convergence (as is done in SHAKE [75]) or by solving the whole matrix equation (LINCS [76]). For very simple molecules, such as water, the set of equations can also be solved analytically, which leads to fast algorithms (SETTLE [77]).

3.3 Boundary conditions

The number of particles one can include in a computer simulation is always limited by the finite memory and processor time available. For example, a fairly standard molecular dynamics simulation nowadays has a few tens of thousands of atoms. If these atoms, say 27.000 of them, are packed in a cubic box, on average 20% of them will lie on the faces of the cube[5]. Those atoms will experience qualitatively different forces than their 21.600 colleagues located inside the cube. In order to get rid of the distinction between particles-on-the-walls and particles-inside and to make a finite, rather small, system to appear as infinite, the periodic boundary conditions are frequently used [78].

The idea of the periodic boundary conditions is presented in Fig. 3.1. The so-called central box (purple) is replicated to form an infinite lattice filling the whole space. In each of the replicated boxes the periodic images of the molecules will move exactly the same way as

[5] $6 \times 30^2/30^3 = 20\%$, assuming that the atoms are packed in a simple cubic ($30 \times 30 \times 30$) lattice.

the original ones in the central box. Hence, when a molecule leaves the box, one of its images will enter through the opposite face. Thus, it is enough to keep track of only the molecules in the central box. The periodic boundary conditions will make all positions within the simulation equivalent; no molecules lay on the surface, and the system appears infinite [78]. For lipid bilayers, an infinite stack (along, say, the z-direction) of infinite membranes (laying roughly parallel to the xy-plane) separated by infinite sheets of water (again along the xy-plane) results.

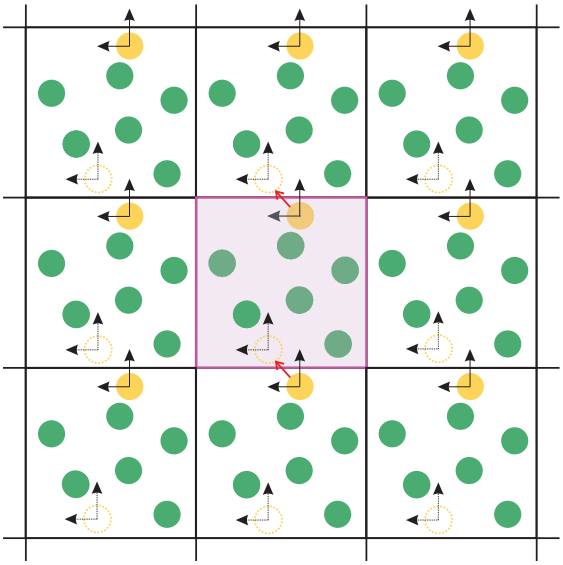

Figure 3.1: Schematic illustration of (cubic) periodic boundary conditions in a two dimensional system. A snapshot of the whole system and the movement of the yellow particle during the next time step are shown. Velocity components are represented by black arrows, the central box is shaded purple.

Periodic boundary conditions will not make the system genuinely infinite. Long-ranged potentials, such as those caused by electric monopoles, will cause a substantial interaction between a particle and its own images, leading to a certain amount of periodicity in the system. In addition, long-wavelength fluctuations cannot be seen in these systems if the wavelength exceeds the box length. Additionally, angular momentum is not preserved by the periodic boundary conditions. Despite these problems, it is generally thought that periodic boundary conditions, when carefully applied, have little effect on the equilibrium thermodynamic properties and structure [78].

Another necessary boundary condition required to emulate an experimental setup or given biological surroundings is the appropriate thermodynamic ensemble. By simply using the periodic boundary conditions (Fig. 3.1) and straightforwardly integrating the Hamilton's equations of motion (3.2), the microcanonical ensemble (constant NVE, see Sec. 3.1)

results. But the conditions of constant volume V and energy E seldom appear in experiments or nature. The more realistic conditions of constant pressure p and temperature T can, however, be achieved using for example the weak-coupling algorithm by Berendsen [79]. Although widely used, the the weak-coupling scheme does not produce a well-defined ensemble [72, 80]. If correct fluctuations are critical, this problem can be alleviated by using a combination of Nose–Hoover [81–83] temperature and Parrinello–Rahman [84, 85] pressure controls. The Berendsen and Nose–Hoover approaches to temperature control are based on fundamentally different goals. The purpose of the weak coupling scheme is to simply and efficiently relax the system from the current temperature T to the target temperature T_0. It achieves this by straightforward first order kinetics, correcting the particle velocities according to $\dot{T} = (T_0 - T)/\tau$, such that the temperature deviation decays exponentially with the time constant τ [79]. The Nose–Hoover scheme has a different aim. Although it does (slowly and oscillatorily) relax the system to the desired temperature, it above all produces the canonical distribution both for coordinates and momenta [81, 82]. Nose's seminal insight was to choose a Hamiltonian H_{Nose}, which extends the phase space by introducing an additional degree of freedom and its conjugate momentum to the equations of motion, and is designed to generate a microcanonical distribution with respect to the extended system, but a canonical distribution with respect to the actual coordinates and momenta. Thus, if a microcanonical molecular dynamics simulation based on H_{Nose} covers the constant energy surface, it will lead to a canonical distribution of the non-extended Hamiltonian H [82]. The Hamilton's equations of motion (Eq. (3.2)) corresponding to the Hamiltonian H_{Nose} unfortunately include scaling of time by the additional degree of freedom. This complication was alleviated by a time scaling transformation introduced by Hoover [83], which lead to the scheme currently known as the Nose–Hoover thermostat. For lipid bilayer simulations, another important ensemble is the NγT, in which the surface tension γ is kept constant instead of the bulk pressure p. The NγT ensemble may be realized by applying the pressure control semi-isotropically, so that the normal direction (z) and the lateral dimensions (xy) are coupled separately.

An infinite system contains an infinite number of particles, which have an infinite number of interactions between them. In principle, to find the force acting on a single particle, one needs to sum over the forces caused by each of the other particles, which means an infinite sum. This situation does not become essentially any better when one uses periodic boundary conditions. There is only a small amount of particles in the central box, but one still has to take into account all the periodic images, and hence the infinite sum is still there. If the particles, however, interact via short-ranged potentials[6] the interactions

[6]Potentials that decay faster than r^{-d}, where r is the inter-particle distance in a d-dimensional system.

with particles that are further than some cutoff radius r_{cut} away can be neglected [69]. As this spherical cutoff then naturally has to be smaller than half of the box length, one needs to consider the interaction of a given particle with only one, i.e., the nearest, image of any other particle. This natural extension to periodic boundary conditions is called the nearest image convention. It implies (Fig. 3.2) similar results as positioning an imaginary box (having the same size as the central box) centred around the given particle, and considering only the contributions of particles that lie inside this box.

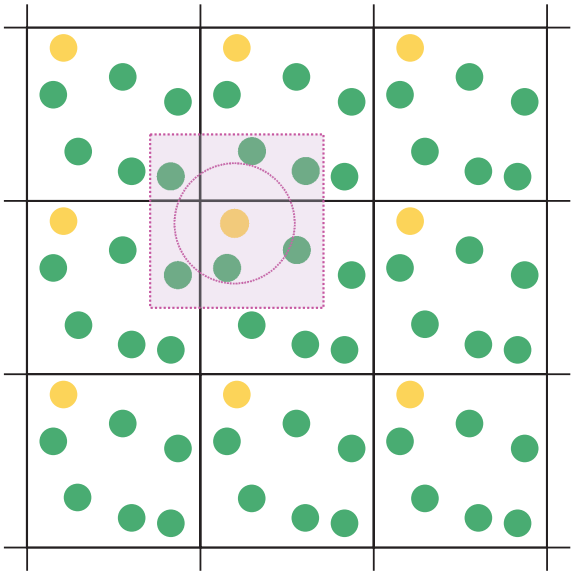

Figure 3.2: Schematic illustration of the nearest image convention in a two dimensional system. Force acting on the yellow particle is being calculated; only the images of the green particles inside the purple box are considered. The dashed line shows the spherical cutoff.

Unfortunately not all potentials are short-ranged enough to be cut off (Sec. 3.2). The electrostatic interactions, which are prevalent in biological systems, decay only as r^{-1}. If these interactions are truncated at r_{cut} in membrane simulations, significant structural [86] and dynamical [87] artifacts appear.

It is, however, possible to utilize the artificial periodicity of the periodic boundary conditions to obtain the complete untruncated electrostatic contribution. Namely, if the central cell is net charge neutral, the sum of all the Coulomb interactions between all the particles and all their images does, although extremely slowly, converge. In other words, the exact electrostatic contribution can be calculated.

Even better, the sum can be divided into short- and long-ranged parts, such that the short-ranged one converges fast in real space, and the long-ranged part converges fast in Fourier

space; a famous trick known as the Ewald summation [88].

The task of calculating the long-ranged part efficiently is, nevertheless, far from trivial. For the practical implementations in modern molecular dynamics simulations, it typically comprises the following four main stages: (1) assigning the charges on a mesh, (2) solving Poisson's equation on the mesh to get the potential, (3) differentiating the potential to get the forces, and (4) interpolating the forces back from the mesh to the particles [89]. The mesh is required such that the efficient Fast Fourier Transform [90] can be applied to solve the Poisson's equation. One of the most used algorithms today is the particle-mesh Ewald [91, 92], which provides reliable results in membrane simulations [86, 93, 94].

3.4 Integrators

In a molecular dynamics simulation an approximate solution of the many-body equations of motion (3.2) is obtained with numerical integration. The aim is not, however, to predict precisely what will happen to a system prepared precisely to some initial state. In this respect the molecular dynamics approach differs drastically from, for example, numerically predicting the trajectories of planetary systems in space.

The pursue for exactness is abandoned out of necessity. The phase space trajectories of (the nontrivial) systems studied in molecular dynamics depend sensitively on their initial conditions. Starting two trajectories from the same initial state, except for slightly perturbing just one particle, their trajectories will diverge exponentially, even if solved without numerical error [95]. As numerical integration will unavoidably introduce this small perturbation (numerical error), the numerical trajectory will unavoidably diverge exponentially fast from the precise trajectory.

The aim of a molecular dynamics simulation is, therefore, to predict the average behavior of a system that was prepared into some representative initial state. For this it is important that the numerical trajectory resembles a true trajectory of a member of the thermodynamic ensemble in question. If the numerical trajectory is statistically equivalent to a true trajectory within a bounded error, it is sufficient to ensure that the same physical observables are obtained on average [71].

The integrator algorithms considered to least perturb the ensemble are symplectic [96]. Symplecticity is a mathematical property of the algorithm, and

it implies the ability to preserve phase space volume. In addition, it can be shown that when a symplectic integrator is applied on a Hamiltonian system, it follows exactly a another Hamiltonian system whose trajectory is close to the true trajectory [97, 98].

The so-called Verlet (also known as Störmer, or Störmer–Verlet [98]) family of symplectic integrators is considered to be an excellent choice for equilibrium molecular dynamics simulations [69]. The family comprises several slightly different implementations (coordinate Verlet, velocity Verlet, leapfrog, Beeman) all of which are equivalent [72]. The leapfrog algorithm consists of repeating the following update steps of the positions $\boldsymbol{q}$ and momenta $\boldsymbol{p}$:

$$\begin{aligned} \boldsymbol{q}(t + \Delta t) &= \boldsymbol{q}(t) + \Delta t \frac{\boldsymbol{p}\,(t + \Delta t/2)}{m} \\ \boldsymbol{p}\,(t + \Delta t/2) &= \boldsymbol{p}\,(t - \Delta t/2) + \Delta t \boldsymbol{F}(t). \end{aligned}$$

Here Δt is the time discretisation, referred to as the time step. One obvious disadvantage of using the leapfrog implementation is that the positions and velocities are not calculated at the same time, which complicates calculating properties that depend on both.

3.5 Simulation details

We performed molecular dynamics simulations of one neutral and 12 cationic lipid bilayers in aqueous solutions with and without NaCl salt (Table 3.1). Each bilayer comprised a mixture of cationic dimyristoyltrimethylammoniumpropane (DMTAP) and zwitterionic dimyristoylphosphatidylcholine (DMPC) lipids (Fig. 2.7). Lipid contents of the two leaflets were identical, and in addition to the 128 lipids each system contained as many Cl^- counterions as DMTAPs: 8 (at χ_{TAP}=6%), 64 (50%), or 96 (75%). To guarantee full lipid hydration with the addition of NaCl (Table 3.1), each system had over 5000 water molecules. All systems were charge neutral.

In our united-atom description the DMTAP model has 39 and DMPC 46 interaction sites (Fig 3.3). DMPC follows the force-field of Berger[7] *et al.* [100], and DMTAP parameters were developed by Gurtovenko *et al.* [45]. For Na^+ and Cl^- ions we used the GROMACS force-field [101–103] and for water the SPC (Simple Point Charge) model [104].

The Lennard-Jones interactions were truncated at 1 nm. For the electrostatic interactions,

[7] An excellent review on the historical development of the Berger lipid force fields can be found in [99].

χ_{TAP} (%)	[NaCl] (M)	Na^+ (#)	Cl^- (#)	DMTAP (#)	DMPC (#)	$\mathrm{H_2O}$ (#)
75	0.0	0	96	96	32	5496
	0.1	10	106	96	32	5476
	0.5	49	145	96	32	5398
	1.0	96	192	96	32	5304
50	0.0	0	64	64	64	5336
	0.1	10	74	64	64	5316
	0.5	48	112	64	64	5240
	1.0	94	158	64	64	5148
6	0.0	0	8	8	120	5099
	0.1	9	17	8	120	5081
	0.5	46	54	8	120	5007
	1.0	89	97	8	120	4921
0	0.0	0	0	0	128	5097

Table 3.1: Summary of setups of MD simulations of DMPC/DMTAP lipid bilayers. χ_{TAP} is the molar DMTAP percentage, [NaCl] is the concentration of NaCl salt, and the last five columns show the numbers of different molecules in each system. The setups at each χ_{TAP} stemmed from corresponding final configurations of a DMPC/DMTAP study without salt [45], but, expecting salt ions to bind with water molecules, we increased the number of $\mathrm{H_2O}$ by 50%. After pre-equilibration of 20 ns, we made four copies of each mixed bilayer system and, to implement salt, replaced proper amounts of random water pairs by Na^+–Cl^- pairs.

we used the particle-mesh Ewald method [91, 92] (with fourth order interpolation, real space cut-off at 1 nm, the relative error in the direct and reciprocal space 10^{-5}, and Fast Fourier Transform parameters optimized for the box size), which has been shown to perform well in membrane simulations [86, 87, 105]. The covalent bonds were constrained to their equilibrium lengths by LINCS (LINear Constraint Solver) [76] in lipids and by SETTLE [77] in $\mathrm{H_2O}$.

The main transition temperature, T_m, at atmospheric pressure is 296 K for a pure DMPC bilayer [106], while it is around 311 K for a pure DMTAP bilayer [107]. For DMTAP/ DMPC mixtures, T_m depends on the molar fraction of DMTAP, χ_{TAP}; experiments at 3 bar [42] have shown that $T_m(\chi_{\mathrm{TAP}})$ is downward concave and has a global maximum of 310 K at around $\chi_{\mathrm{TAP}} \sim 45$ mol %. Therefore, all the simulations were performed at 323 K to simulate the fluid phase.

Temperature and pressure (1 bar) were controlled by the weak coupling method [79]. Heat bath coupling of lipids was separate from the rest of the system, and both subsystems had coupling time constants of 0.1 ps. Pressure coupling (time constants 1.0 ps) was applied

semi-isotropically: the simulation box length in the bilayer normal direction (z) and its cross-sectional area in the bilayer plane (xy) could vary independently. Periodic boundary conditions applied in all three directions. The time step was 2 fs, the long-range contribution to electrostatics updated every 20 fs, and the particle positions saved every 10 ps.

Each simulated system consisted of over 21 000 atoms. The total simulated time was 2.1 μs, the longest individual simulation run amounting to 242 ns. All simulations were performed using the open source GROMACS molecular simulation package version 3.3 [101–103].

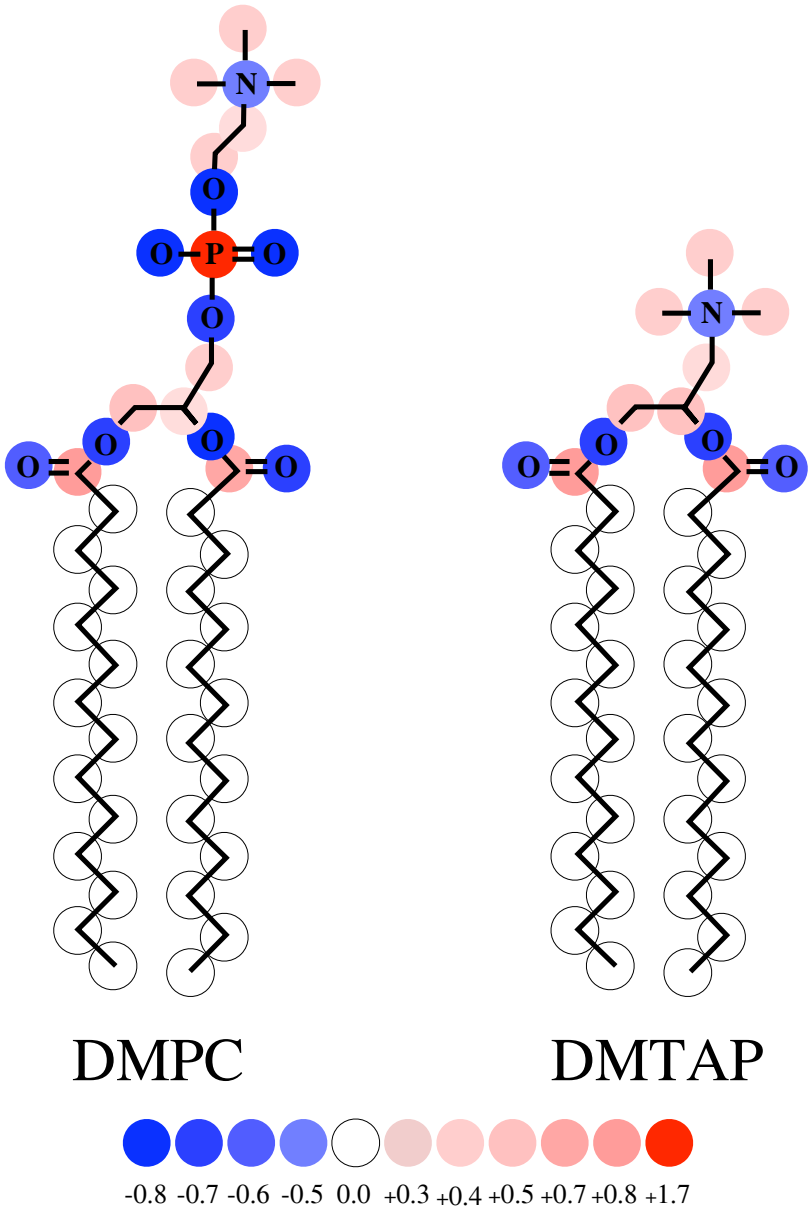

Figure 3.3: The two lipid models. Both force-fields are available online at `www.softsimu.org`. The colouring shows electric charge.

Chapter 4

Results

This chapter presents the results obtained from molecular dynamics simulations. It has two sections. Section 4.1 describes the effects of NaCl on the static properties of cationic lipid bilayer systems, and Sec. 4.2 focuses on the dynamic features. Both sections comprise several subsections, each focusing on one property of the system. In these the properties are introduced, the measurement methods used to study them are described, the results are presented, and finally the results are discussed. Both sections end with a summary of the most relevant findings in the section.

The details of the setup and parameters used in the simulations are as described in the previous chapter, Sec. 3.5. Excluding the NaCl salt, our systems are similar to those studied by Gurtovenko and coworkers: binary mixtures of neutral (zwitterionic) DMPC (dimyristoylphosphatidylcholine) and cationic DMTAP (dimyristoyltrimethylammoniumpropane) lipids [45]. Figure 4.1 shows the lipids and illustrates some of the terms used in the text to refer to their different parts.

4.1 Simulation results: static

This section focuses on the effects of NaCl on the static properties of DMPC/DMTAP bilayer systems. The first two subsections, however, deal also with some dynamical aspects, as the relaxation times required for the area per lipid (Sec. 4.1.1) and ion binding (Sec. 4.1.2) have to be estimated to quarantee that long enough simulations are performed that justifiable interpretations of the simulation data can be made. After this Sec. 4.1.3

describes in molecular detail the intimate interactions found between the sodium ions and the DMPC lipids. The next two subsections then go through on a single molecule level the effects of NaCl salt on the lipid headgroups (Sec. 4.1.4) and on the tails (Sec. 4.1.5). Then we start to move towards studying the electrostatic properties of the bilayer by first looking at the distributions of the system constituents across the membrane in Sec. 4.1.6. These are naturally followed by their charge-weighted counterparts, the charge density profiles (Sec. 4.1.7), from which we get by integration the surface charge density profiles (Sec. 4.1.8), and by another integration the electrostatic potentials across the bilayer (Sec. 4.1.9). Finally we compare the simulation results with the predictions of the Poisson–Boltzmann theory in Sec. 4.1.10. All the static properties are then summarized in Sec. 4.1.11.

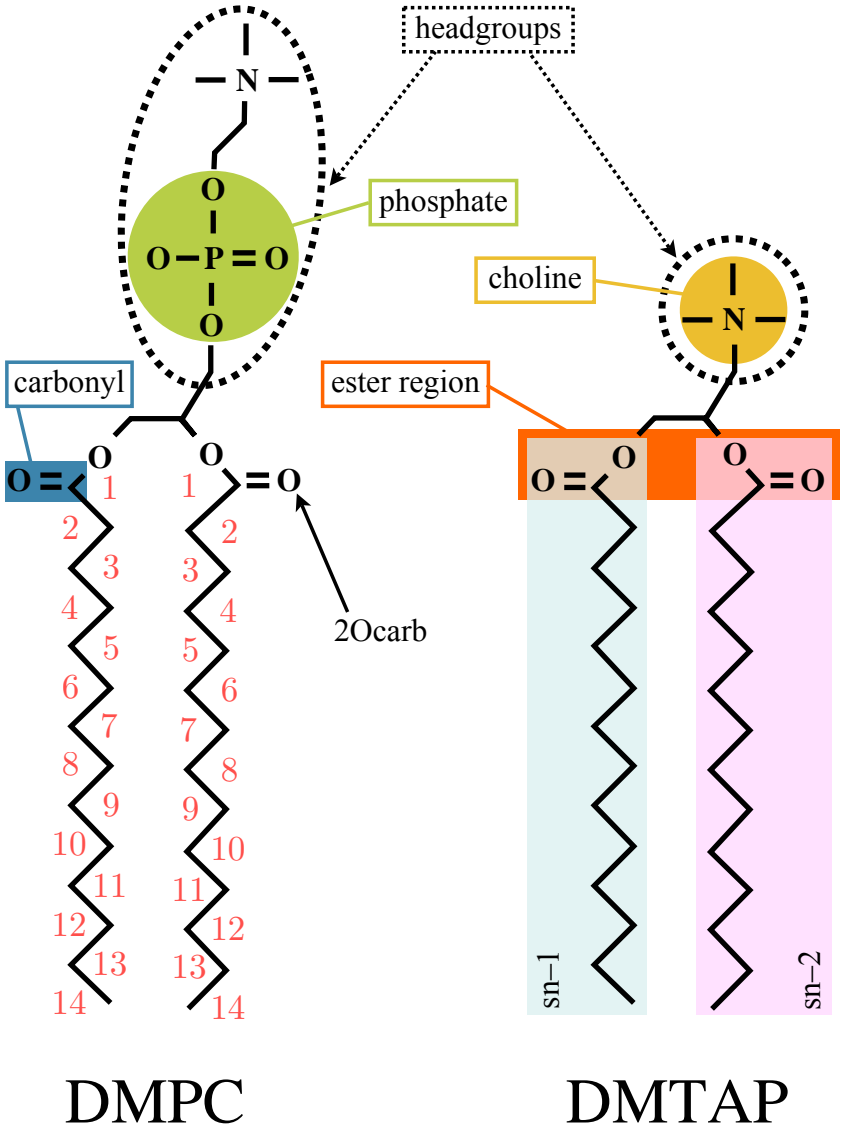

Figure 4.1: The naming concept.

4.1.1 Area per lipid

The average area per lipid, $\langle A \rangle$, is one of the few characteristics of a bilayer that is readily available experimentally. It has thus become a fundamental concept in understanding membrane phenomena, be them of static or of dynamic nature. In simulational work $\langle A \rangle$ has become the key property for assessing the equilibration of a membrane setup.

Method. Taking samples every 500 fs, we measured for each system $\langle A(t) \rangle$, the average area per lipid as a function of simulation time t, using

$$\langle A(t) \rangle = \frac{L_x(t) L_y(t)}{64}. \tag{4.1}$$

Here L_x and L_y are the simulation box dimensions in the bilayer plane (xy). The cross-sectional area of the box, $L_x L_y$, was divided equally among the 64 lipids per leaflet. Time-averaging $\langle A(t) \rangle$ over the measurement period provided $\langle A \rangle$. Because the method of block averages, as described by Flyvbjerg and Petersen [108], did not show an obvious plateau, we used the standard deviation as a pessimistic error estimate for $\langle A \rangle$.

Results. Figure 4.2 shows $\langle A(t) \rangle$, the average area per lipid as a function of the simulation time t, over the whole duration of each of the 13 simulations. The bilayers that had a strong positive charge ($\chi_{\mathrm{TAP}} = 50$ or 75%) showed no clear change in $\langle A(t) \rangle$ when NaCl was added. In the mildly positive bilayer ($\chi_{\mathrm{TAP}} = 6\%$), however, $\langle A(t) \rangle$ appeared to decrease after the addition of NaCl salt. Although for example the $\chi_{\mathrm{TAP}} = 6\%$, [NaCl] = 1.0 M -system showed a long-lived (from $t \approx 80$ until 130 ns) deviation from its average value $\langle A \rangle$, in all the systems the bilayer appeared to find its equilibrium area in a few tens of nanoseconds.

Figure 4.3 shows $\langle A \rangle$ for all the cationic bilayers. A decreasing trend with increasing NaCl concentration was observed in all the systems. The trend was, however, markedly stronger for the mildly cationic bilayer ($\chi_{\mathrm{TAP}} = 6\%$) than for the highly charged ones ($\chi_{\mathrm{TAP}} = 50$ or 75%). In the latter case the decrease could even fall within the error bars, whereas in the former the total relative compression of the bilayer was over 7%, going from 0.64±0.01 nm^2 (no salt) to 0.59±0.01 nm^2 (1.0 M).

Discussion. The monovalent NaCl salt caused a decreasing trend on the average area per lipid, $\langle A \rangle$, of a cationic DMTAP/DMPC lipid bilayer at all the studied DMTAP fractions, χ_{TAP}.

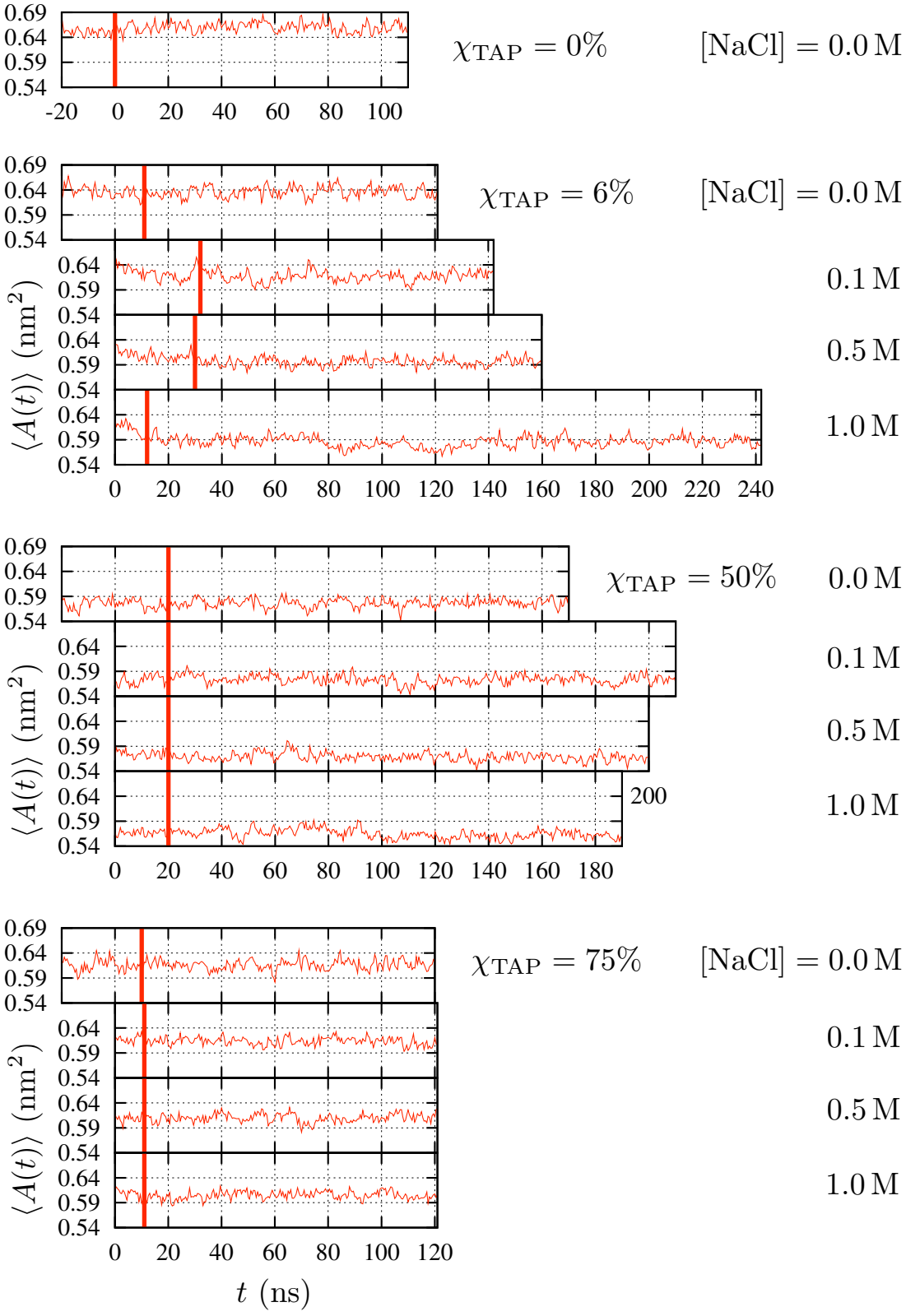

Figure 4.2: Average area per lipid as a function of time, $\langle A(t) \rangle$, for each system over its whole simulation time. The layout visualizes the relations between the systems in the setup, as systems with NaCl stemmed from ones without salt at each χ_{TAP}, see Sec. 3.5. The red vertical line separates the initial equilibration period and the measurement period.

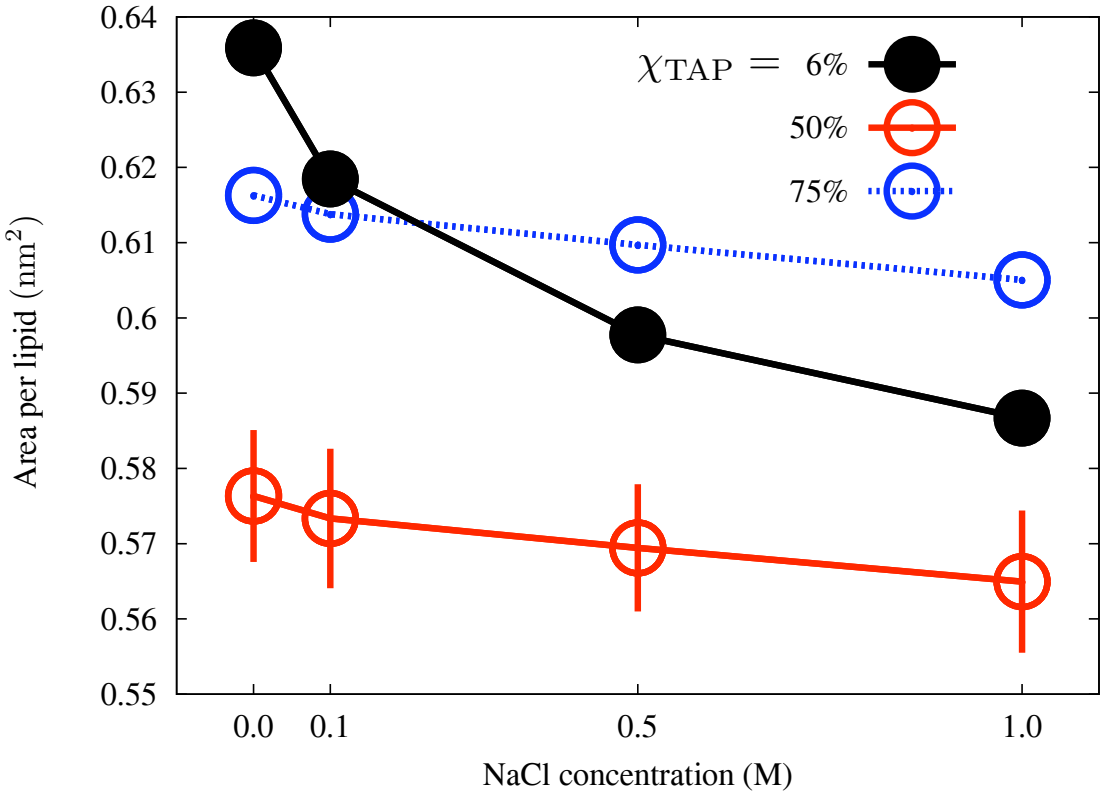

Figure 4.3: Average area per lipid, $\langle A \rangle$, as a function of [NaCl]. The standard deviation in each case was about 0.01 nm^2, but for clarity it is shown only for $\chi_{\mathrm{TAP}} = 50\%$. For pure DMPC $\langle A \rangle = 0.66 \pm 0.01$ nm^2.

Due to long-time correlations in $\langle A(t) \rangle$ this decreasing trend could not, however, be quantitatively established for the bilayers having a high positive surface charge ($\chi_{\mathrm{TAP}} = 50$ or 75%). The reason for the mild decrease of $\langle A \rangle$ in these cases could be related to the screening ability of salt ions, allowing charged lipid heads to reside closer to one another.

For the mildly charged bilayer ($\chi_{\mathrm{TAP}} = 6\%$) the effect was similar to those reported in simulation studies of pure phosphatidylcholine bilayers with monovalent salt [64, 109, 110]. It is attributable to the more compact packing of the DMPC lipids because of their tight association with sodium ions, as will be described in detail in Sec. 4.1.3.

It is worth noting that even for $\chi_{\mathrm{TAP}} = 6\%$ the decreasing effect was quite moderate compared to the effects that have been reported earlier [45] as a function of DMTAP fraction χ_{TAP}. The strong nonmonotonic dependence of $\langle A \rangle$ on χ_{TAP} was also found in this study (Fig. 4.3), $\chi_{\mathrm{TAP}} = 50\%$ giving the minimum $\langle A \rangle$.

4.1.2 Ion binding to bilayer

To clarify the interactions between positively charged lipid bilayers and monovalent salt was the main goal of the whole present study. Using molecular dynamics simulations allowed us to find not just the effects of NaCl salt on the DMPC/DMTAP bilayer properties on the large, but to see the interaction mechanism between Na^+ and Cl^- ions and the lipids in intricate molecular detail. In this subsection we discuss where the ions were binding and the time scales required for them to find their binding sites.

Methods. An intuitive feeling of the ion distributions in the systems was obtained by simply plotting snapshots from the simulation trajectories.

The mental image thus obtained was corroborated by studying the spatial distributions of ions around relevant parts of the lipid molecules. These distributions are in general terms characterised by the pair distribution functions $g(\boldsymbol{r})$, which can be averaged over the angular dependence to give the radial distribution functions $g(r)$. The radial distribution function between particles of types A and B is defined as

$$g_{\mathrm{AB}}(r) = \frac{\rho_{\mathrm{AB}}(r)}{\rho_{\mathrm{B}}} = \frac{1}{N_{\mathrm{A}}} \sum_{i=1}^{N_{\mathrm{A}}} \sum_{j=1}^{N_{\mathrm{B}}} \big\langle \delta\big(\boldsymbol{r} - (\boldsymbol{q}_{\mathrm{A},i} - \boldsymbol{q}_{\mathrm{B},j})\big) \big\rangle, \tag{4.2}$$

where $\rho_{\mathrm{AB}}(r)$ is the average number density of the type B particles at a distance r from a particle of type A and $\rho_{\mathrm{B}} = N_{\mathrm{B}}/V$. For a 3D radial distribution function V is the simulation volume, for a 2D case it is the corresponding area. It should be noticed that $\rho_{\mathrm{AB}}(r)$ is a conditional density, i.e., the density given that there is a particle of type A present at $r = 0$. From our molecular dynamics trajectories the radial distribution functions were simply measured by collecting corresponding histograms of particle distances, which were then transformed (by dividing by the bin volume) into histograms of densities. From this $g(r)$ was obtained by normalising with the average number density. In this subsection the chosen bin width was 0.1 pm.

Using the data from radial distribution functions it was possible to study average coordination numbers, N_C, of Na^+ ions with various oxygen atoms. This was done by setting a cutoff radius to 0.31 nm (to include the first coordination shell) and for each Na^+ ion in each simulation frame calculating the number of oxygens of interest within this radius. The average over sodium ions then provided $N_C(t)$ as a function of simulation time t.

Results. Figure 4.4 shows snapshots of a mildly ($\chi_{\mathrm{TAP}} = 6\%$) and a strongly cationic (50%) lipid bilayers with their Na^+ co-ions. The dependence on DMTAP mole fraction was obvious. When the positive surface charge is strong (lower snapshot), the Na^+ ions were expelled from the vicinity of the bilayer surface. In contrast, when the surface had only a mild positive charge (upper snapshot), the Na^+ ions penetrated below the lipid headgroups into the carbonyl region of the bilayer.

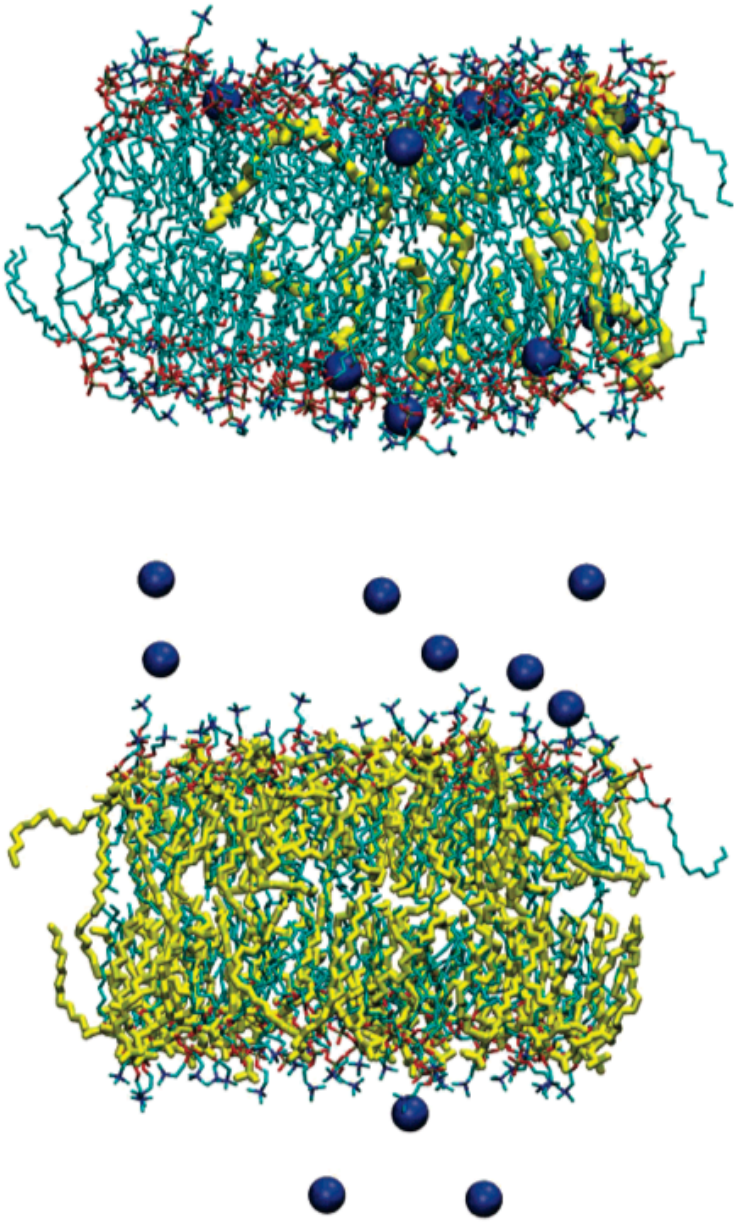

Figure 4.4: Snapshots showing the sodium ions (blue spheres) close to a mildly cationic ($\chi_{\mathrm{TAP}} = 6\%$, upper) and highly cationic ($\chi_{\mathrm{TAP}} = 50\%$, lower) lipid bilayers. DMPC tails cyan, DMTAP yellow, water and Cl^- not shown. [NaCl] = 0.1 M, simulation time 70 ns.

Figure 4.5 shows the radial distribution functions $g(r)$ between the lipid carbonyl oxygens and Na^+. When the lipid membrane had a mild positive charge ($\chi_{\mathrm{TAP}} = 6\%$), Na^+ ions

were readily associating with the DMPC carbonyl oxygen of the sn-2 chain, 2Ocarb (for the naming of lipid parts see Fig. 4.1). When, in contrast, the surface charge was large, ($\chi_{\mathrm{TAP}} = 50$ or 75%), the Na^+ ions were either completely excluded from the carbonyl region or were only able to visit it very shortly, leading to a non-existent or mild peak in the radial distribution function. No noticeable binding of Na^+ to DMTAP carbonyl oxygens was observed in any of the systems studied.

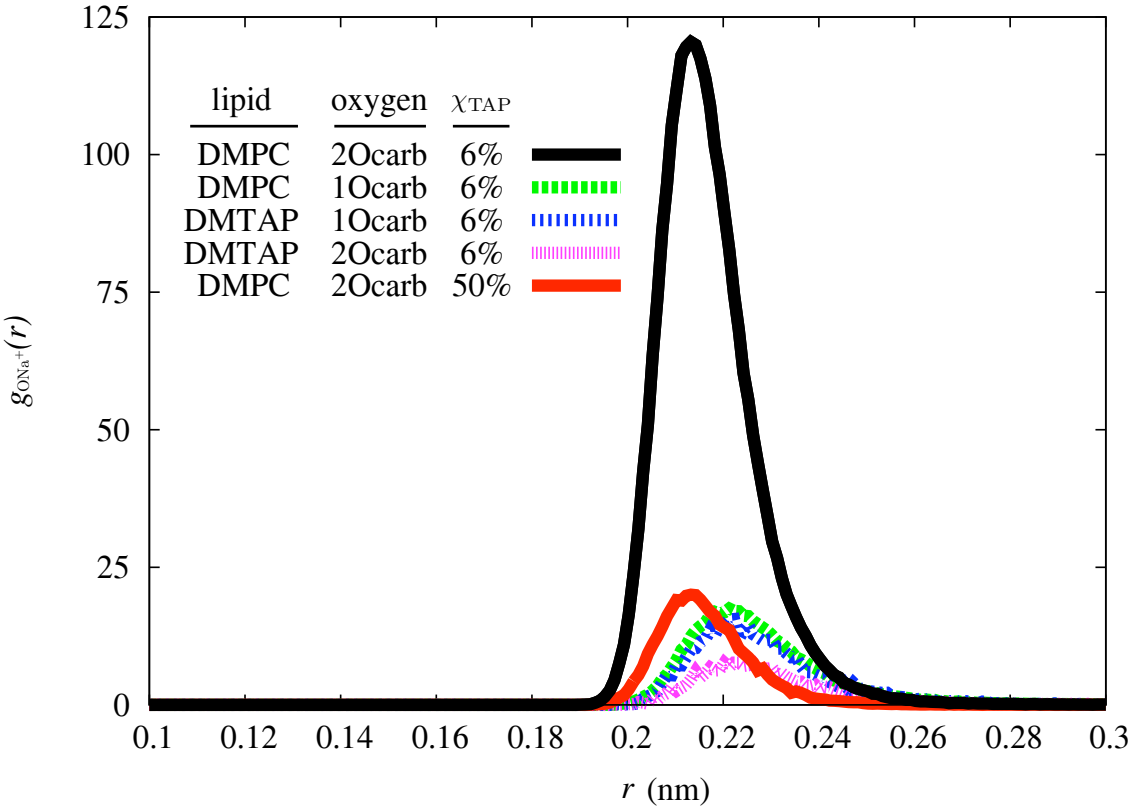

Figure 4.5: 3D radial distribution functions between the carbonyl oxygens and Na^+ ions at $\chi_{\mathrm{TAP}} = 6\%$. The 2Ocarb–$\mathrm{Na}^+$ $g(r)$ at $\chi_{\mathrm{TAP}} = 50\%$ given for reference. [NaCl] = 0.5 M.

Figure 4.6 compares the evolution of coordination of Na^+ ions with water- and DMPC carbonyl oxygens in the beginning of two simulations. With the highly charged ($\chi_{\mathrm{TAP}} = 50\%$) bilayer the Na^+ ions stayed in the bulk water, and thus there was no change in the $N_C(t)$ during the simulation. With the mildly charged (6%) bilayer the Na^+ ions were associating with the DMPCs, and thus $N_C(t)$ of water oxygens decreased with time and $N_C(t)$ of carbonyl oxygens increased. This exchange of water oxygens with DMPC carbonyl oxygens took place rather slowly; an exponential fit to the time evolutions of coordination times gave relaxation times of 32 ([NaCl]=0.1 M), 17 (0.5 M), and 10 ns (1.0 M) for Na^+ binding to the carbonyl oxygens.

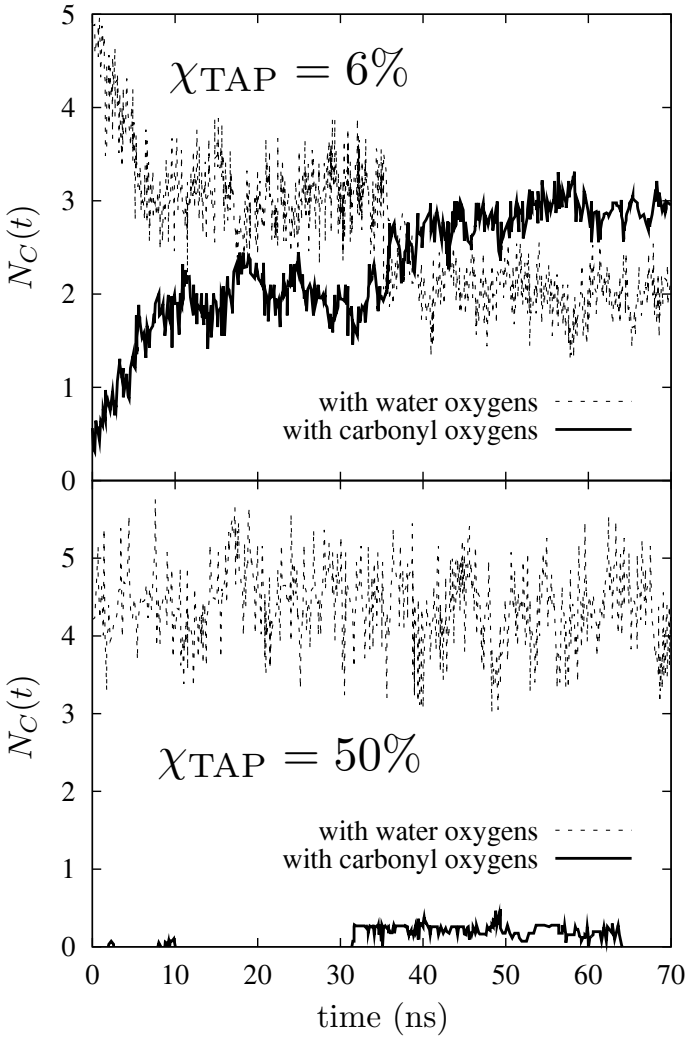

Figure 4.6: The coordination number of Na^+ ions with (DMPC carbonyl and water) oxygens as a function of time, $N_C(t)$. In both plots $[\mathrm{NaCl}] = 0.1\,\mathrm{M}$.

Discussion. We found a striking difference in the Na^+ distribution between the low (6%) and high (50 and 75%) lipid bilayer DMTAP contents (Fig. 4.4). At high χ_{TAP} the Na^+ ions were excluded from the vicinity of the cationic bilayer surface, whereas at low χ_{TAP}, in line with what has been reported for pure phosphatidylcholine bilayers [64, 109–116], the Na^+ ions were associating strongly with the DMPC 2Ocarb carbonyl oxygens (Fig. 4.5). This association was accompanied with a loss of water molecules from the first hydration shell of Na^+ ions (Fig. 4.6). This resembles closely what has been reported for pure phosphatidylcholine bilayers [64, 112].

No binding of Na^+ to the DMTAP carbonyl oxygens was found, the most plausible explanation being the close vicinity of the positive DMTAP head, preventing such close encounters of Na^+.

The exponentially slow binding of ions with lipid bilayers has been found before to depend on the type of ions and the associated time scales may sometimes be substantial [64, 112]. The time scale of tens of nanoseconds in our case for Na^+ binding is rather moderate, if compared with times required for the binding of multivalent ions such as Ca^{2+}, which can be an order of magnitude longer [112]. We used the Na^+ relaxation times as estimates for the relaxation period needed for each simulation, see Fig. 4.2.

4.1.3 Sodium–DMPC complexes

As described in the previous subsection, when the cationic bilayer was not too highly loaded with lipids carrying a net positive charge, its Na^+ co-ions were able to bind strongly with the carbonyl group of its zwitterionic lipid component. This subsection describes the resulting ion–lipid complexes.

Methods. Because the Na^+–DMPC complexes formed via the 2Ocarb (Fig. 4.5), we used the Na^+–2Ocarb distance for defining a complex as the entity formed by a single Na^+ ion and those DMPCs whose 2Ocarbs were on its first coordination shell (< 0.31 nm, see Fig. 4.5). In other words, the size of a given complex at time t equals the 2Ocarb coordination number of its Na^+ ion at time t, as determined in the previous subsection. Saving the coordination numbers of each Na^+ ion of each measurement frame provided a distribution of the different complex sizes. This allowed us to calculate the average fraction of DMPCs partaking in complexes of various sizes.

To achieve spatial resolution of Na^+ coordination across a leaflet, we also calculated $N_C(z)$, the average $N_C(t)$ over the measurement period (Fig. 4.2) and over Na^+ ions at a given distance z from the bilayer center.

Results. In the case where Na^+ ions could stay below the lipid headgroups, $\chi_{\mathrm{TAP}} = 6\%$, we found that on average 3.25±0.15 ([NaCl]=0.1 M), 2.70±0.15 (0.5 M), and 2.90±0.20 (1.0 M) DMPCs were on average bound to a single Na^+ ion inside the carbonyl region.

This averaged picture did not, however, provide the full detail of the Na^+–DMPC complexes. Looking in more detail we found a distribution of complexes having one, two, three or four lipids per Na^+ (Fig. 4.7). Bigger complexes than this were never observed to form. Notably, most of the lipids were not complexed with Na^+ ions, although as the NaCl concentration increased this fraction did go down from 78% (0.1 M) to 54% (1.0 M). At [NaCl]=0.1 M a complexed DMPC was most typically participating in a complex of

four DMPCs, and the contributions from complexes of one and two were vanishingly small. At higher [NaCl] the complexes with three and four lipids were equally typical, and those of two DMPCs were not rare either.

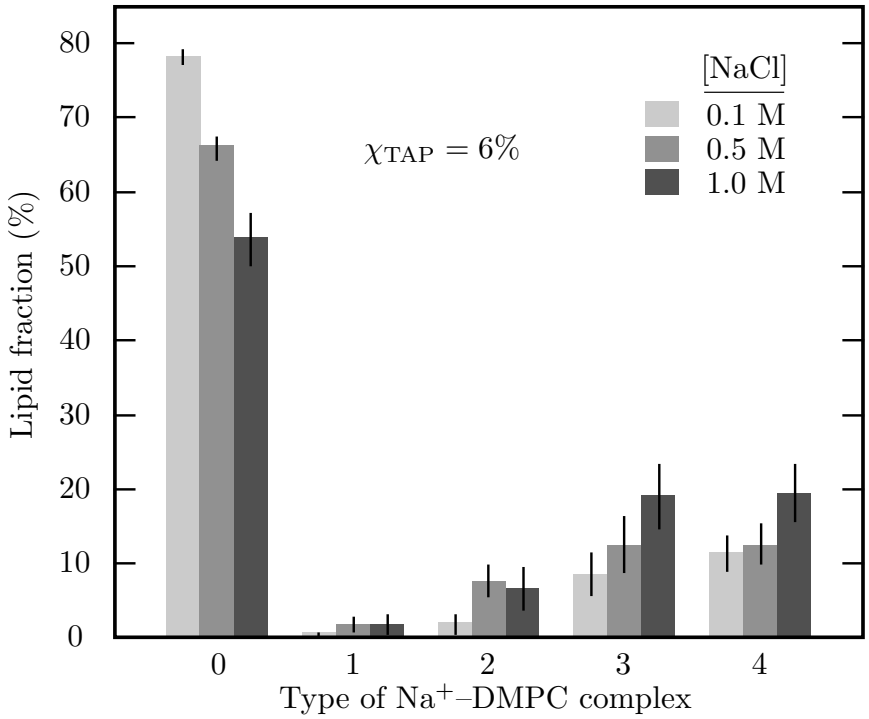

Figure 4.7: Average fractions of DMPCs participating in Na^+–DMPC complexes of different sizes: 1, 2, 3 or 4 DMPCs bound to the same Na^+. "0" stands for DMPCs not associated with any Na^+. The error bars are standard deviations.

Figure 4.8 shows the average coordination numbers N_C as a function of distance from the bilayer center: Once a Na^+ ion was able to penetrate into the carbonyl region of the lipid leaflet, it bound with the DMPC carbonyl oxygens. In the process it left behind the Cl^- ions and most of the waters, which it was associated with in the bulk water.

Discussion. We found that if a Na^+ ion was able to stay in the bilayer carbonyl region, it was on average bound to about three DMPCs. This agrees well with the findings from simulations of pure POPC bilayers [64]. Another simulation of pure DPPC bilayer[109] reports smaller number of two, but this might be an equilibration artefact as their simulation time only spanned 10 ns.

It appeared that most DMPCs associated with a Na^+ were participating in a big complex of four or three lipids. This is rather natural as a single Na^+–2Ocarb pair will have a total positive charge (see Fig. 3.3), thus attracting the 2Ocarbs of nearby DMPCs. This will make it less likely to find DMPCs that would not be sharing their bound sodiums. Rather

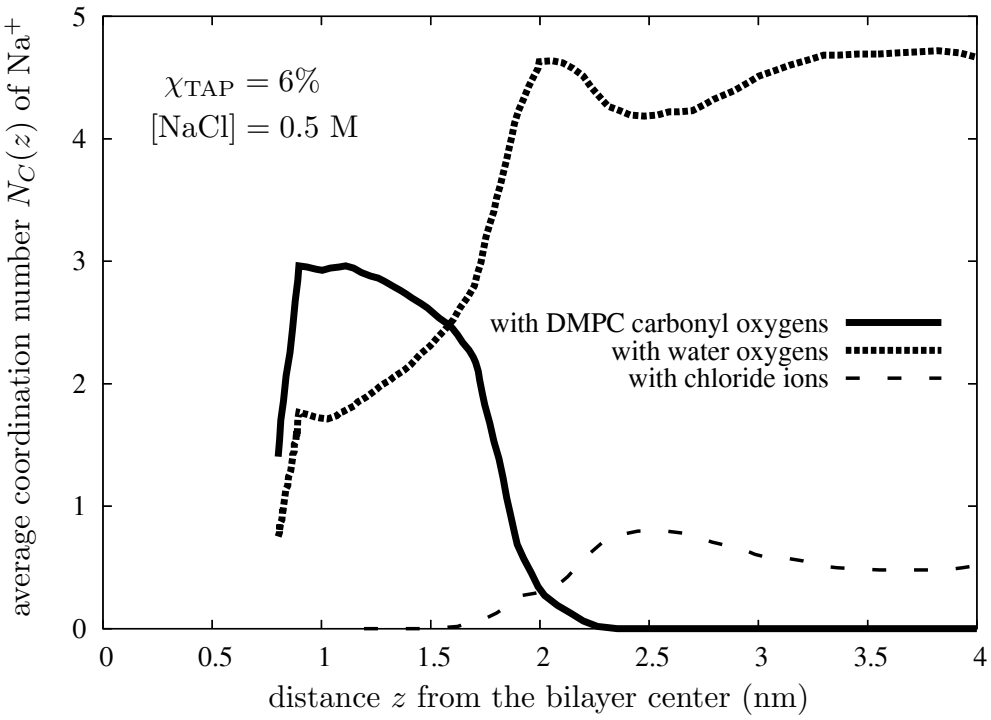

Figure 4.8: Average coordination numbers of Na^+ ions with DMPC carbonyl oxygens (solid), water oxygens (dotted), and Cl^- ions (dashed) as a function of distance in the bilayer normal direction (z) from the bilayer center.

broad distributions of Na^+—lipid complex sizes have been reported also from simulations of pure DMPC bilayers with monovalent salt [110].

One should note that the distributions given in Fig. 4.7 are not the distributions of complexes of different sizes, but the distributions of DMPCs in complexes of different sizes. To estimate the distribution of complexes of different sizes, the bar heights in Fig. 4.7 can be divided by the number of DMPCs in the complex they represent.

Figure 4.8 shows that there was also some spatial heterogeneity in the complex size distribution. The maximum value of roughly 3 DMPCs per Na^+ is reached at $z = 1.0$ nm from the bilayer center, and the average value of 2.7 roughly where the Na^+ and 2Ocarb density distributions peak, as will be seen in Sec. 4.1.6.

Concerning the relevance of the present work as a whole, the key question is if the here discussed strong association of Na^+ ions and DMPC carbonyl oxygens at low χ_{TAP} is a real effect or a model artifact.

Indeed, until rather recently, Na^+ ions were thought to be rather indifferent cations with respect to phospholipids [117, 118], and ion binding in general to take place only in

the headgroup region [119, 120]. During the past decade, however, this view has been challenged. Indirect evidence from infrared spectroscopy [121], fluorescence correlation spectroscopy [64], atomic force microscopy [122, 123], small angle x-ray diffraction [124], spin-labeling electron paramagnetic resonance spectroscopy [124], and calorimetric [64, 124] studies suggest the possibility of Na^+ interacting with lipid carbonyl oxygens, binding lipids into complexes, and thus leading to detectable changes in area per lipid, bilayer thickness and -rigidity [124], as well as lipid lateral diffusion [64], main transition temperature, calorimetric peak width [64, 124], and increase of force required to puncture the bilayer in gel phase [122, 123]. In addition to this indirect evidence, direct images of possible ion or water bridges between lipids below headgroups have been provided by frequency modulation atomic force microscopy of supported phosphatidylcholine bilayers in gel phase [125].

These experimental results have emerged in unison with the first realistic simulations on effects of ions on lipid bilayers. This simulational work at the atomistic level can be divided roughly into two categories, depending on the force-field used to describe the lipids. Using the all-atom CHARMM (Chemistry at HARvard Molecular Mechanics) parameter set 27, no complexation of Na^+ with the lipid carbonyl oxygens has been reported [126–128]. In contrast, using the "Berger lipids", i.e., variants of united atom force-fields based on Refs. [65, 100, 129], tight binding of Na^+ ions to the lipid carbonyl oxygens is found [64, 109–111, 114–116, 130–132]. Due to the different nature of these two force-fields, simulations using CHARMM27 lipids need to be performed with the area of the bilayer fixed, whereas Berger lipids allow simulations in the NpT-ensemble, such that the bilayer can adjust its area to agree with the thermodynamic parameters. Furthermore, the carbonyl region of lipid molecules is more polar in the case of the Berger force-field, so that it attracts cations considerably stronger compared to its CHARMM counter-part. Interestingly, Shinoda *et al.* [133], who modified CHARMM27 force-field replacing the ester groups with their self-developed ether groups to simulate an archael lipid bilayer, were able to use the NpT ensemble and found Na^+ binding to the ether oxygens. Further, the results on Na^+ binding acquired using the Berger lipids are not qualitatively changed if the water model is changed [111] or if CHARMM27 force-field is used for the ions [114, 116]. In fact, the ion force-fields for Na^+ and Cl^- (Gromacs, Charmm-27/22, Amber, OPLS-AA) with different combinations of water models have been systematically tested [134] and although there are some deviations, they are qualitatively in agreement.

In the light of the above, we are confident that Na^+–DMPC association is a real effect, although its strength might be somewhat overestimated by our Berger-type force field.

4.1.4 Reorientation of the DMPC headgroups

Let us now turn to discuss what the forming Na^+–DMPC complexes, as described in the previous subsection, do to the average conformations of lipid molecules. We will start from the headgroups in the present subsection, after which the next one will focus on the tails.

The orientation of the DMPC headgroup is particularly interesting, as it has a dipole moment along the P–N vector (Fig. 2.7) and thus reacts readily to electrostatic fields. It has also been found to contribute considerably to the electrostatic potential at the water–membrane interface [45, 135].

Methods. We measured the average angle $\langle\alpha\rangle$ between the DMPC headgroup P-to-N vector and the bilayer outward normal. Instead of the local bilayer outward normal we used its average, i.e., a vector pointing out of the bilayer (xy) plane along the direction of the z axis. In each system we measured α for each DMPC head in each measurement frame (Sec. 3.5). Averaging over DMPCs and time then provided $\langle\alpha\rangle$. We estimated the error as a standard error of the mean. For this we estimated the number of independent measurements by assuming each $\alpha(t)$ to be independent of the orientations of other DMPC heads at time t, and by finding the time it takes for the autocorrelation of $\alpha(t)$ to vanish completely. The latter was found to be in the range of five to thirty nanoseconds.

To study the lateral orientation of headgroups in Na^+–DMPC complexes, we measured the 2D radial distribution functions $g(r)$ between Na^+ and DMPC phosphorus. For determining the 2D $g(r)$, we projected the coordinates of P:s of a given leaflet and the Na^+ ions bound within it into the bilayer plane. To visualize the orientational information using $g(r)$ we divided it into two parts: heads pointing towards Na^+ and those pointing away. In addition, the distribution of the Na^+–P–N angle (again in the bilayer plane) was determined.

Results. Figure 4.9 shows the average angle α between the DMPC headgroup vector and the bilayer normal. We found that when DMTAP fraction was small ($\chi_{\mathrm{TAP}} = 6\%$), the addition of NaCl had a clear effect on this vertical orientation, turning the head about $9 \pm 2^\circ$ more up from the bilayer plane. Again for larger χ_{TAP} there was no effect of NaCl concentration on the DMPC head group orientation.

Also the lateral orientation of the DMPC head groups was found to be slightly affected by the bound Na^+ ions (Fig. 4.10), as head groups preferred pointing away from rather

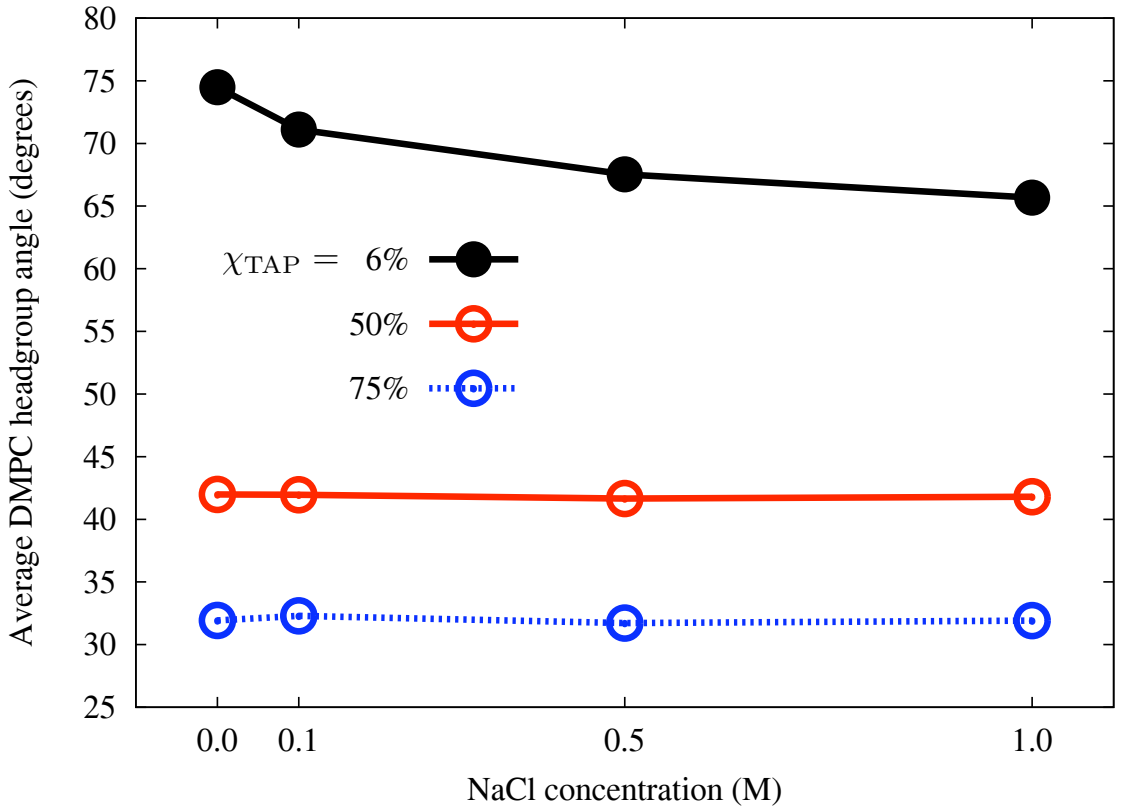

Figure 4.9: Average angle $\langle\alpha\rangle$ between the DMPC headgroup P–N vector and the bilayer outer normal. Error bars smaller than the symbol size. For pure DMPC $\langle\alpha\rangle = 79 \pm 1°$.

than towards the Na^+. Behavior was similar in all low-χ_{TAP} systems with NaCl; in the absence of salt, a corresponding analysis (Na^+ replaced with its complex-forming partner, 2Ocarb) indicated no ordering (data not shown).

Discussion. In the mildly charged bilayer, an increase in the NaCl concentration lead to reorientation of the DMPC headgroups, pushing them into a more vertical average orientation (Fig. 4.9).

As the effect was only found in the mildly cationic bilayers ($\chi_{TAP} = 6\%$), in which the Na^+ ions could stay bound in the bilayer carbonyl region (Sec. 4.1.2), it supports the view of the DMPC heads working as "voltage meters" [136]: They react to the increasing local electrostatic field caused by the increasing positive charge in the carbonyl region by turning up from the bilayer plane. A similar reorienting effect has also been reported for pure phosphatidylcholine bilayers with salt [64, 110]. It is however worth noting that, as we also found (Fig. 4.9), the reorienting by NaCl salt is considerably less prominent than the changes in orientation when the DMTAP mole fraction is changed [45].

Although we were able to measure the average DMPC headgroup orientations very pre-

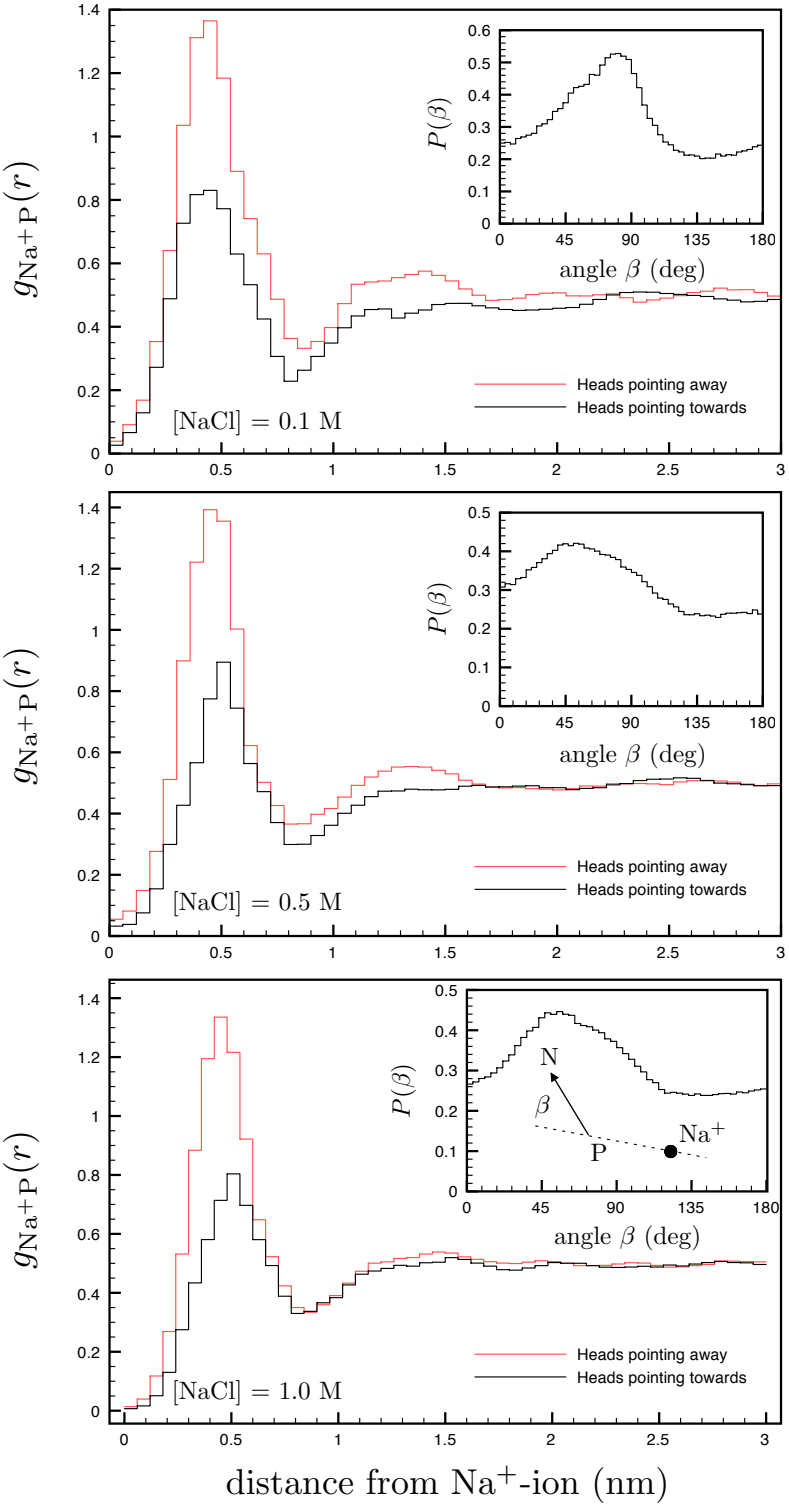

Figure 4.10: Lateral reorientation of the DMPC heads by bound $\mathrm{Na^+}$. Lateral (2D) radial distribution functions—between a complexed $\mathrm{Na^+}$ ion and the phosporus (P) atoms in headgroups of DMPC lipids—split in two according to head group dipole orientation. Inset: distribution of the angle β (between the $\mathrm{Na^+}$–P and P–N vectors projected into the bilayer plane) in the nearest neighbour peak (distance of P from $\mathrm{Na^+}$ less than 0.85 nm). χ_{TAP}=6%.

cisely (Fig. 4.9), one should not forget that the headgroup orientations are in no way tightly fixed. In fact, the typical standard deviations were large in all the systems: roughly 27° when $\chi_{\mathrm{TAP}} = 6\%$, 22° (50%), and 16° (75%), signaling very diverse headgroup orientations among lipids.

Looking at the lateral reorientation of DMPC headgroup dipoles close to a Na^+ ion bound to the membrane, we found that the head group dipoles did undergo electrostaticly induced lateral ordering (Fig. 4.10). The tendency (to point away from the ion) was rather weak and only experienced by the headgroups closest to the Na^+, i.e., those DMPCs that are most likely tied to the same complex by the Na^+ ion in question.

4.1.5 Ordering of lipid chains

Let us now turn our focus from the heads of the lipids to their other main part. Here we discuss the effect of NaCl on the orientation of the lipid tail chains.

Ordering of nonpolar hydrocarbon tails in lipid bilayer is often characterized using the deuterium order parameter S_{CD}, measured using ^{2}H nuclear magnetic resonance experiments. Let θ be the angle between a carbon–deuterium (CD) bond and the bilayer normal. Then S_{CD} is defined as

$$S_{\mathrm{CD}} = \frac{3}{2}\left\langle \cos^2\theta \right\rangle - \frac{1}{2} \tag{4.3}$$

separately for each hydrocarbon group. The brackets denote averaging over time and over lipid molecules. When the chains are fully ordered, $\theta = 90^\circ$ and $S_{\mathrm{CD}} = -1/2$. When the chain is completely disordered, all the angles are equally likely, and $S_{\mathrm{CD}} = 1/4$.

Methods. The explicit positions of the deuteriums have been coarse grained out of our united atom model. They were recovered from the positions of three successive carbons, assuming an ideal tetrahedral geometry of the central CH_2 group [137–139].

We measured S_{CD} separately for each carbon atom in the lipid tails (Fig. 4.1). The measurement periods (given in Fig. 4.2) were divided into intervals of 10 ns, assumed to be statistically independent to estimate the error bars as the standard errors of the mean. Although the S_{CD} for the two (sn-1 and sn-2, Fig. 4.1) tails of the lipids slightly differed, we studied their average to mimic an experimental situation of undistinguishable tails.

To describe the effect of NaCl on the order of the whole tail region with a single number, we calculated for each system the average order parameter S_{ave}. It was defined as the

average S_{CD} of the carbons 2–8 (see Fig. 4.1 for the tail carbon numbering scheme).

Results. Figure 4.11 shows the deuterium order parameter S_{CD} as a function of the tail carbon atom number. Note that here the average S_{CD} of the two tails is shown, and that the y-axis has a negative sign such that more ordered values are those that are further up in the figure. The numbering starts from the headgroup-end of the tails (see Fig. 4.1).

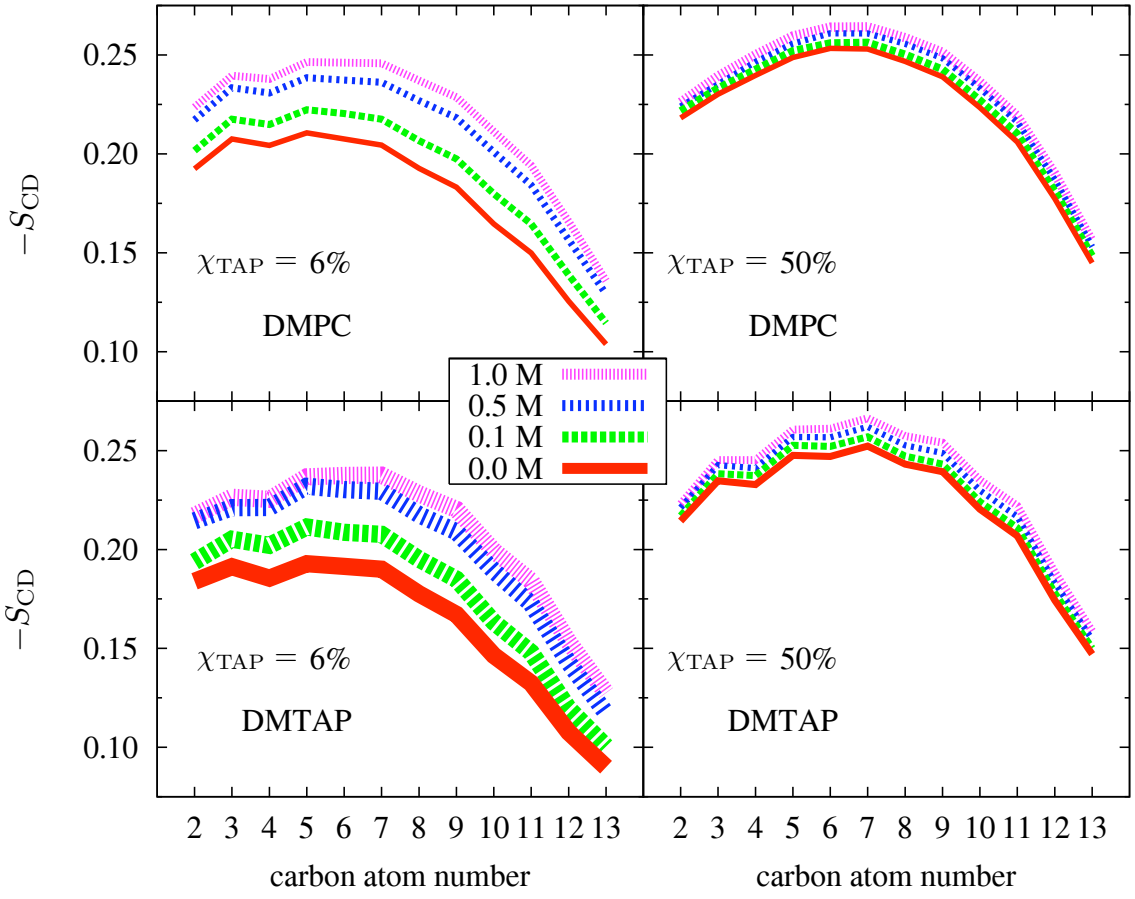

Figure 4.11: Deuterium order parameter S_{CD} averaged over the two tails. DMPC in the top row and DMTAP in the bottom row. The left column has $\chi_{\mathrm{TAP}} = 6\%$, on the right $\chi_{\mathrm{TAP}} = 50\%$. Error bars smaller than the line width. The carbon atom numbers start from the ester region (Fig. 4.1).

The left column shows the bilayer of low cationic lipid content, $\chi_{\mathrm{TAP}} = 6\%$. Order in both DMPC (upper panel) and DMTAP (lower panel) tails was increased by increasing the NaCl concentration. The increase in order was taking place evenly at all the tail carbons.

The right column shows a bilayer of high cationic lipid content, $\chi_{\mathrm{TAP}} = 50\%$. Again an increase in [NaCl] lead to an evenly distributed increase in the tail order. This increase was, however, considerable smaller than that seen for the mildly cationic system.

Figure 4.12 shows S_{ave}, the average S_{CD} over the first seven carbons, as a function of NaCl concentration. Note again the negative sign on the y-axis. Figure 4.12 confirms what was seen already in Fig. 4.11: An increase in [NaCl] increased the order of the lipid tails, the effect being strongest at $\chi_{\mathrm{TAP}} = 6\%$. In addition, in DMPC the tails were more ordered than in DMTAP. The difference between the two lipid types was largest at the low cationic lipid content, $\chi_{\mathrm{TAP}} = 6\%$.

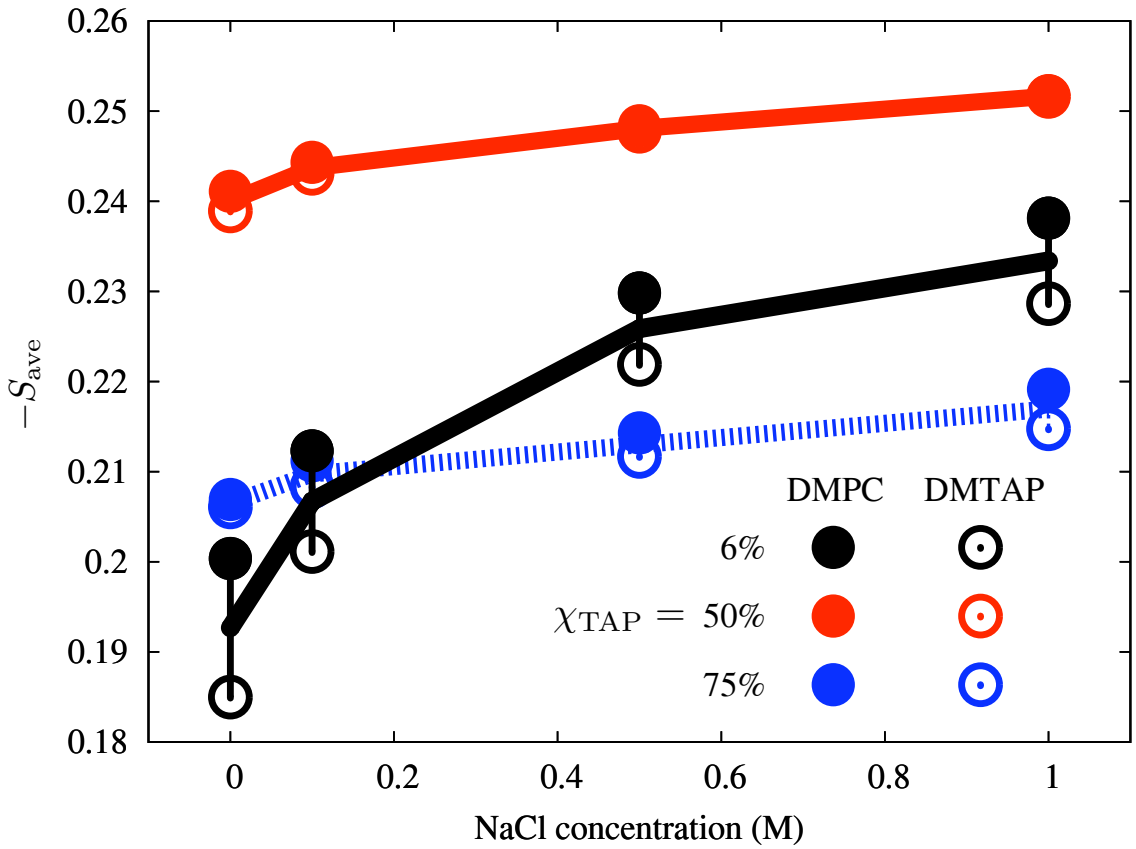

Figure 4.12: Average order parameters S_{ave} as a function of NaCl concentration for all the cationic bilayers. S_{ave} was obtained from S_{CD} (Fig. 4.11) by averaging over carbons 2 to 8. Data for DMPC (solid symbols), DMTAP (hollow symbols) and their average (lines) are shown.

Discussion. We found the lipid tail order to increase with the NaCl concentration. This appeared not, however, to be connected with any particular salt-induced conformational change in the tails, but the increase in order was taking place evenly at all carbon numbers (Fig. 4.11). This suggest the mechanism for ordering to be the general compaction of the bilayer.

Indeed, comparing Fig. 4.12 to Fig. 4.3 reveals a clear connection between the tail order and the area occupied by a lipid. The average order parameter S_{ave} went hand in hand with

the average area per lipid $\langle A \rangle$: An increase in the NaCl concentration lead to an increased order of the lipid chains and a correspondingly decreased the area per lipid. This is in agreement with simulations of pure phosphatidylcholine bilayers with salt [64, 109].

In line with what has been reported before [45], in all the systems where a distinction could be made, DMPCs appeared more ordered than DMTAPs. This suggests that a DMPC lipid would on average also require slightly less area than a DMTAP in a binary bilayer.

4.1.6 Density distributions

So far in this section we have found out that the Na^+ ions were able to bind to the mildly cationic bilayer (Sec. 4.1.2) and to tie DMPC lipids into complexes (Sec. 4.1.3). This gave rise to changes in the average lipid structure both in the headgroups (Sec. 4.1.4) and in the tail region (Sec. 4.1.5).

Now we shall turn towards looking at the electrostatics of the cationic membrane as a large positively charged entity surrounded by saline water. To this end we shall be working mostly with various average profiles along the bilayer normal direction. We start in this subsection by looking at the number density profiles of different molecules and molecular groups across the membrane. These density distributions will give us a solid starting point for studying the electrostatic features of the systems in the later subsections.

Methods. We first measured the density profiles $\rho(z)$ by dividing the simulation box into 200 thin slices (roughly 40 pm in width, depending on the box dimensions) along the bilayer normal (z) direction, counting the mass of molecules or molecular groups falling within each slice, dividing this number by the slice volume, and finally averaging over the whole measurement time (given in Fig. 4.2).

The number density profile $\rho_{\#}(z)$ was then calculated by dividing the density profile $\rho(z)$ by the corresponding molecular mass M:

$$\rho_{\#}(z) = \frac{\rho(z)}{M}. \tag{4.4}$$

To estimate the error in the number density profiles we did not average over the two leaflets, but in the results plotted both $\rho_{\#}(z)$ on top of one another; they were found to overlap within the line width.

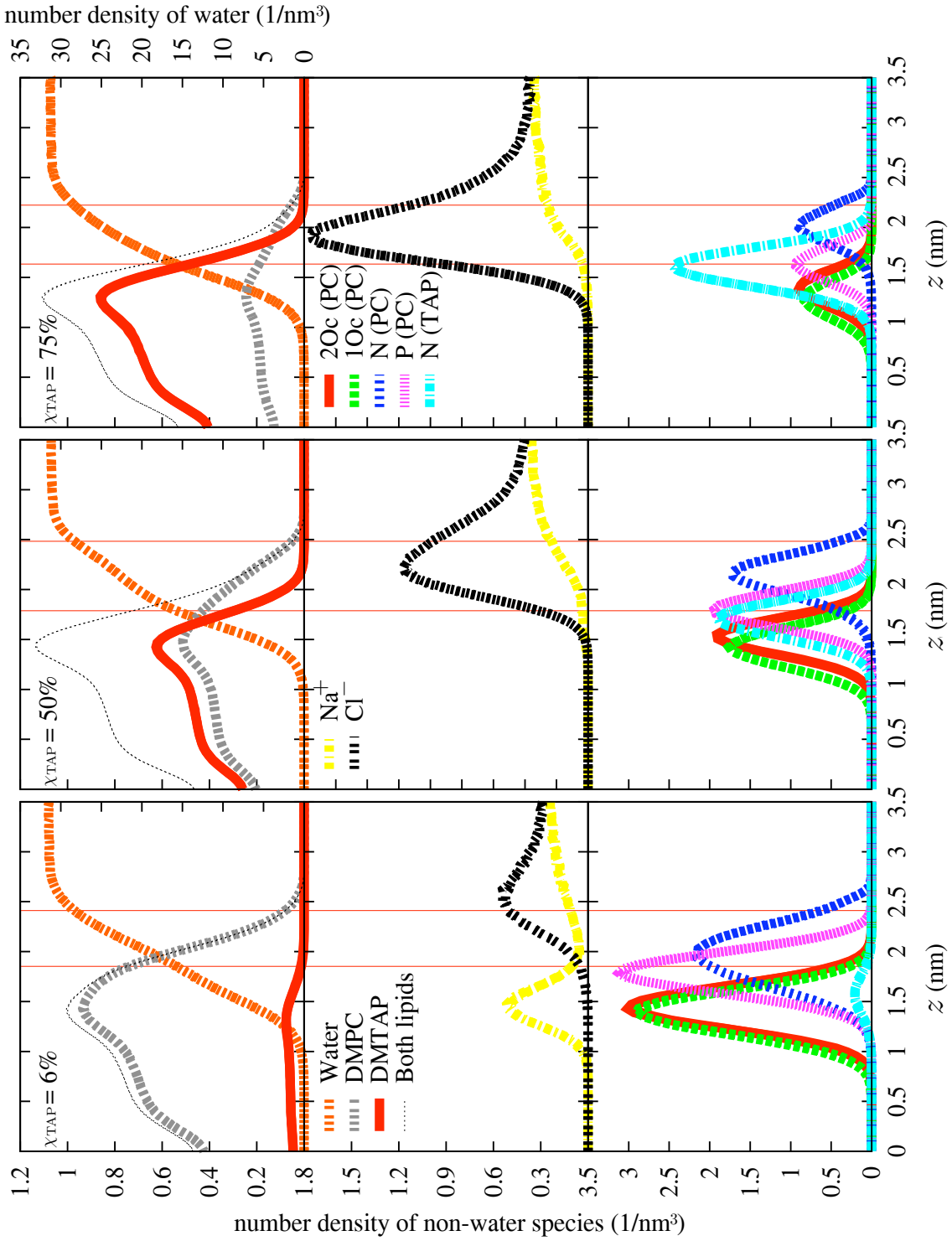

Figure 4.13: The number densities of various molecular species as a function of distance from the bilayer center. The data of each leaflet has been plotted on top of one another to show that the errorbars are within linewidth. The three columns have χ_{TAP}= 6%, 50% and 75% from left to right. [NaCl] = 0.5 M in all. In each column the upper row shows water and the two lipids, the middle row has the ions, and the bottom row the lipid headgroups as well as some carbonyl oxygens. The red vertical lines show the points where water density has reached 50% or 90% of it bulk value, and aim to help comparison with other profiles in this section.

Results. Figure 4.13 shows the number density profiles of lipids, water, ions and some selected molecular groups of the lipids in three of the systems. The salt concentration here was 0.5 M, but the profiles are typical of their corresponding DMTAP mole fractions, χ_{TAP}.

At low cationic lipid content ($\chi_{\mathrm{TAP}} = 6\%$, left column) Na^+ penetrated deep below the DMPC headgroups, all the way until the carbonyl region. There its number density peak aligned nearly perfectly with those of the (DMPC) carbonyl oxygens. Chloride ions, in contrast, stayed in the bulk water or at the water–membrane interface. The Cl^- distribution peaked roughly where the water density reached its bulk value.

At high cationic lipid content ($\chi_{\mathrm{TAP}} = 50\%$, the middle column; 75%, the right column), however, the Na^+ ions were not able to penetrate below the headgroup region, but were located in the bulk water. The Cl^- ions were found mostly in the bulk water too, although drawn closer to the water–membrane interface than in the case of $\chi_{\mathrm{TAP}} = 6\%$.

Discussion. The number density profiles (Fig. 4.13) agreed well with the previously described results of ion binding to the bilayer (Fig. 4.4) and formation of Na^+–DMPC complexes (Figs. 4.5 and 4.8).

An interesting point in Fig. 4.13 is to note is that the carbonyl oxygen of the sn-1 chain was, in fact, deeper in the membrane than that on the sn-2 chain, 2Ocarb. Hence the 2Ocarb oxygens were more easily accessible to the Na^+ ions, making binding to them easier than to the oxygens in the sn-1 chain. (See Fig. 4.1 for the naming of the lipid parts.)

Notably, the distance between the DMPC headgroup phosphorus and nitrogen increased with χ_{TAP}. This is a sign of the DMTAP-induced reorientation of the headgroups [45].

4.1.7 Charge densities

In this subsection we shall look specifically at the distribution of charged entities across the bilayer. The main motivation for this is the need for these distributions for calculating the other electrostatic properties of the membrane in the upcoming subsections, but familiarity with the charge distributions themselves does provide intuition on those derived quantities too.

Methods. We measured the charge profiles in each system by dividing the simulation box into 150 slices (approximately 50 pm in width, depending on the box dimensions) along the bilayer normal (z) direction, counting the total charge of the entities of interest within each slice, dividing it by the slice volume, and averaging over all the frames saved during the measurement time (given for each system in Fig. 4.2). The error was estimated in a similar manner as for the density profiles (Sec. 4.1.6), namely plotting distributions from each leaflet on top of another.

Results. For each cationic bilayer, Fig. 4.14 shows typical charge distribution profiles across a membrane leaflet. Here [NaCl] = 0.5 M. Contributions from the lipids (DMPC and DMTAP), the ions (Na^+ and Cl^-), and the water molecules are shown separately.

Although the zwitterionic DMPC lipids have no net charge, their charge distribution profile had a distinctive wave-like shape. The 'wave', its wave-length slightly exceeding 1.5 nm, comprised a strong negative peak starting right after the lipid tail region ($z < 1.0$ nm), immediately followed by a positive peak of similar size. The cationic DMTAP lipids had just a single positive peak with no negative components in their charge profiles.

The Na^+ and Cl^- ion distributions are, by definition, their number density distributions weighted by their charge. In bulk water the two ion types mostly neutralized one another.

The dipolar nature of water is seen in its bumpy charge density profile. By orienting on average along the local electrostatic field, the water molecules did create a considerable contribution to the charge. Notably, the shape of their profile changed qualitatively between $\chi_{\mathrm{TAP}} = 50\%$ and 75%, as the positive peak closer to the bilayer center disappeared.

At $\chi_{\mathrm{TAP}} = 6\%$, the positive charges of DMTAP and Na^+ bound to the carbonyl region appeared to be overcompensated by the negative DMPC-charge residing at the same distance from the bilayer center. At $\chi_{\mathrm{TAP}} = 50\%$, the positive peak of DMTAP appeared to be able to slightly overcompensate the negative contributions from DMPC and water. At $\chi_{\mathrm{TAP}} = 75\%$, the positive peak of DMTAP headgroups could not to be compensated even by the combined effect of the small negative DMPC peak and the negative local contribution of water; the resulting strong positive wall charge potently attracted the Cl^- ions.

Discussion. The wave-like signature of the DMPCs was a prominent feature in all the charge density profiles (Fig. 4.14). Interestingly, the minimum of the DMPC charge

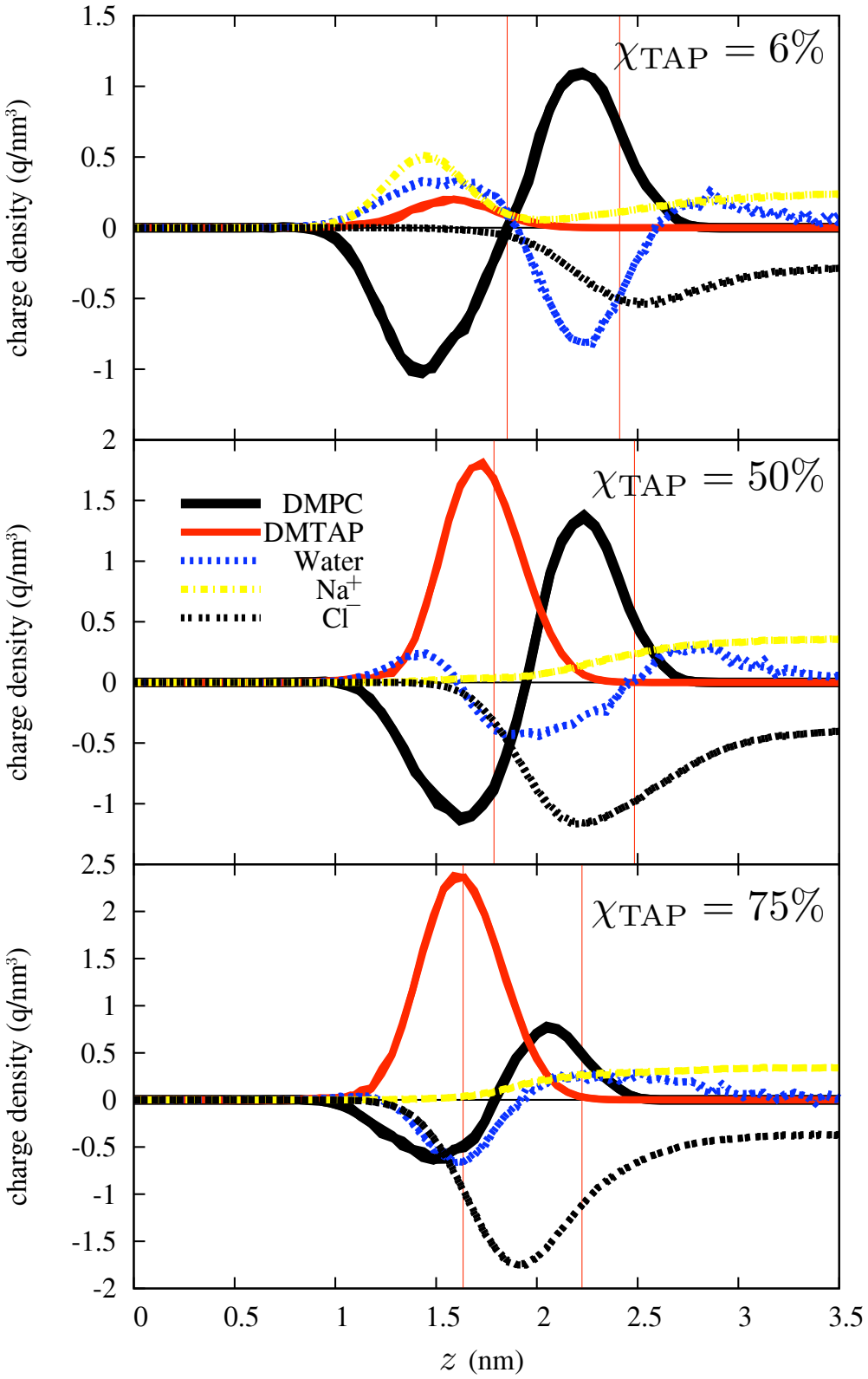

Figure 4.14: The distribution of charge along the bilayer normal in three systems with [NaC]=0.5 M: χ_{TAP}=6%, 50% and 75% from top to bottom. The data of leaflets are plotted one over the other to provide a reliability estimate.

profile did not coincide with the maximum of the P-peak (Fig. 4.13). In particular at $\chi_{\mathrm{TAP}} = 6\%$ the minimum rather resided in the carbonyl region, thus explaining why the Na^+ ions did bind so keenly to the carbonyl region of this mildly cationic membrane.

Indeed, for $\chi_{\mathrm{TAP}} = 6\%$, the negative DMPC peak was greatly uncompensated by the positive DMTAPs and the carbonyl-bound Na^+ ions (Fig. 4.14). Thus, in purely electrostatic terms, it would have been apt for even more Na^+ to enter the carbonyl region to level down the local charge imbalance. Already at $\chi_{\mathrm{TAP}} = 50\%$ and particularly at 75%, however, the positive DMTAP peak easily overcompensated the negative DMPC peak, making it electrostaticly impossible for Na^+ ions to be permanently bound to the carbonyl region.

The disappearance of the peak closest to bilayer center in the water charge density profile between $\chi_{\mathrm{TAP}} = 50\%$ and 75% has been reported previously [45].

4.1.8 Surface charge density

Our cationic membranes have a substantial positive charge, but can not (Fig. 4.14) exactly be considered as ideal planar charged surfaces. It is thus interesting to explore how the monovalent NaCl salt affects the electric surface properties of these non-ideal rough walls, characterized by a broad interfacial region between the wall and the bulk water.

In this subsection we study how the surface charge profile $\sigma(z)$, defined as

$$\sigma(z) = \int_0^z \rho_{\mathrm{e}}(z')dz' \tag{4.5}$$

varies across a membrane leaflet; $\rho_{\mathrm{e}}(z)$ is the charge density excluding water [109] at distance z from the bilayer center.

Methods. For each system we calculated $\rho_{\mathrm{e}}(z)$ by simply summing the average charge density profiles (excluding that of water) measured before (Sec. 4.1.7) and averaging the outcome over the two leaflets. The average surface charge density $\sigma(z)$ across a leaflet was then obtained by numerical integration of $\rho_{\mathrm{e}}(z)$ from $z = 0$ (bilayer center) to z.

Results. Figure 4.15 shows the surface charge density profiles $\sigma(z)$ for all the studied membranes. At the center of bilayer, in the nonpolar hydrocarbon chain region ($z < 1.0$ nm), the surface charge was naturally zero for all the systems. A less trivial common feature in all the cases was the region of negative surface charge right after the tail region.

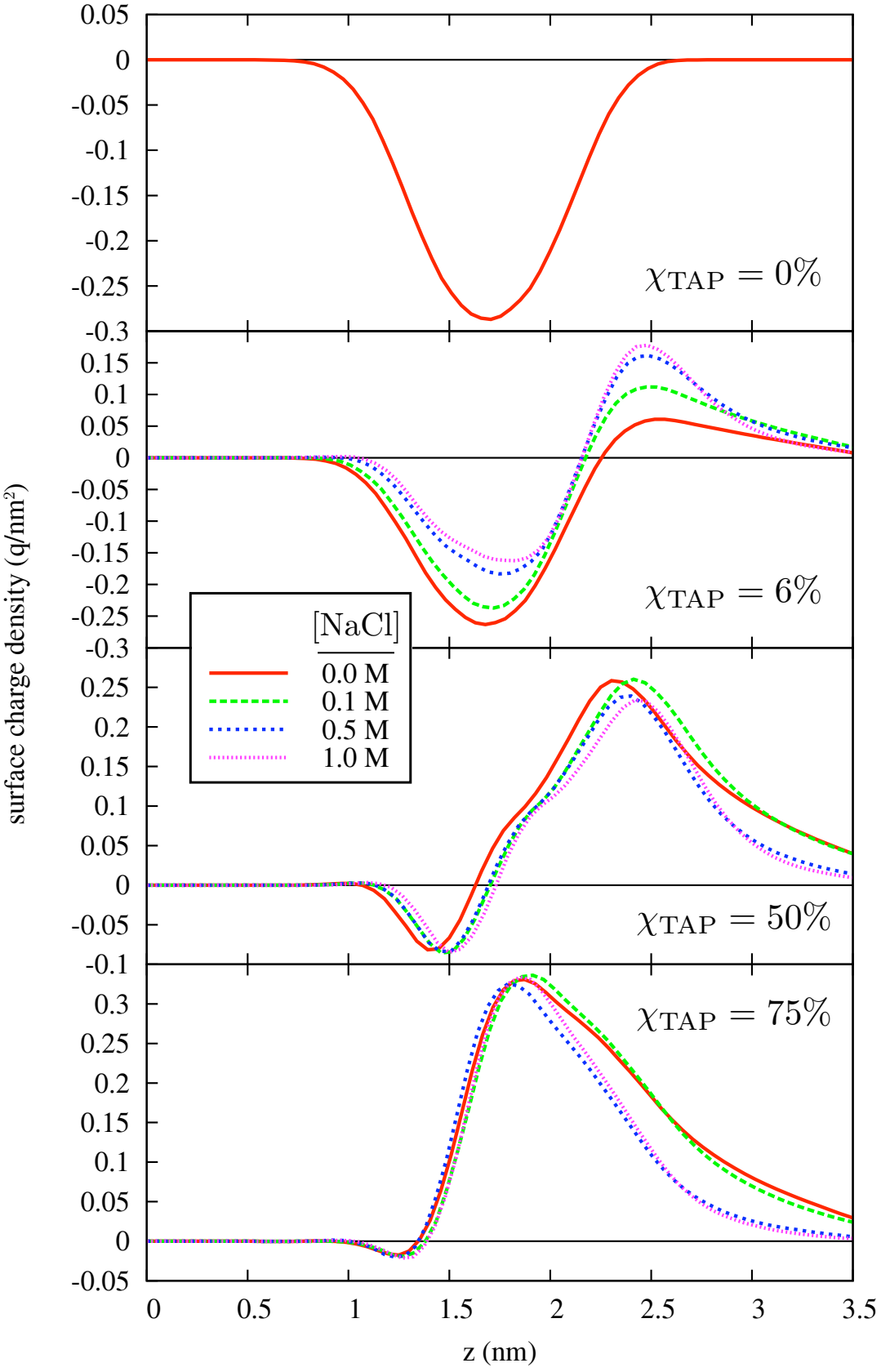

Figure 4.15: The surface charge density profiles of the bilayers (excluding water) as function of distance from the bilayer center.

This region was largest for pure DMPC, and got smaller with increasing DMTAP fraction, χ_{TAP}, but was still clearly visible even for $\chi_{\mathrm{TAP}} = 75\%$.

After this initial negative dip a common feature among all the cationic systems was that the surface charge turned positive. In other words, all the cationic membranes indeed appeared as positively charged surfaces to the bulk water. The actual shapes of the $\sigma(z)$ curves, as well as the changes caused on them by changes in the salt concentration, were dependent on the cationic lipid content of the bilayers.

At $\chi_{\mathrm{TAP}} = 6\%$ the negative surface charge region was extensive and its minimum deep. When NaCl was added, the minimum of $\sigma(z)$ curves shifted further away from the bilayer center and decreased in depth. Notably also the positive maximum moved towards the bilayer center and increased in height, making the bilayer to appear increasingly positive to the bulk water.

At $\chi_{\mathrm{TAP}} = 50\%$ the negative surface charge region was considerable smaller than for $\chi_{\mathrm{TAP}} = 6\%$, and its minimum shallower. In addition, the region was not markedly affected by changes in the NaCl concentration. However, large amounts of NaCl slightly decreased the height of the positive surface charge peak.

At χ_{TAP}=75% the negative surface charge region had almost disappeared. The depth of the negative well, as well as the height of the positive peak in $\sigma(z)$, appeared insensitive to changes in [NaCl].

Discussion. All the cationic bilayer systems appeared positive to the bulk water; on the other hand they displayed a region of negative surface charge between this water-facing region and the neutral tail region (Fig. 4.15).

The effects of NaCl on the surface charge profiles $\sigma(z)$ depended on the DMTAP mole fraction (Fig. 4.15). To understand the key features in $\sigma(z)$ it is instructive to look at the charge density profiles. To this end Fig. 4.16 displays the charge density profiles of the two most relevant species for each χ_{TAP}.

For $\chi_{\mathrm{TAP}} = 6\%$, comparing Figs. 4.15 and 4.16 reveals that the extensive region of negative surface charge was caused by the DMPC lipids. The Na^+ ions were then responsible for pushing the surface charge minimum further from the bilayer center, and decreasing its depth, as salt concentration increased. Interestingly, adding NaCl does in fact increase the negative contribution from DMPC (upper panel in Fig. 4.16), because Na^+ binding to the carbonyl region reorients the DMPC headgroups (Fig. 4.9). This local increase of

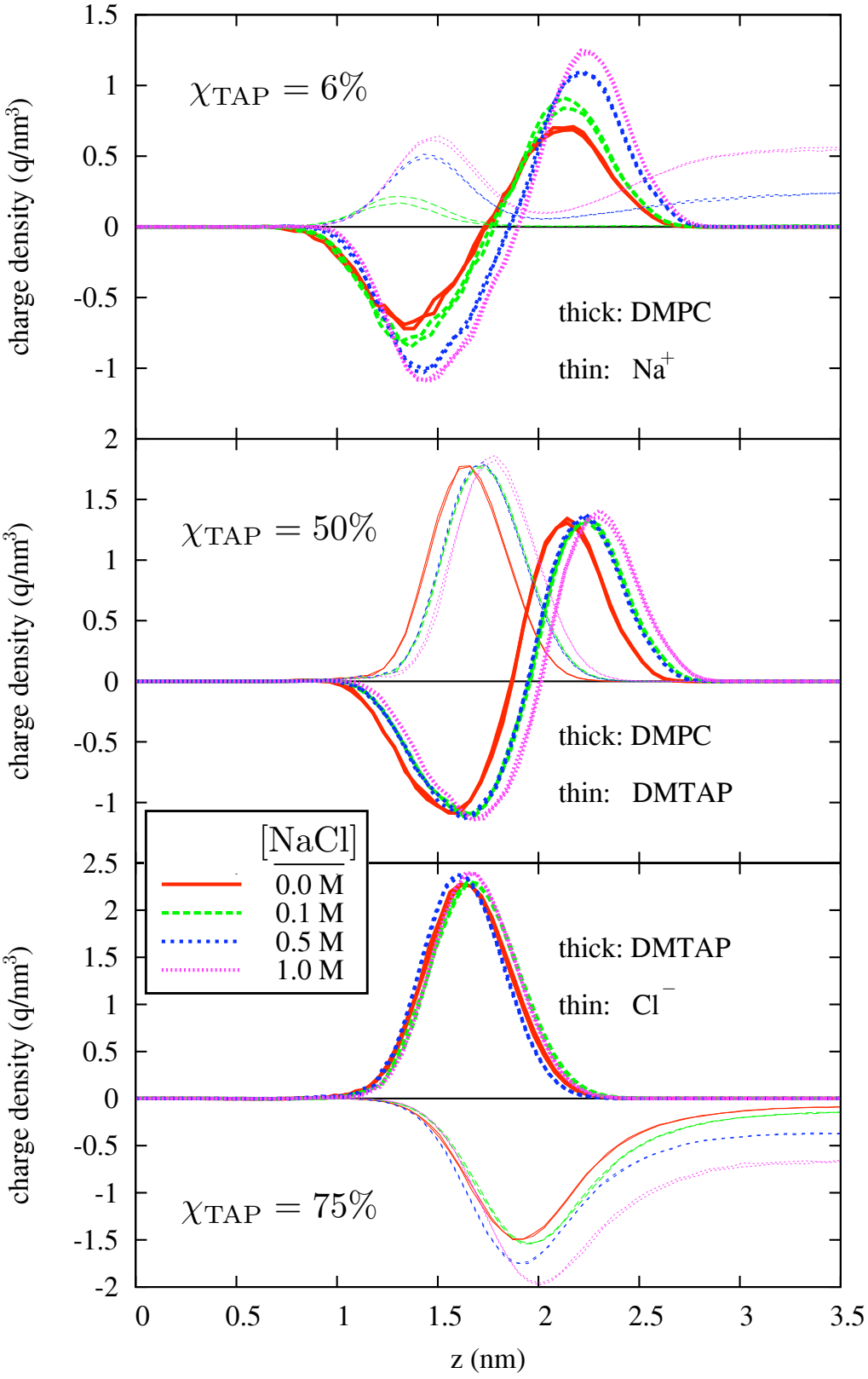

Figure 4.16: Charge densities of the components that explain the key features of the corresponding surface charge density plots (Fig. 4.15); χ_{TAP}=6%, 50%, 75% from top to bottom. The data for both leaflets plotted on top of one another to allow an estimate for measurement error. For measurement details see Sec. 4.1.7.

negative $\sigma(z)$ is, however, overcompensated by the simultaneous increase in the positive Na^+ peak itself.

These findings are in line with previous reports that the surface charge profile of a pure phosphatidylcholine membrane is fully negative, but develops a small positive component (making the membrane to appear as a slightly positive surface to the bulk water), when NaCl salt is added [109].

Figure 4.16 reveals also the main cause for the changes observed in the positive surface charge peak at $\chi_{\mathrm{TAP}} = 6\%$: increase in height and displacement closer to the bilayer center (Fig. 4.15). Somewhat surprisingly, it turns out that the Na^+ distribution is not directly responsible for these effects. In fact, it has hardly any contribution in its charge density at the location of the positive surface charge peak. Instead, the increase and the displacement are caused by the reorientation of the DMPC headgroup, which lead to an increase in the positive charge density contribution coming from the DMPCs.

For $\chi_{\mathrm{TAP}} = 50\%$, comparing Figs. 4.15 and 4.16 shows that the less pronounced negative surface charge region (compared to the mildly cationic bilayer) was quite naturally caused by the DMTAPs. They were namely able to compensate most of the negative contribution of the DMPCs, except for a small portion concentrated around $z \approx 1.5$ nm. Because the Na^+ ions were not able to bind to the bilayer at this DMTAP molar fraction, the salt concentration did not affect the negative $\sigma(z)$-region. However, adding more NaCl did slightly decrease the height of positive peak of the $\sigma(z)$, as concentration of Cl^- close to the membrane was increasing more than that of Na^+.

For χ_{TAP}=75%, Fig. 4.16 clearly shows that the positive charge of the DMTAPs dominated, and thus the negative surface charge region had almost disappeared in Fig. 4.15. Further, the features of the negative charge density peak were unaffected by NaCl, because the Na^+ could not reach the carbonyl region at all.

Also the height of the positive peak in $\sigma(z)$ appeared insensitive to changes in [NaCl]. This can be understood by comparing the lowest panels in Figs. 4.15 and 4.16. There were no changes in the DMTAP charge density distribution (responsible for the positive peak in $\sigma(z)$) when the salt concentration increased. In addition, there we no changes in the Cl^- penetration depth, as only the height of the Cl^- charge distribution peak, not its leading edge, moved. Thus the surface charge density reached its maximum unaffected at all salt concentrations, and the increase in the Cl^- charge density peak affected only the rate at which the surface charge density decayed, not its maximal value.

4.1.9 Electrostatic potential

The electrostatic membrane potential is a key player in many membrane-mediated biological phenomena. The most notable example is the propagation of action potential in neural cells [140, 141], but the orientation of membrane-spanning proteins [142], the membrane fusion of viruses [143], and the programmed cell death [144], among many other phenomena appear to depend on the electrostatic membrane potential as well.

Our membranes were symmetric (Sec. 3.5) and the systems on the whole in equilibrium (Fig. 4.2), thus on average no net electrostatic potential difference could prevail over the bilayer. It is, however, instructive to the study the electrostatic potential profile $V(z)$ across the membrane and the effects of monovalent NaCl salt on it.

In this subsection we study how $V(z)$, obtained by a double integration of the Poisson equation

$$V(z) = -\frac{1}{\epsilon_0}\int_0^z \frac{1}{\epsilon_r(z')}\int_0^{z'} \rho_{\mathrm{i}}(z'')dz''dz', \tag{4.6}$$

varies across a membrane leaflet. Here $\rho_{\mathrm{i}}(z)$ is the charge density including water at the distance z from the bilayer center, ϵ_0 the vacuum permittivity, and $\epsilon_r(z)$ the relative permittivity profile.

Methods. For each system we calculated $\rho_{\mathrm{i}}(z)$ by simply summing the average charge density profiles (of all the the components of the system) measured before (Sec. 4.1.7) and averaging the outcome over the two leaflets.

The relative permittivity profile $\epsilon_r(z)$ was estimated from the corresponding number density profile of water ($\rho_{\#\mathrm{H_2O}}(z)$, see Fig. 4.13) using

$$\epsilon_r(z) = 2.0 + 68.0 \times \frac{\rho_{\#\mathrm{H_2O}}(z)}{\rho_{\#\mathrm{H_2O}}(\text{in bulk})}. \tag{4.7}$$

Such that inside the hydrocarbon tail region $\epsilon_r(z \lesssim 1.0\ \mathrm{nm}) = 2.0$, in the bulk water $\epsilon_r(z \gtrsim 3.0\ \mathrm{nm}) = 70.0$, and in the interfacial region the shape of the water density profile was followed.

The average electrostatic potential profile $V(z)$ across a leaflet was then obtained by double numerical integration of Eq. (4.6).

Results. Figure 4.17 shows the average electrostatic potential profile $V(z)$ across a leaflet for each of the simulated systems. All the $V(z)$ displayed a shape that had a minimum around $z = 1.0$ nm, followed by a maximum around $z = 1.5$ nm, and dropping again to the bulk water region.

This shape was most distinctively displayed in the pure DMPC system; upon adding more DMTAP the maximum became smaller an smaller, and the drop to the bulk deeper and deeper. At $\chi_{\mathrm{TAP}} = 75\%$, a potential difference of almost -30 mV was reached between the bilayer center and the bulk water.

The effect of NaCl was most prominent for the mildly charged bilayer, $\chi_{\mathrm{TAP}} = 6\%$. With increasing [NaCl] the minimum became deeper, whereas the maximum value did not show a systematic change. The positions of both extrema were, however, pushed further away from the bilayer center. The bulk value of the electrostatic potential was affected only with the highest NaCl concentrations, where a drop ($\lesssim 5$ mV) was observed.

Similar behaviour was seen also when $\chi_{\mathrm{TAP}} = 50\%$, but the modifications of the potential profile were even slighter than for $\chi_{\mathrm{TAP}} = 6\%$. For $\chi_{\mathrm{TAP}} = 75\%$ the salt-induced changes to the $V(z)$ were vanishingly small.

Discussion. The electrostatic potential difference between the bulk water and the bilayer center was of the order of few tens of millivolts. This is in a stark contrast to the potential differences typically reported in lipid bilayer simulations, which are of the order of one Volt [66]. For example, for the systems shown in Fig. 4.17, potential differences of 0.6 V (pure DMPC), 1.0 V ($\chi_{\mathrm{TAP}} = 50\%$) and 1.2 V (75%) have been reported [45]. The reason for the discrepancy is that in earlier simulational work a flat permittivity profile $\epsilon_r(z) = 1$ has been used for the second integration in Eq. (4.6).

If the potential difference between the bulk and the middle of bilayer would be of the order of a Volt, a monovalent ion would gain 1 eV $\approx 40 k_B T$ of electrostatic energy by moving to the tail region. As the ions are typically not seen to gather within the membrane, it seems plausible that the permittivity of the medium, $\epsilon_r(z)$, should be taken into account when calculating $V(z)$.

One should note, however, that we have just estimated $\epsilon_r(z)$ using Eq. (4.7), not measured it. To find $V(z)$ with high accuracy one could measure the average electrostatic potential experienced by a test charge at z. This was beyond the scope of the present study, but could be done either during the simulation or by performing a re-run on the

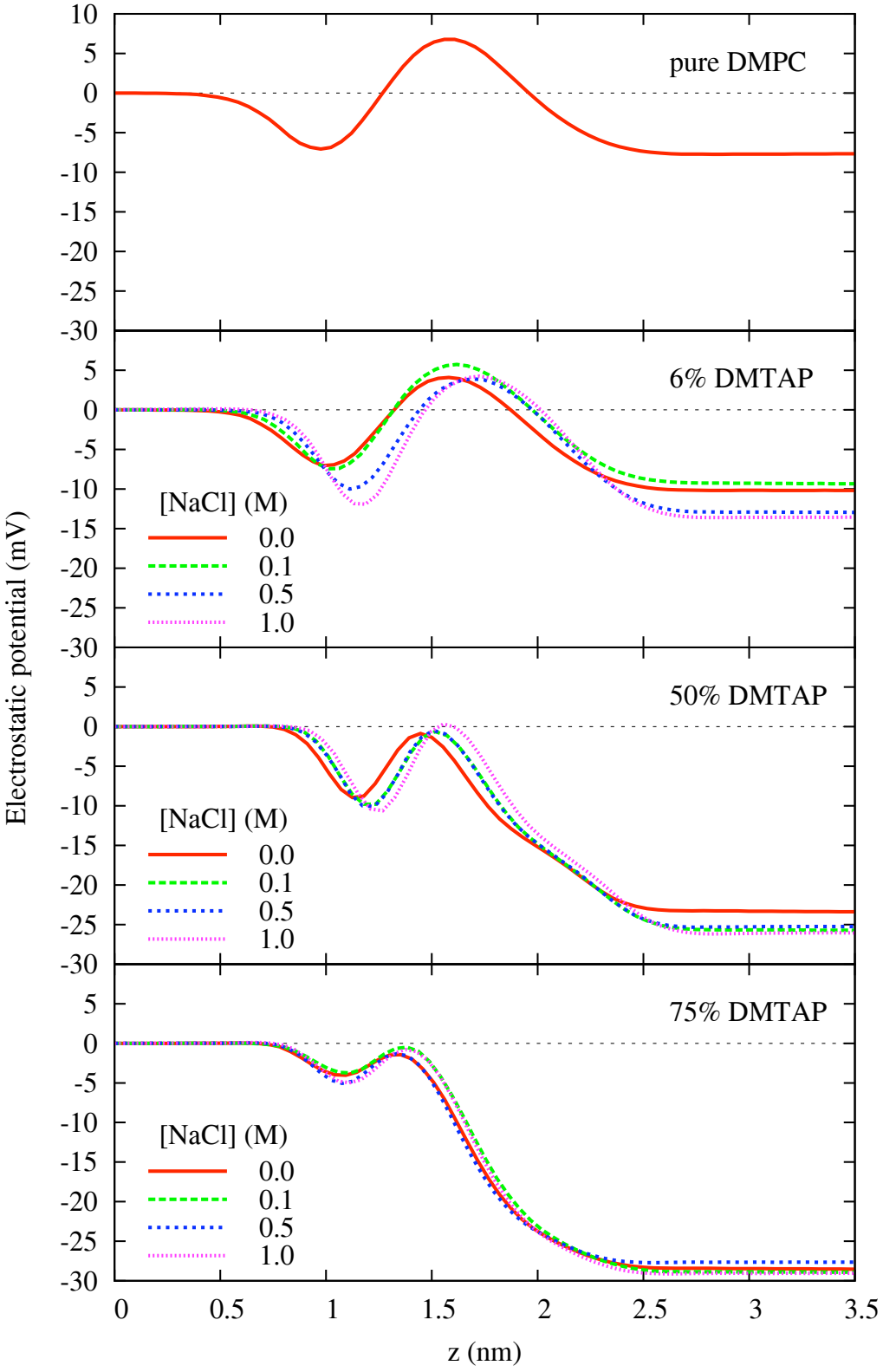

Figure 4.17: Electrostatic potential as a function of distance (z) from the bilyer center. All the 13 simulated systems shown. DMTAP mole fraction goes from pure DMPC (top), via $\chi_{\mathrm{TAP}} = 6\%$, and 50%, to 75% (bottom). Lines show different NaCl concentrations. For pure DMPC no simulations with NaCl were made (Table 3.1).

saved frames. Further, from the accurate $V(z)$ and $\rho_{\rm i}(z)$ one could determine reliably the relative permittivity profile $\epsilon_r(z)$ using Eq. (4.6).

Let us now turn to the details of the actual electrostatic potential profiles $V(z)$ in Fig. 4.17. The distinct (tails–minimum–maximum–water) shape of the profiles was clearly caused by the DMPC lipids, as it was purest in the pure DMPC system and evolved further away from it with each addition of DMTAP. One could speculate that the potential profile of a pure DMTAP bilayer would consist of no minima around $z = 1.0$ nm, but the potential would simply decay in a monotonic way from the tail region to the value in the bulk water.

It was again found that the effect of monovalent salt depended on the cationic lipid content of the bilayer (Fig. 4.17). The modifications in $V(z)$ seen for $\chi_{\rm TAP}$ = 6% with increasing NaCl concentration appear related to the reorientation of the DMPC headgroups (Fig. 4.9). Although it does not quite explain the slight changes seen for $\chi_{\rm TAP}$ = 50%, this explanation would be well in line with the fact that at highest DMTAP fraction, $\chi_{\rm TAP}$=75%, there was no major change in the electrostatic potential with NaCl concentration.

4.1.10 Comparison to Poisson–Boltzmann theory

Let us end our discussion of the electrostatic properties with a comparison to the predictions of the Poisson–Boltzmann theory. As discussed in Chap. 2, this is a mean field theory, thus neglecting fluctuations and correlations. In addition it assumes the ions to be point-like and the water a continuum. It does, however, benefit from its simplicity and the intuitive picture of electrostatic phenomena it provides.

Methods. For the cationic membranes having no NaCl salt (see Table 3.1), we fitted $\rho_{\#{\rm Cl}^-}(z)$, the number density profiles obtained in Sec. 4.1.6 for the $\rm Cl^-$ counter ions, to the predictions given by the Poisson–Boltzmann theory for $\rho_-(z)$, the counter ion density profile in the two-plate setup in absence of salt

$$\rho_-(z) = \frac{\rho_{\rm m}}{\cos^2(Kz)}. \tag{4.8}$$

Note that here z is the distance from the midplane of the water slab between two periodic images of the bilayer, $\rho_{\rm m}$ is the counterion density at $z = 0$, and $K = \sqrt{2\pi\ell_B n_{\rm m}}$. Because $\rho_{\rm m}$ was fixed by the value of $\rm Cl^-$ number density at the midplane, $\rho_{\rm m} = \rho_{\#{\rm Cl}^-}(0)$, the only parameter left for fitting was K, i.e., essentially the Bjerrum length ℓ_B. The error of

the fit was estimated visually.

For all the 13 systems the validity of the fundamental Poisson–Boltzmann assumption

$$\rho_{\pm}(z) = \rho_{\pm}^{0} e^{\mp V(z)/k_B T} \tag{4.9}$$

was studied. Here $\rho_{\pm}(z)$ is the number density of an ion species (Na^{+}, Cl^{-}) and $V(z)$ the average electrostatic potential at position z, $\rho_{\pm}^{0}$ is the reference density at $V \to 0$, and $k_B T$ the thermal energy. The number density profiles $\rho_{\#\mathrm{Na}^{+}}(z)$ and $\rho_{\#\mathrm{Cl}^{-}}(z)$ were obtained in Sec. 4.1.6. The potential profiles $V(z)$ including water were obtained in Sec. 4.1.9; the profiles excluding water were obtained in a similar manner as described in Sec. 4.1.9, but $\rho_{\mathrm{e}}(z)$, the charge density profile excluding water (see Sec. 4.1.8) was used. For $\rho_{\pm}^{0}$ the input number densities $0.60221/\mathrm{nm}^3$ ([NaCl] = 1.0 M), $0.30111/\mathrm{nm}^3$ (0.5 M), and $0.06022/\mathrm{nm}^3$ (0.1 M) were used. The zero-level of the potential was taken to be in the midplane of the water slab. No parameters were fit.

Results. Figure 4.18 compares the counter ion (Cl^{-}) density profiles measured directly from the simulation (Sec. 4.1.6) and predicted by the Poisson–Boltzman (Gouy–Chapman) theory (Eq. (4.8)). As the counter ion density at the midplane of the water slab was rather far from zero (Fig. 4.18), the two-plate solution of the Poisson–Boltzman equation was used.

There was one parameter, K, to fit in Eq. (4.8). In practice K controls the distance between the walls. As Fig. 4.18 shows, the fits appeared to give a reasonably good correspondence between the theory (thin lines) and the direct measurements (thick lines). In particular, the fits were good within the water region.

Fitting K, however, was equal to fitting the Bjerrum length $\ell_B = K^2/2\pi n_{\mathrm{m}}$, which should in bulk water at 323 K have a fixed value of 0.74 nm. We obtained values $\ell_B = 0.8 \pm 0.1$ nm ($\chi_{\mathrm{TAP}} = 6\%$), 1.20 ± 0.02 nm (50%), and 1.21 ± 0.02 nm (75%). We took this inconsistency as a sign that the simplified geometry of flat hard walls used to solve the Poisson–Boltzmann equation was inappropriate for our rough and porous walls. Fitting to the more complicated ion profiles, which the analytic theory predicts in the presence of added electrolyte, was thus not considered reasonable.

Instead we focused on studying the validity of the basic assumption of the Poisson–Boltzmann theory, Eq. (4.9), that the ion distributions are determined by the Boltzmann weight of the average electrostatic interactions.

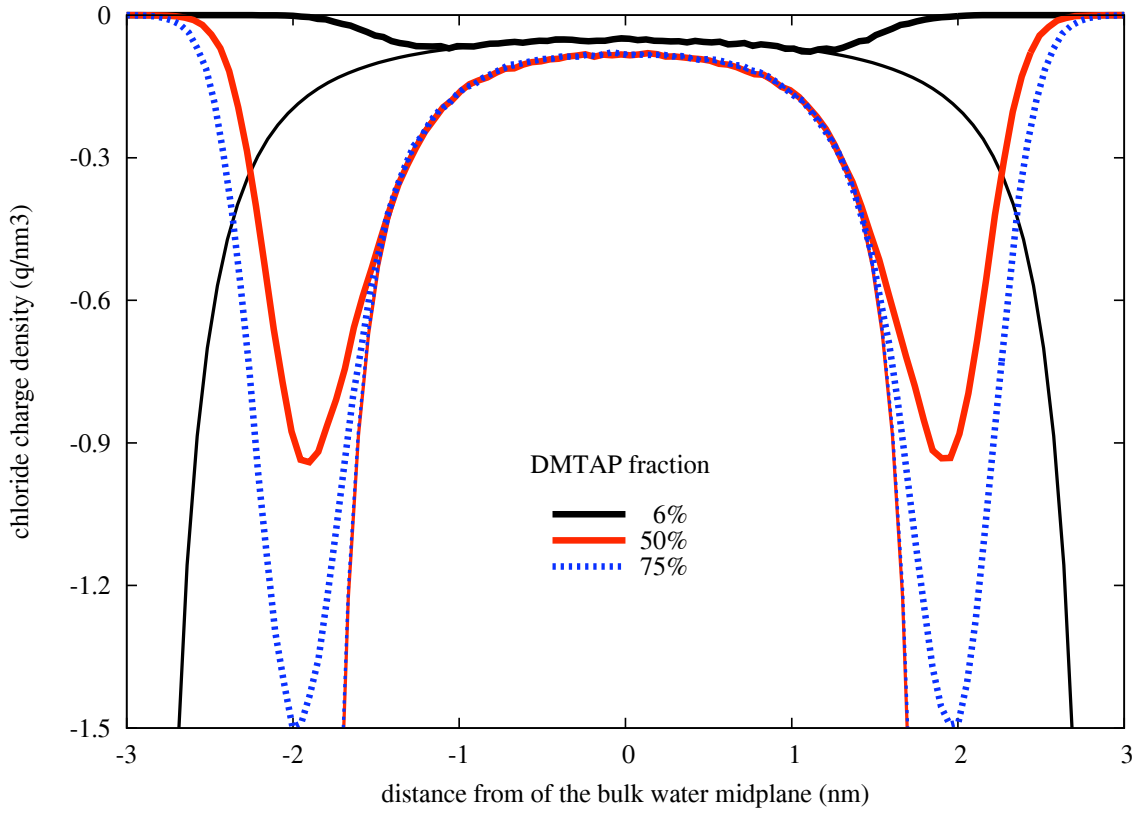

Figure 4.18: Comparison of the Cl^- counter ion profiles, measured directly from the simulation (thick lines) and determined from the Poisson–Boltzmann theory (thin lines). All the systems in the absence of NaCl salt. The two-plate boundary conditions used for the theory (Eq. (4.8)). Note that z is the distance from the midplane of the water slab between two periodic bilayer images.

Figure 4.19 compares the ion density profiles measured directly from the molecular dynamics simulations (Sec. 4.1.6) and those obtained by inserting the electrostatic potential profiles (Sec. 4.1.9) into Eq. (4.9). The upper quadruplet shows the results when charge density of water was excluded from the determination of the potential profile $V(z)$. In the lower one water was included. It appeared that excluding water from the $V(z)$ gave results more consistent with the direct measurement, so let us focus on it.

Among the four subplots the upper row has the mildly cationic system, $\chi_{\mathrm{TAP}} = 6\%$, the lower row the strongly cationic one, $\chi_{\mathrm{TAP}} = 75\%$. In both rows the left column has NaCl concentration of 0.1 M, the right one 1.0 M.

In the strongly charged bilayer the theory seemed to overestimate the height on the Cl^- peak. It was also overestimated in the mildly charged bilayer at the high salt concentration. In the mildly charged bilayer system with small amount of NaCl the theory seemed to estimate the shape of the Cl^- number density profile rather well.

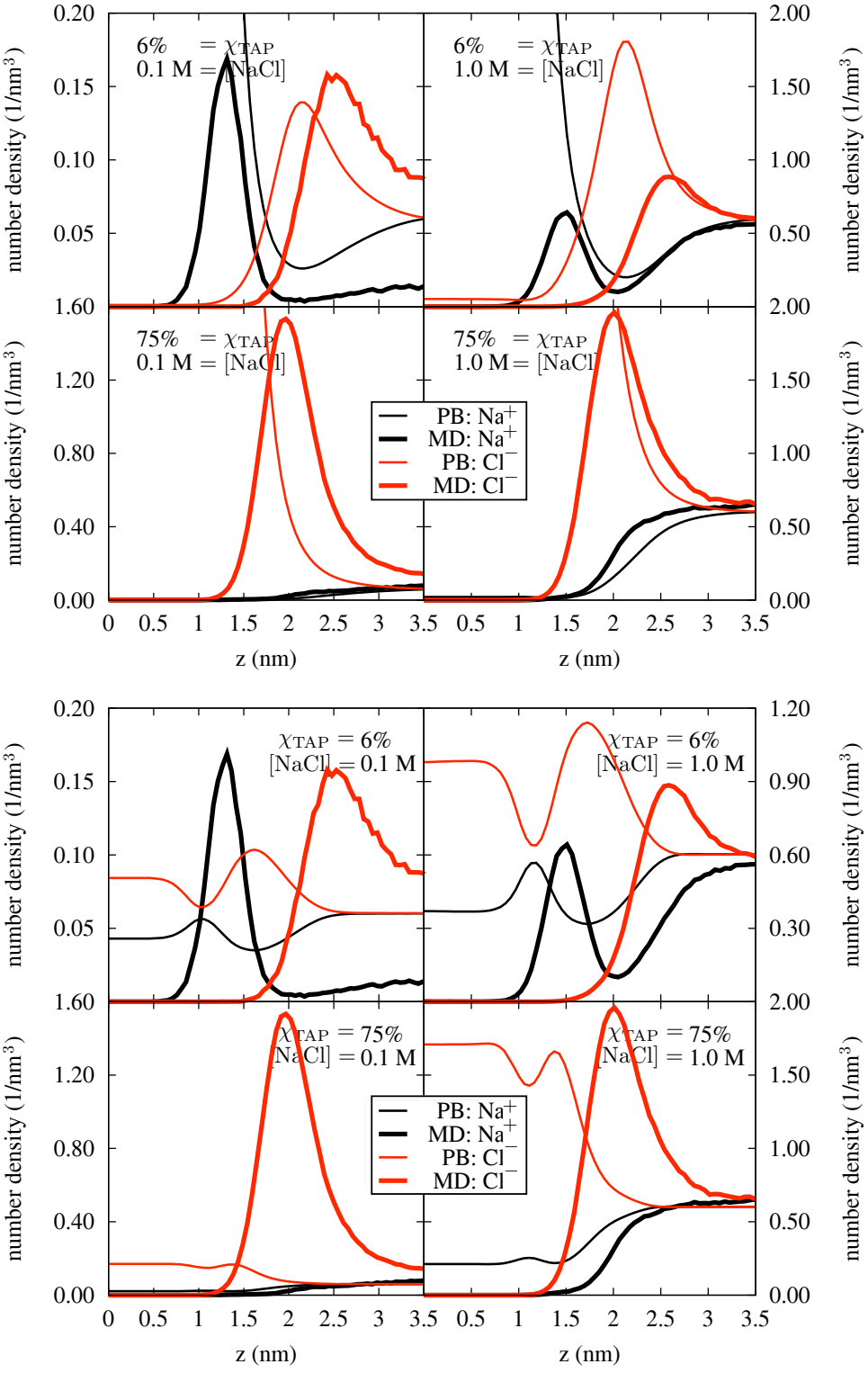

Figure 4.19: Comparison of Poisson–Boltzmann theory with molecular dynamics results. The upper panel is excluding water. The lower panel is including water. In both panels the upper row has χ_{TAP}=6%, [NaCl]=0.1 M on the left and 1.0 M on the right. The lower row has the same for χ_{TAP}=75%.

The height of the Na^+ peak was overestimated at low χ_{TAP}, whereas it was quite correct in the strongly charged system. The shape of the Na^+ number density profile was rather correct at both low and high χ_{TAP}, as well as low and high [NaCl].

Discussion. The basic assumption of the Poisson–Boltzmann theory, Eq. (4.9), appeared to hold reasonably well for all our systems.

In particular, when the contribution of water was excluded from the electrostatic potential profile $V(z)$, the correspondence between the Poisson–Boltzmannian and the directly measured ion number density profiles was good (Fiq. 4.19). It is worth noting that no fitting was performed on the curves given in Fig. 4.19. Therefore, because the concentrations of Cl^- and Na^+ were not always equal in the midplane of the water region (in particular in the system where $\chi_{\mathrm{TAP}} = 6\%$ and [NaCl] = 0.1 M), the agreement between theory and simulation could have been made even better by fitting the co- and counter ion distributions separately.

To our knowledge there is no previous work directly studying the validity of the Poisson–Boltzmann theory in a manner described here. The reason lies most likely in the fact that the traditional way of measuring the electrostatic potential $V(z)$ has lead to potentials that are orders of magnitude larger than what we obtained (Sec. 4.1.9). Taking the exponential of these, as required by Eq. (4.9), leads to completely unphysical ion density profiles. We consider this as one more argument supporting the validity of the method we used for determining $V(z)$ in Sec. 4.1.9.

It is quite fascinating that Böckmann and coworkers [64] numerically solved the Poisson–Boltzmann equation for a phosphatidylcholine bilayer using the lipid charge distribution obtained from a molecular dynamics simulation as a boundary condition. They found similar agreement between their simulational and theoretical ion distributions as our Fig. 4.19 shows. They did not, however, report the electrostatic potential profile which the must have also obtained when solving the Poisson–Boltzmann equation, but rather showed a $V(z)$ measured in the traditional way and not compatible with their ion distributions.

4.1.11 Summary

Summarizing the results for the static properties, we find that monovalent salt does affect the properties of cationic membranes, but that the strength of the effect is strongly dependent on the cationic lipid content. When the bilayer is only mildly cationic, i.e.,

when the DMTAP fraction of lipids is a lot smaller than the DMPC fraction, the salt plays a prominent role in determining the structural, electrostatic and dynamical properties of the bilayer. Infact, in this case the cationic Na^+ ions become one of the most interesting players in the whole bilayer system. Then again, when the bilayer is strongly cationic (the fraction of DMTAPs being equal to or larger than DMPCs) the membrane has a strong positive surface charge, which prevents the Na^+ ions from binding to the carbonyl groups of the DMPCs, and thus the structural, electrostatic as well a dynamic changes imposed by salt on the bilayer are minuscule.

4.2 Simulation results: dynamic

This section focuses on the effects of NaCl on the dynamic properties of DMPC/DMTAP bilayer systems. Although we also look at the lipids that form the cationic membrane, we shall above all focus on its co- (Na^+) and counter- (Cl^-) ions. Their motions can be roughly divided into two parts: those perpendicular to the membrane, and those along it.

We start by looking at the perpendicular motions. In Sec. 4.2.1 we aim to form a qualitative picture of how the Na^+ and Cl^- ions move to and from the charged lipid/water interface and across the water region. Then in Sec. 4.2.2 we shall make our picture more quantitative by actually measuring the residence times of ions within the vicinity of the membrane. Sec. 4.2.3 will discuss the temporal asymmetries between membrane leaflets resulting from the observed long residence times. In Sec. 4.2.4 we then study the other direction: the diffusion of lipids and bound ions along the membrane. Finally, Sec. 4.2.5 sums up our main findings with respect to the dynamic properties.

4.2.1 Ion diffusion perpendicular to membrane

As we know from Sec. 4.1.2, the Na^+ ions were able to bind to the carbonyl oxygens of the zwitterionic DMPC lipids when the membrane had just a mild positive charge. On the other hand, the Cl^- ions were attracted closer and closer to the membrane the stronger its positive charge was (Sec. 4.1.6). In this subsection we study how these attractive regions affected the diffusion of ions in the direction perpendicular to the membrane.

Methods. For each cationic membrane system (Table 3.1), we recorded the z-coordinates of each ion at 10 ps intervals over 50 ns. The origin was fixed to the center of mass of the

bilayer to eliminate the effects of membrane movement. From the periodic images of the ions we chose the one that had $0 < z < L_z$, where L_z was the z-dimension of the simulation box. From these data we constructed a two dimensional histogram, $z(t + \Delta t)$ versus $z(t)$, which visualizes how the position of an ion at time t influences its position at time $t + \Delta t$. Time lapses $\Delta t = 0.1$ ns, 1.0 ns and 10 ns were used; t ranged from 0 ns to $50 - \Delta t$ ns. Bins in the histogram were 0.1 nm $\times$ 0.1 nm and its volume was normalized to unity.

Results. Fig. 4.20 characterizes the ion dynamics perpendicular to the membrane for two different DMTAP molar fractions, $\chi_{\mathrm{TAP}} = 6\%$ (Fig. 4.20a) and 75% (Fig. 4.20b).

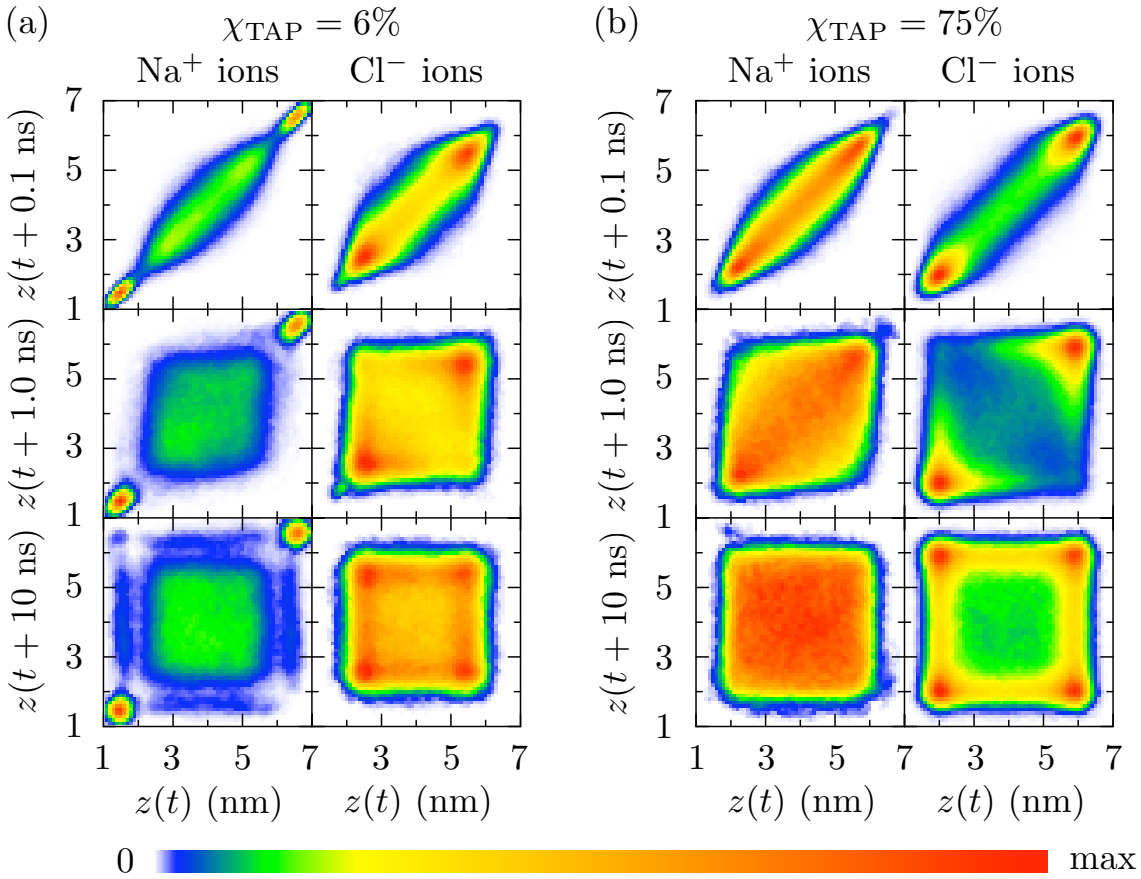

Figure 4.20: Two dimensional histograms visualizing the correlations between ion positions at time t and time $t + \Delta t$. Blue color stands for small correlation, red for high. Mildly cationic ((a), $\chi_{\mathrm{TAP}} = 6\%$) and strongly cationic ((b), 75%) membranes shown; [NaC] = 1.0 M in both.

However, before going into details, let us study two examples to get an intuitive feel on how to read a $z(t + \Delta t)$-versus-$z(t)$ plot. Firstly, if the ions would be completely fixed in the z-direction, we would have $z(t+\Delta t) = z(t)$, and a single straight line of points would cross the plot at a 45° angle. Secondly, if the ions would completely lose the memory of

their position during time Δt, we would have no correlation between $z(t + \Delta t)$ and $z(t)$, and the plot would have a uniform distribution spread across it. Now, what we see in Fig. 4.20 is something in between these two extrema.

The upmost row has $\Delta t = 0.1$ ns. During this reasonably short time the ions do not on average move much along the z-direction. Therefore the plots show a reasonably narrow spread around the $45°$ line. We can, however, already see differences between Na^+ in Cl^- ions and between the mildly charged ($\chi_{\mathrm{TAP}} = 6\%$) and strongly charged (75%) membranes. In particular, at $\chi_{\mathrm{TAP}} = 6\%$ the Na^+ ions were concentrated in the carbonyl regions in the corners of the plot, whereas the other distributions appeared constricted within the water region.

The lowest row has $\Delta t = 10$ ns. During this time the Na^+ ions not bound to the carbonyl region have had time to move anywhere within the water region, and their distribution within this region is uniform. Those Na^+ (in $\chi_{\mathrm{TAP}} = 6\%$), however, that were bound to the carbonyl region, typically stayed bound during the whole 10 ns interval. Thus there are strong peaks in the lower-left and upper-right corners of the plot. The Cl^- ions behaved qualitatively similarly in both the mildly cationic ($\chi_{\mathrm{TAP}} = 6\%$) and the strongly cationic (75%) systems. During the 10 ns time lapse they were able to sample the whole region available to them, but preferred staying close to the membrane, which is evidenced by the four peaks the corners of their distribution. For $\chi_{\mathrm{TAP}} = 75\%$ these peaks were stronger than for $\chi_{\mathrm{TAP}} = 6\%$.

Note that the colors in Fig. 4.20 were scaled separately for each panel to achieve maximum contrast. The 'max' values (top to bottom; left to right) were: (a) 1.01, 0.73, 0.55; 0.39, 0.17, 0.12 and (b) 0.31, 0.12, 0.08; 0.57, 0.33, 0.16. Fig. 4.20 only shows the systems with the highest NaCl salt concentration (1.0 M), but the other concentrations (0.1 M and 0.5 M) appeared qualitatively similar.

Discussion. Separation of time scales between the Na^+ release from the carbonyl region ($\gg 10$ ns) and the ion diffusion across the water region (< 10 ns) was evident (Fig. 4.20). This signals that the binding of ions into the Na^+–DMPC complexes (Sec. 4.1.3) was strong, at least when compared to electrostatic attraction experienced by the Cl^- ions close to the cationic membrane surfaces (Sec. 4.1.6).

The movement of the Na^+ ions not bound in the carbonyl region resembled free diffusion in the sense that they seemed to be indifferent of the positively charged walls (Fig. 4.20). This indicates the effectiveness of the Cl^- counter ion layer (Fig. 4.14) in screening the

cationic bilayer surface to effectively appear as neutral to the inter-membrane bulk water.

As for the Cl^- ions then, the time scale separation between those ions residing in the diffuse counter-ion layer and the ones crossing the bulk water was less striking, although the positively charged surface was able to hold its counter-ions for several nanoseconds (Fig. 4.20, middle row).

4.2.2 Ion Residence Times

In this subsection we perform a quantitative analysis of the ion dynamics described qualitatively in the previous subsection. To do this, we focus on the characteristic "basin of attraction" of each ion type: the lipid carbonyl region (Na^+) and the positive membrane surface (Cl^-), see Figs. 4.20 and 4.13. We determined the residence times of ions within these attractive regions.

Methods. To study the residence times, we used the following definitions (illustrated in Fig. 4.21) for the ion binding. A Na^+ ion was considered to be bound to the lipid carbonyl region once it got closer to the bilayer center than the peak in the Na^+ number density profile and until it moved further away than the peak in the Cl^- number density profile. (For details on determining the number density profiles, see Sec. 4.1.6.) Analogously, a Cl^- ion was considered to be bound once it moved closer to the bilayer center than the peak in the Cl^- number density profile and until it escaped into the bulk water. All the values used in these definitions are given in Table 4.1; if there is no value in Table 4.1, then there was no corresponding residence time to be determined. The reason for using different limits for binding and unbinding was to secure that small fluctuations in an ion's position were not counted as actual binding/unbinding events. In other words, the unbinding limit simply acted as a filter for small fluctuations. We tested varying the unbinding limit, and made sure that our results were robust to the choice of it (data not shown).

The residence times were measured over the whole duration of the measurement period (Fig. 4.2). From these data, residence time histograms were created; the errors were estimated as standard errors of the mean bin height. The results did not qualitatively depend on the choice of keeping or excluding binding events that had started before the measurement started or that continued when it finished (data not shown).

Finally, fits to the histograms were made to study the functional forms of the residence time distributions; the errors were estimated visually.

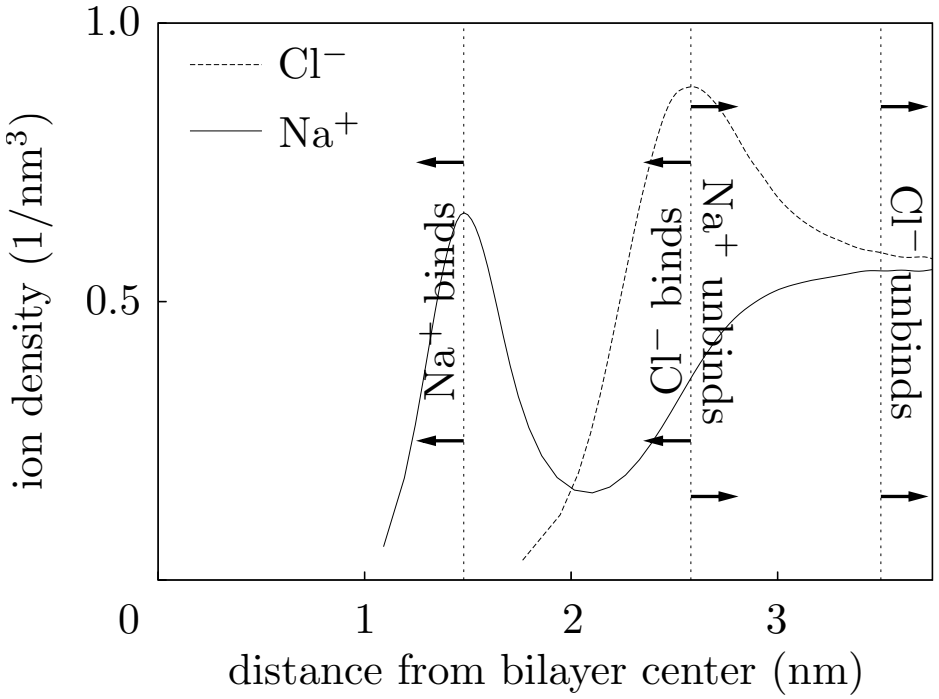

Figure 4.21: Number density profiles (as determined in Sec. 4.1.6) of Na^+ and Cl^- ions, illustrating the definitions used for ion binding. Here $\chi_{\mathrm{TAP}} = 6\%$, [NaCl] = 1.0 M; other systems analogously.

χ_{TAP} (%)	NaCl (M)	Na^+ peak (nm)	Cl^- peak (nm)	Cl^- unbound (nm)
6	0.0	—	2.59	3.5
	0.1	1.335	2.54	3.5
	0.5	1.465	2.53	3.5
	1.0	1.480	2.58	3.5
50	0.0	—	2.16	4.0
	0.1	1.56	2.19	4.0
	0.5	no	2.24	4.0
	1.0	1.62	2.28	4.0
75	0.0	—	1.94	3.75
	0.1	no	1.96	3.75
	0.5	no	2.00	3.75
	1.0	no	2.02	3.75

Table 4.1: The positions of peaks in the Na^+ and Cl^- number density profiles (compare to Fig. 4.13), and the distances from the bilayer center at which the Cl^- ions were considered unbound. These values were used in the calculation of residence times, in accordance with the definition illustrated in Fig. 4.21.

Results. The residence time distributions of Na^+ (in the carbonyl region) and Cl^- (at the positive membrane surface) were strikingly dissimilar (Fig. 4.22).

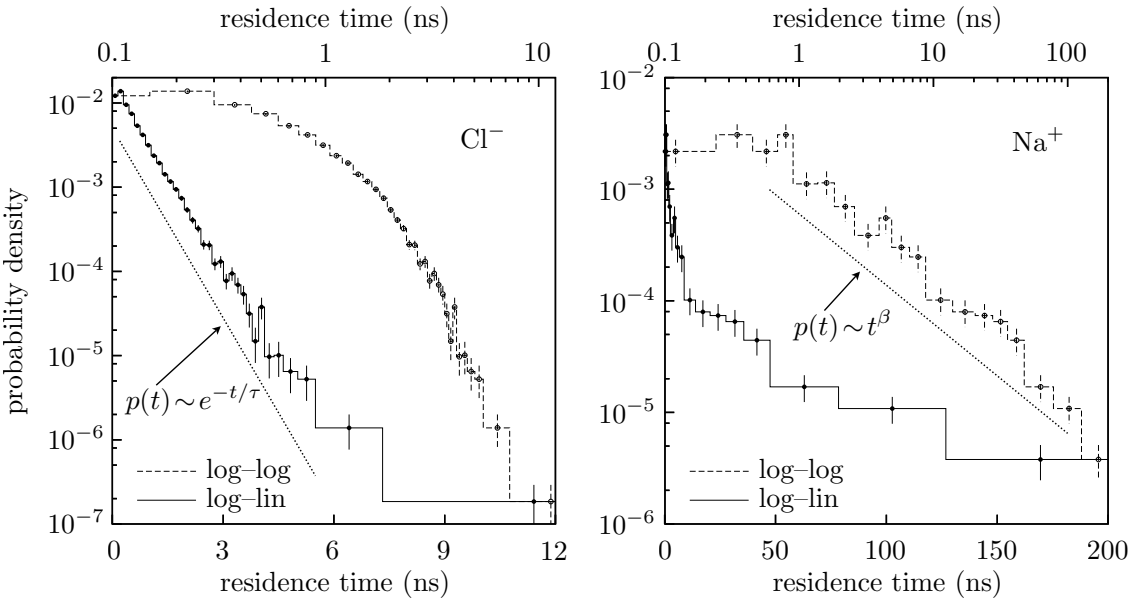

Figure 4.22: The residence time distributions of the counter- (Cl^-, left panel) and co-ions (Na^+, right). Note the logarithmic scale on the y-axis, and that the lower (upper) x-axis has a linear (logarithmic) scale. In each panel, the two curves show the same data plotted on log–log (dashed) and log–lin (solid) scales to reveal the different functional forms.

The Cl^- ion residence times, t, followed an exponential distribution, $\exp(-t/\tau)$, with characteristic decay time, τ. A fit to the linear part of the log–linear plot gave the decay time constant τ as the negative inverse of the slope of the fitted line. Although increase in the surface charge increased τ, it never exceeded a few nanoseconds (Fig. 4.23).

Contrary to Cl^-, sodium appeared to follow a power law, t^{β}, with no characteristic time scale. A fit to the linear part of the log–log plot gave the exponent β. It could only be determined for χ_{TAP} = 50% with [NaCl] = 1.0 M ($\beta = -1.6$), and the χ_{TAP} = 6% systems ($\beta = -0.9$ for 0.1 M, and -1.0 for both 0.5 M and 1.0 M). In other systems there were no, or too few, binding events despite the rather long measurements (Fig. 4.2). The error was estimated to be ± 0.2 in all of the cases. At very short times ($t < 1$ ns) there was a clear deviation from power-law behavior (Fig. 4.22). From our data it was not possible to conclusively define the functional form of the Na^+ residence time distribution. It was, however, without a doubt that the distribution decayed very slowly.

Let us then return to the Cl^- counter ion residence times at the positive membrane surface. Fig. 4.23 shows the characteristic decay times τ as a function of NaCl salt concentration for each of our three cationic membranes, χ_{TAP} = 6%, 50%, and 75%. There was, again, a

qualitative difference between the mildly charged (6%) and the strongly charged (50% and 75%) bilayers. In the strongly charged bilayers the Cl^- characteristic times decayed when the NaCl concentration increased; in the mildly charged bilayer the trend was opposite.

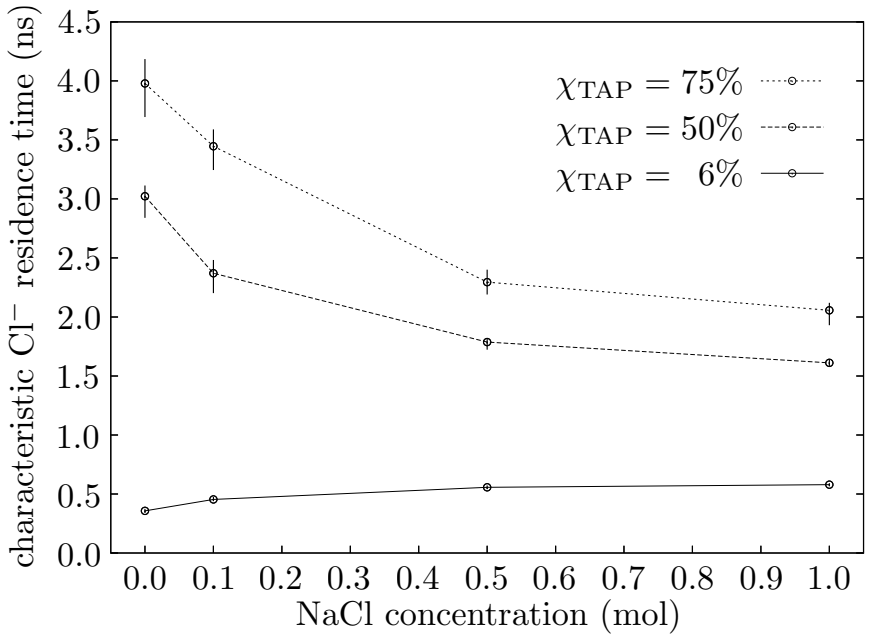

Figure 4.23: The characteristic residence times, τ, of the Cl^- counter ions at the positive membrane surface shown as a function NaCl salt concentration.

Discussion. The Cl^- counter ions were found to have exponentially distributed residence times at the positive membrane surface (Fig. 4.22). The characteristic times were in the nanosecond region (Fig. 4.23). The Na^+ ions in the carbonyl region, in contrast, appeared to have residence time distributions with no characteristic time scale (Fig. 4.22). That is, their distribution had a power law -like appearance at time scales accessible to this study. This explains the long residence times (strongly localized peaks) that appeared in Fig. 4.20a. To the best of our knowledge we are the first to report a detailed study of ion residence times in the vicinity of charged membranes.

The exponentially distributed residence times of Cl^- ions (Fig. 4.22) can be understood simply in terms of a Poisson process (c.f. radioactive decay). This points to the direction that binding of a Cl^- ion to the wall (membrane) is effectively independent of the other Cl^- ions. The behaviour of the Cl^- residence times may thus be qualitatively extrapolated from the simple electrostatic model described in Sec. 2.5. Indeed, Fig. 4.23 shows that (in terms of the Poisson–Boltzmann theory) the surface charge and the salt concentration had expected effects on the characteristic residence times τ:

(1) higher bilayer surface charge σ (that is, higher χ_{TAP}, or in the case of $\chi_{\mathrm{TAP}} = 6\%$ higher [NaCl], see Fig. 4.15), and thus shorter Gouy-Chapman length b, lead to an attraction of counter ions closer to the surface (Fig. 4.13). This tighter binding of ions was reflected as longer characteristic residence times τ in Fig. 4.23.

(2) Higher NaCl salt concentration meant shorter Debye-Hückel screening length λ_{D}, and thus an increase of the ratio b/λ_{D}, allowing the ion cloud to extend further from the bilayer surface. This looser binding is reflected as shorter residence times τ at the $\chi_{\mathrm{TAP}} = 50\%$ and 75% membranes in Fig. 4.23.

(3) At $\chi_{\mathrm{TAP}} = 6\%$, the slightly increasing trend in τ with [NaCl] resulted, because the increase in the positive surface charge σ (Fig. 4.15) decreased b more than the screening effect of the salt decreased λ_{D}.

The long time power law -like distribution for Na^+ ions, on the other hand, is quite intriguing and no simple explanation is available. Comparison with experiments or other simulations is not possible as these properties, as far as we know, have not been studied quantitatively. Sachs and coworkers [127] computed the residence times as a function of distance from a zwitterionic phosphatidylcholine bilayer, but their simulations spanned only 5 ns and an exponential distribution of residence times was assumed, not confirmed. They did, however, observe that the behavior of Na^+ and Cl^- ions was different, and that the time scales related to Na^+ were longer.

4.2.3 Salt asymmetry

The exceedingly long residence times of Na^+ ions within the carbonyl region, quantified in the previous subsection, suggest that there might have been long lived fluctuations in the number of ions bound to a leaflet and corresponding long lived asymmetries in the electrostatic fields. These might affect the interpretation of the measurements, were they typically of the same length or longer than the measurement times (Fig. 4.2). In this subsection we will address this concern.

Methods. As described in detail in Sec. 4.2.2, we counted the number of ions in residence within the attractive regions (carbonyl for Na^+; membrane surface for Cl^-; see Figs. 4.20 and 4.23) of each leaflet. This was done for each cationic membrane system over the whole measurement time (Fig. 4.2). These numbers were plotted as a function of time to study how the occupancy of the leaflets evolved during the simulation.

Results. Fig. 4.24 shows the number of co- (Na^+, top panel) and counter (Cl^-, bottom panel) ions bound to each monolayer (red/black curves) of the mildly positive bilayer ($\chi_{TAP} = 6\%$, [NaCl] = 1.0 M) as a function of time. In addition, the total number of ions of each type bound to the bilayer is shown on gray.

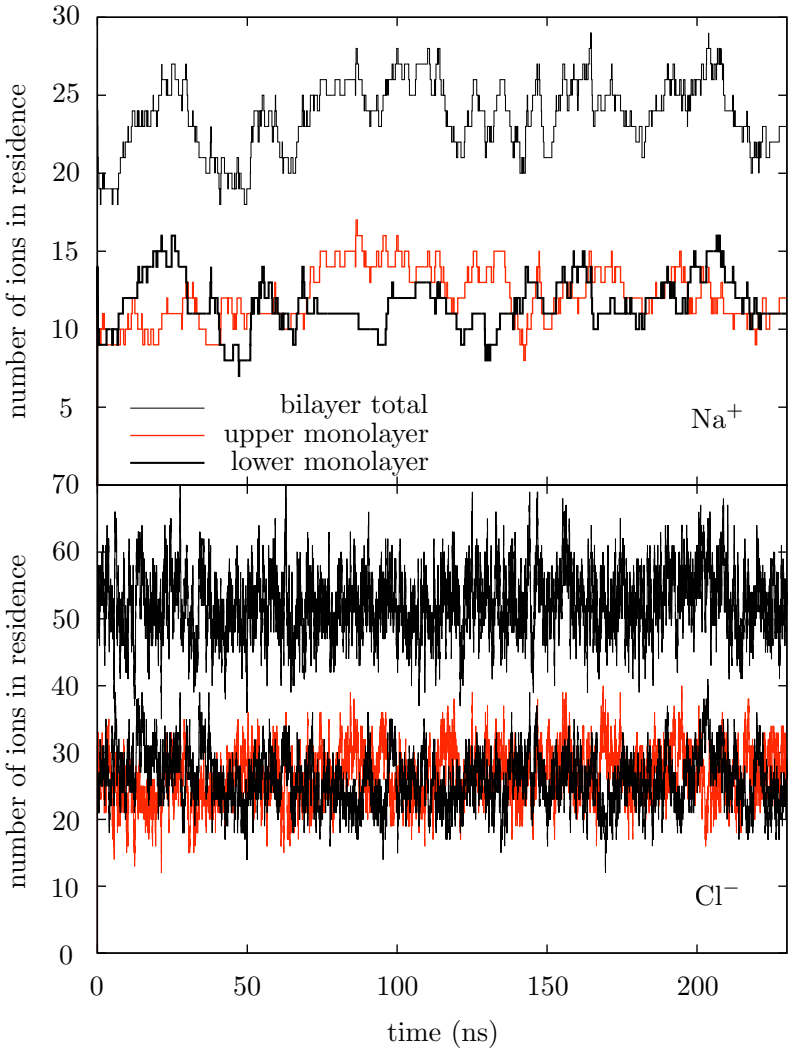

Figure 4.24: Comparison of the number of ions bound to each leaflet (red and black lines) as a function of time. The gray line shows their sum, that is, the total number of ions bound to the bilayer. The upper panel displays Na^+ bound to the carbonyl regions; the lower panel Cl^- bound to the positive membrane surface. For details on determining the bindings, see Sec. 4.2.2. Here $\chi_{TAP} = 6\%$ and [NaCl] = 1.0 M; behavior at other salt concentrations was similar (data not shown).

Long-lived asymmetries in ion content developed between the leaflets. The fluctuations in the number of bound Na^+ ions were slow, taking place in tens of nanoseconds. Although fluctuating more vigorously, the number of attracted Cl^- ions per leaflet followed that of bound Na^+. At maximum the differences between the leaflets were roughly five Na^+ ions and more than 20 Cl^- ions.

Discussion. The rather large and long-lived asymmetries between the membrane leaflets (Fig. 4.24) developed because of the prolonged binding of Na^+ ions to the carbonyl regions (Sec. 4.2.2). These asymmetries were not, however, long-lived or strong enough to cause pore formation, reported for asymmetric bilayer systems [113].

The asymmetries in the number of Cl^- ions per leaflet were naturally following those of Na^+. The amount of Na^+ bound to the carbonyl region namely changed the surface charge of the leaflet (Fig. 4.15), which then attracted the corresponding amount of Cl^- counter ions to compensate it.

Because the binding of ions is a dynamic phenomenon, it is clear that in a molecular dynamics simulation, as in nature, the instantaneous ion occupations of the leaflets will always differ. However, in equilibrium the average coordination numbers must equal. Therefore, measuring the salt asymmetry in a molecular simulation provides—in addition to clarifying the overall physical picture of the system via revealing the time scales involved in the fluctuations of each ion type—a way to investigate the equilibration of the simulation as well as to ensure that the measurement period is long enough to obtain meaningful averages. As the fluctuations in the ion occupancies appeared to take place within tens of nanoseconds (Fig. 4.24), our measurement times (Fig. 4.2) were long enough in this respect.

4.2.4 Lateral diffusion along membrane surface

Until now we have focused on the motion of ions along the membrane normal direction. In this subsection we shall turn our attention to the movements of ions and lipids along the membrane surface. The lateral diffusion of Na^+ ions bound within the carbonyl region will be studied, together with the lateral diffusion of lipid molecules that form the membrane.

The lateral diffusion of lipids can be addressed also experimentally. Typically it is discussed in terms of the lateral diffusion coefficient D, defined as

$$D = \lim_{t\to\infty} \frac{1}{4t} \left\langle r^2(t) \right\rangle .$$

Here $\langle r^2(t) \rangle$ is the mean squared displacement (MSD), the square of the lateral displacement r of a tracer lipid during a time period t, averaged over all the periods of length t during the whole measurement time and over all the lipids that were tracked in the

measurement. As D can be accessed via simulations as well as experimentally, it is an important quantity for characterizing a bilayer system. In this subsection we will study how changes in NaCl salt concentration affect D, and discuss the details of the diffusion mechanisms using the MSD.

Methods. We measured the lateral (2D) diffusion coefficient D_α for each lipid species α,

$$D_\alpha = \lim_{t\to\infty} \frac{1}{4t} \left\langle r^2(t) \right\rangle = \lim_{t\to\infty} \frac{1}{4tN_\alpha} \sum_{i=1}^{N_\alpha} \left\langle r_i^2(t) \right\rangle . \tag{4.10}$$

Here N_α was the total number of lipids of type α (DMPC or DMTAP) in the system (see Table 3.1); $\langle r_i^2(t)\rangle$ was the average (over the sampling time, see Fig. 4.2) squared lateral displacement of the i^{th} lipid (of type α) in time t. To exclude any artificial contributions from leaflet movement, we measured the displacements of the lipid centers of mass, r_i, with respect to the centers of mass of their respective membrane leaflets. The slope of the MSD, $\sum_{i=1}^{N_\alpha} \langle r_i^2(t)\rangle / N_\alpha$, at the limit of the longest available time scale (fitting started from 10 and ended to 25 ns), then provided D_α. The error estimates for the MSD (as standard error of the mean) were evaluated from the variation of $\langle r_i^2(t)\rangle$ of the N_α independent measurements; this allowed estimating the error of MSD at each t. The error estimates for D_α were then visually evaluated from the linear fitting within the MSD error bars.

Similarly as for the lipids, we measured the MSDs, $\sum_{i=1}^{N_\alpha} \langle r_i^2(t)\rangle / N_\alpha$, for the Na^+ ions bound within the carbonyl regions of the membrane. In this case N_α was the total number of binding–unbinding events that took place during the sampling time (Fig. 4.2, see Sec. 4.2.2 for the definition used to determine binding). The displacements r_i were measured with respect to the center of mass of the leaflet at which the i^{th} binding took place.

Finally, to better understand the details of the lateral diffusion mechanism, we measured separately the MSDs of DMPCs and Na^+ ions belonging into complexes of different sizes (see Sec. 4.1.3 for the complex size distributions). As Na^+ and DMPC complexed via the carbonyl oxygen 2Ocarb (Fig. 4.5), we used the Na^+–2Ocarb distance (< 0.28 nm) to identify complexes of 1, 2, 3 or 4 DMPCs, uncomplexed DMPC, and uncomplexed but bound Na^+. Within each of these six groups, the lateral MSDs were measured using Eq. (4.10), regarding each existence of a complex as giving an independent $\langle r_i^2(t)\rangle$. A given complex was considered to exist as long as it comprised exactly those molecules that originally formed it. As the complex half-lives exceeded nanoseconds, the possibility of a complex breaking and reforming between consecutive saved simulation frames (10 ps) did not impact the results.

As a side product of the last analysis, the distributions of bound Na^+ ions among complexes of different sizes were obtained. This was done by counting how many times each complex size realized during the simulation, and normalizing by the their total number.

Results. Fig. 4.25 shows the lateral diffusion coefficients D of the DMPC and DMTAP lipids in the cationic membrane systems. Three qualitative trends emerged:

(1) in all conditions DMPC and DMTAP diffused rather similarly, the difference between them falling within the error bars.

(2) Increase in DMTAP mole fraction χ_{TAP} quickened diffusion slightly in the mixed bilayers (for pure DMPC $D = 1.29 \pm 0.15 \times 10^{-7}$ cm^2/s).

(3) NaCl concentration did not have a noticeable effect on the lipid diffusion, except for the slight slowdown at χ_{TAP}=6%.

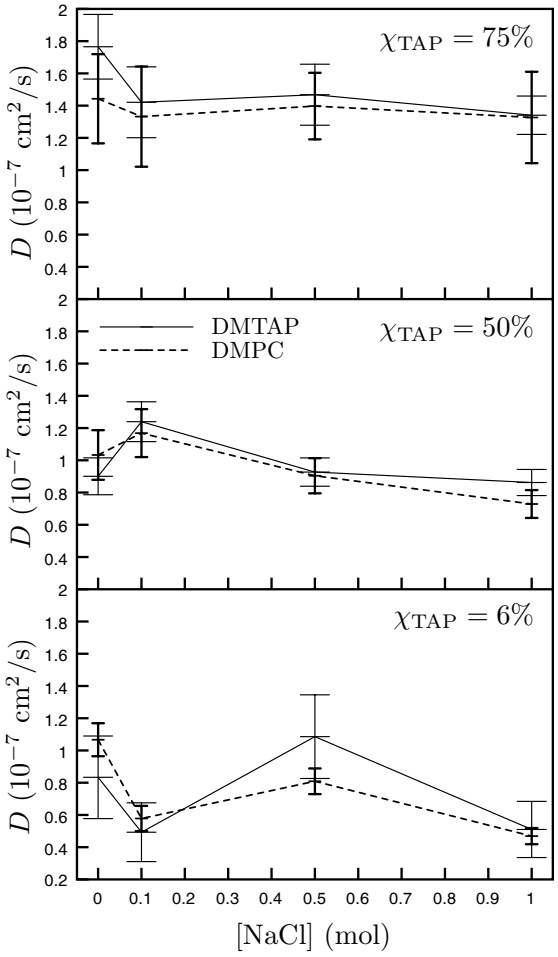

Figure 4.25: The lateral diffusion coefficients D of DMTAP (solid) and DMPC (dashed) lipids as a function of NaCl salt concentration. The panels show our three different DMTAP mole fractions: 75% (top), 50% (middle), and 6% (bottom).

Fig. 4.26 then compares the mean squared displacements of the (DMPC and DMTAP) lipids and the bound Na^+ ions in the mildly cationic ($\chi_{TAP} = 6\%$) membranes. At all NaCl concentrations all the three MSDs appeared to more or less overlap, signaling that there was no major differences in the lateral diffusion rates. In the system having the smallest NaCl concentration (0.1 M) it appeared, however, as if the bound Na^+ ions would be diffusing on average slightly slower than either lipid species. In this system the bound Na^+ ions also stayed mostly (73%) in the big (3- or 4-DMPC) complexes. In the systems with higher NaCl concentration these big complexes were considerably less popular (in 0.5 M: 42%, and in 1.0 M: 48%).

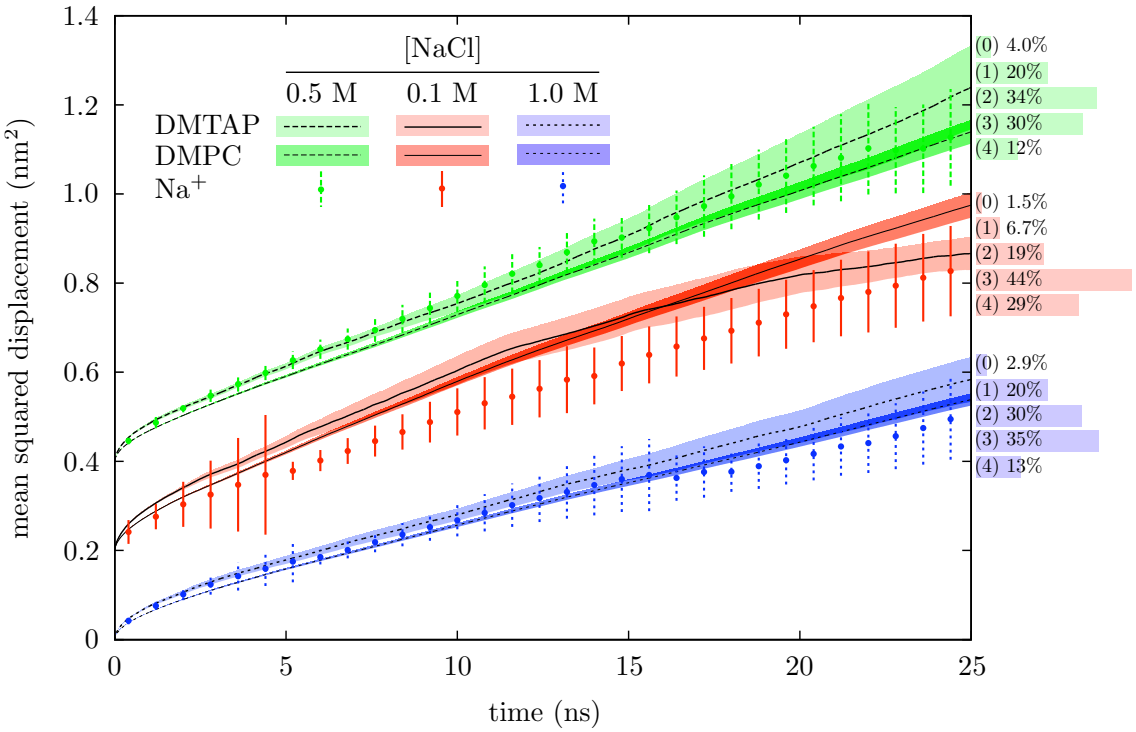

Figure 4.26: The lateral mean squared displacements, MSD(t), for the mildly charged membrane, $\chi_{TAP} = 6\%$, at NaCl salt concentrations of 0.1 M (red), 0.5 M (green), 1.0 M (blue). The MSDs of each lipid type (lines, error bars as color shaded regions) and of Na^+ ions bound in the carbonyl region (dots, vertical error bars; see Sec. 4.2.2 for the definition of binding) are compared. Note that the red (0.1 M) MSDs have been lifted by 0.2 nm^2 and the green (0.5 M) by 0.4 nm^2 to make the plot read better. The corresponding histograms on the right show the average fraction of bound Na^+ ions that are uncomplexed (0) or that are in a complex with (1 to 4) DMPC lipids.

In Fig. 4.27 we take one (1.0 M) of the systems of Fig. 4.26 under closer study to reveal the details of the lateral diffusion mechanism. Whereas Fig. 4.26 showed the MSDs on a time scale spanning tens of nanoseconds, Fig. 4.27 focuses on the time scale of a few nanoseconds and even zooms into the subnanosecond regime. Furthermore, instead of

looking at the MSDs of all the bound Na^+ ions or all the DMPCs as one group, Fig. 4.27 shows the MSDs separated according to the complex size.

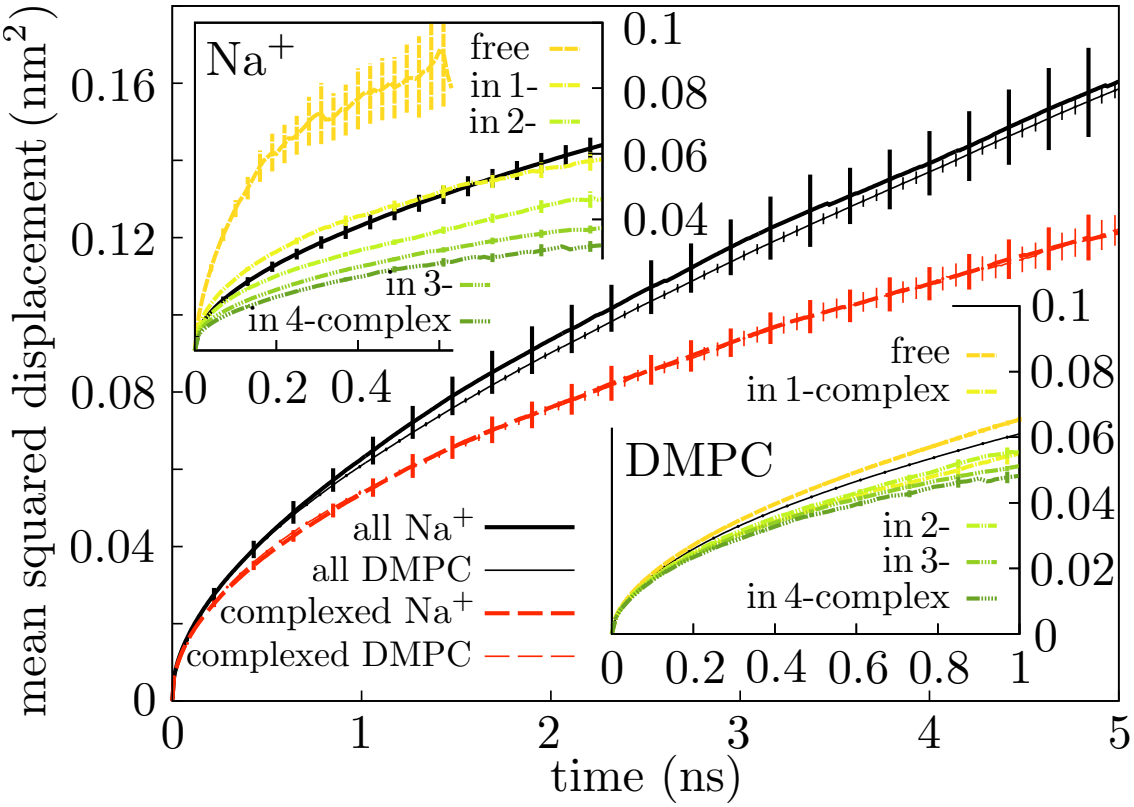

Figure 4.27: Comparison of the lateral mean squared displacements, MSD(t). The black curves show the full data (1.0 M, i.e., the same as in blue in Fig. 4.26). The red curves show the MSDs measured only of those Na^+ and DMPC that belonged to some complex. The insets show the subnanosecond MSDs for Na^+ (upper) and DMPC (lower) separated according to complex size.

The main plot in Fig. 4.27 compares the average MSDs of all Na^+ and all DMPC (black) to the average MSDs when they were part of a complex (red). After joining a complex the diffusion of the ions (thick lines), and equally the lipids (thin lines), was slowed down considerably.

The insets in Fig. 4.27 then show the MSDs for the bound Na^+ ions (upper) and for the DMPCs (lower) separated according to the complex size.

We found the Na^+ lateral diffusion to comprise two qualitatively different modes: free of DMPCs a Na^+ moved very rapidly, but very slowly once complexed.

The time scales for staying in these two modes differed also markedly. The half-time, i.e., the time it took for an uncomplexed ion (or an ion in a complex) to bind to a complex (or

to become uncomplexed) with a 50% probability, was for an uncomplexed Na^+ approximately 300 ps irrespective of [NaCl]. For a complexed Na^+, however, it was an order of magnitude longer: 20 ns (0.1 M), 9 ns (0.5 M), 12 ns (1.0 M).

It appeared, therefore, that the lateral diffusion of Na^+ took place in a 'hopping' fashion. The hops from one DMPC to another occurred rapidly, on a sub-nanosecond time scale, and were fast considering the distance covered, thus making an important contribution to the Na^+ diffusion along the membrane.

The inset for Na^+ in Fig. 4.27 further shows that the bigger the complex, the slower the Na^+ ions became. The inset for DMPC on the other hand reveals that just binding a Na^+ ion, and not even complexing with other DMPCs via it, sufficed to make the short-time DMPC diffusion clearly slower.

Discussion. Changes in NaCl concentration had a surprisingly small effect on the lipid lateral diffusion coefficients D (Fig. 4.25). The slight drop in D seen in the mildly cationic membrane, $\chi_{\mathrm{TAP}} = 6\%$, with increasing [NaCl] was, in the light of Fig. 4.27, associated with the Na^+–DMPC clustering taking place in this system. A change of roughly similar relative magnitude has been reported upon adding NaCl to a POPC bilayer [64]. Clustering has also been observed to be of importance in anionic bilayers [132].

The increase of D caused by increasing DMTAP molar fraction χ_{TAP} in the cationic bilayers (Fig. 4.25) appears closely linked to the free volume per lipid. For salt-free systems, it is known that adding some DMTAP to a DMPC bilayer decreases the area per lipid [45], as the cationic lipids 'stitch' the DMPCs together [46]. After a limiting value (χ_{TAP}=50%), however, the average free volume again increases [45]. This happens because in DMTAP the head group is smaller than in DMPC, and because the electrostatic repulsion between positive headgroups again increases the area per lipid (also we saw this nonmonotonic behavior in Fig. 4.3). As one expects more free volume to lead to faster lipid diffusion, these findings agree with our results in Fig. 4.25.

Typical lateral diffusion coefficients D measured for lipids (for DMPC see e.g. Filippov *et al.* [145]) in biomembranes are of the order of 10^{-8} to 10^{-7} cm^2/s, corresponding to net distances from a few Ångströms to a few nanometers traversed in 100 ns [146]. Lipid diffusion may also involve complex collective motions [147]. It is thus not surprising that accurately finding D using molecular simulations can be challenging, as manifested by Figs. 4.25 and 4.26. Small amount of molecules lead to poor statistics, which was particularly obvious for DMTAPs at $\chi_{\mathrm{TAP}} = 6\%$. Additional trouble was caused by the

rather long times (> 10 ns) required for the lipids to leave behind their initial subdiffusive regime [148] and the lipid mean squared displacements to become linear in time, as required by Eq. (4.10).

Estimating the long-time lateral diffusion coefficients for Na^+ from Fig. 4.26 gives D_{Na^+} of the same order as for the lipids (Fig. 4.25), i.e., $D \approx 0.7 \times 10^{-7}$ cm^2/s, which agrees with the experimental results of Rigaud and coworkers [149], reporting $D_{\mathrm{Na}^+} \approx 0.7 \times 10^{-7}$ cm^2/s at the limit of low water content, i.e., when practically all their Na^+ ions were bound to the membrane.

The lateral diffusion of bound Na^+ ions within the carbonyl region was found to be slower at low (0.1 M) than at high (0.5 M and 1.0 M) NaCl salt concentration (Fig. 4.26). The reason for this was that at [NaCl] = 0.1 M the majority of the bound Na^+ ions were taking part in the large 3- or 4-DMPC complexes, and in bigger complexes the Na^+ ions were slower (Fig. 4.27).

We are not aware of other studies reporting the lateral hopping motion of the bound Na^+ ions described in Fig. 4.27, although there are experimental indications that Na^+ ions could be moving laterally along the membrane surface [125]. The Na^+ hopping could possibly be to some extent related to the diffusional behavior and transport of protons close to and along bilayer surfaces [150].

An interesting subject for further study would be to elucidate the mechanism behind the somewhat unexpected observation that just binding a Na^+ slows a DMPC considerably (inset in Fig. 4.27). This could result from, e.g., an increase in the relaxation time of the carbonyl vector due to the extra positive charge, or an attraction of the bound Na^+ by the carbonyl oxygens of other DMPCs.

4.2.5 Summary

Let us end by summarizing our results for the dynamic properties. Despite the Na^+–DMPC complexes that form in the mildly cationic (χ_{TAP}= 6%) membrane (Sec. 4.1.3) the effect of NaCl salt concentration on the lipid diffusion was rather minute in all our cationic membranes.

The dynamics of Cl^- and Na^+ ions, however, proved more interesting. Their behaviors at the membrane/water interface differed qualitatively: Cl^- ions had well-defined char-

acteristic (nanosecond-scale) residence times, whereas Na^+ ions appeared to lack such, and their residence time distributions were power-law like. The origin of the surprising Na^+ ion residence dynamics remains unclear. The lateral diffusion of Na^+ ions within the water–membrane interface comprised two qualitatively different modes: very slow diffusion when bound to DMPC, punctuated by fast rapid jumps when detached. Overall, the rich dynamics of Na^+ should be interesting for the physics of the whole membrane, especially considering its interaction dynamics with charged macromolecular surfaces.

The dynamics of ions within a lipid bilayer system has been mostly overlooked in the literature until very recently. In simulations typically only the times required for ions to bind on a membrane have been determined for equilibration purposes [64, 112]. In addition to this the computational publications that discuss ion dynamics are extremely few [113, 114, 127]. This is understandable as simulations have to be very long, even with current computational resources.On the other hand, given the importance of ion dynamics in the vicinity of membranes in many biological phenomena, starting from action potentials in nerve cells [151, 152] and ranging from cell energetics [153] to ion-mediated signaling between active membrane proteins [154–156], the subject should really attract more attention. To our knowledge ours is the first systematic report on ion dynamics in charged bilayer systems.

As we have seen, the systems having a low cationic lipid content were able to retain cationic ions in their carbonyl regions for very long times, whereas systems with higher cationic lipid content lacked this ability. This encourages one to speculate on the possibility of signaling via changes in the cationic lipid content, leading to a rapid release of cationic ions from the bilayer. More generally, should membranes' capability of retaining positive ions have biological relevance, one is lead to speculate if this could be part of the explanation for the observed scarcity of cationic lipids in biological membranes.

Chapter 5

Conclusions

The molecular dynamics simulation studies presented in this thesis show how symmetric monovalent (NaCl) salt affects the structural, electrostatic and dynamic properties of a mixed cationic/zwitterionic (DMTAP/DMPC) lipid membrane, and how its effects depend on the lipid composition.

The study was motivated as a step towards understanding the the features of cationic bilayers under physiological conditions. The physiological buffer has high concentrations of various ions and their interactions with the membrane can play a considerable role in its ability to interact with negatively charged biologically relevant objects such as DNA or the cell membrane. This, in turn, has biomedical importance as the cationic lipid systems are used to deliver genetic material and drugs into cells.

The main result of the whole study was that the effects of the NaCl salt were very strongly dependent on the cationic lipid content of the bilayer. At low cationic DMTAP lipid content the salt had a notable effect of the structural properties of the bilayer, decreasing the area per lipid, increasing the tail order, reorienting the DMPC head groups, and increasing the average electrostatic potential difference over the head group region. At high DMTAP content there was hardly any effect when NaCl was added.

The reason for this dichotomy was found to be the ability of the positive Na^+ ions to bind with the DMPC lipid carbonyl oxygens at low DMTAP content and to tie 2 to 4 DMPCs into a dynamic complex. At high DMTAP content the binding of Na^+ was prevented by the high positive surface charge of the bilayer.

The interaction dynamics of the Cl^- and Na^+ ions with the bilayer were found to be

interesting. In particular the lateral diffusion of Na^+ ions within the carbonyl region was intriguing, having two qualitatively different modes. When bound to a DMPC carbonyl oxygen a Na^+ ion was moving very slowly with the lipid. The free Na^+ ions within the carbonyl region, however, were diffusing very fast. The combined effect of the two motions appeared as Na^+ ions hopping from a DMPC carbonyl to another.

With regards to ideas for further studies, it would be extremely interesting to have the results concerning the ion dynamics repeated with other force fields, in particular those using an all-atom description of the lipids. If the results prove robust to the model, other lipids as well as other ion types should be studied simulationally. This should also attract experimental interest to the issue.

Another obvious extension to this work would be to include the interactions with DNA, RNA, or some negatively charged (cell) membrane into the simulations, and changing the cationic DMTAP lipid content and the salt concentration similarly as in the present work. The information thus available should interest also the experimentalists using the cationic lipid vectors in their daily lab routines.

Bibliography

[1] A. A. Gurtovenko, M. Miettinen, M. Karttunen, and I. Vattulainen, "Effect of monovalent salt on cationic lipid membranes as revealed by molecular dynamics simulations," *J. Phys. Chem. B*, vol. 109, pp. 21126–21134, 2005.

[2] M. S. Miettinen, A. A. Gurtovenko, I. Vattulainen, and M. Karttunen, "Ion dynamics in cationic lipid bilayer systems in saline solutions," *J. Phys. Chem. B*, vol. 113, pp. 9226–9234, 2009.

[3] The image has been released into the public domain by its author, who grants anyone to use this work for any purpose, without any conditions, unless such conditions are required by law.

[4] P. Ball, "Water as an active constituent in cell biology," *Chem. Rev.*, vol. 108, pp. 74–108, 2007.

[5] I. Brovchenko and A. Oleinikova, "Which properties of a spanning network of hydration water enable biological functions?," *ChemPhysChem*, vol. 9, pp. 2695–2702, 2008.

[6] F. Paesani and G. A. Voth, "The properties of water: Insights from quantum simulations," *J. Phys. Chem. B*, vol. 113, pp. 5702–5719, 2009.

[7] I. Brovchenko and A. Oleinikova, "Multiple phases of liquid water," *ChemPhysChem*, vol. 9, pp. 2660–2675, 2008.

[8] C. Huang, K. T. Wikfeldt, T. Tokushima, D. Nordlund, Y. Harada, U. Bergmann, M. Niebuhr, T. M. Weiss, Y. Horikawa, M. Leetmaa, M. P. Ljungberg, O. Takahashi, A. Lenz, L. Ojamäe, A. P. Lyubartsev, S. Shin, L. G. M. Pettersson, and A. Nilsson, "The inhomogeneous structure of water at ambient conditions," *P. Natl. Acad. Sci. USA*, vol. 106, pp. 15214–15218, 2009.

[9] "So much more to know," *Science*, vol. 309, pp. 78b–102, 2005.

[10] P. Nelson, *Biological Physics: Energy, Information, Life*. New York, NY: W. H. Freeman and Company, 2004.

[11] P. Ball, "Water — an enduring mystery," *Nature*, vol. 452, pp. 291–292, 2008.

[12] R. Bell, L. Ballas, and R. Coleman, "Lipid topogenesis," *J. Lipid. Res.*, vol. 22, pp. 391–403, 1981.

[13] O. G. Mouritsen, *Life — as a Matter of Fat. The Emerging Science of Lipidomics.* Heidelberg: Springer Verlag, 2005.

[14] G. van Meer, D. R. Voelker, and G. W. Feigenson, "Membrane lipids: where they are and how they behave," *Nat. Rev. Mol. Cell. Biol.*, vol. 9, pp. 112–124, 2008.

[15] H. E. Carter, F. J. Glick, W. P. Norris, and G. E. Phillips, "Biochemistry of the sphingolipides," *J. Biol. Chem.*, vol. 170, pp. 285–294, 1947.

[16] B. F. Cravatt, O. P.-G. G. Siuzdak, N. B. Gilula, S. J. Henriksen, D. L. Boger, and R. A. Lerner, "Chemical characterization of a family of brain lipids that induce sleep," *Science*, vol. 268, pp. 1506–1509, 1995.

[17] M. Sud, E. Fahy, D. Cotter, A. Brown, E. A. Dennis, C. K. Glass, J. Merrill, Alfred H., R. C. Murphy, C. R. H. Raetz, D. W. Russell, and S. Subramaniam, "LMSD: LIPID MAPS structure database," *Nucl. Acids. Res.*, vol. 35, pp. D527–532, 2007.

[18] J. Israelachvili, *Intermolecular & surface forces*. San Diego, CA: Academic Press, 2nd ed., 1991.

[19] M. J. Janiak, D. M. Small, and G. G. Shipley, "Temperature and compositional dependence of the structure of hydrated dimyristoyl lecithin.," *J. Biol. Chem.*, vol. 254, pp. 6068–6078, 1979.

[20] R. Koynova and M. Caffrey, "Phases and phase transitions of the phosphatidylcholines," *Biochim. Biophys. Acta*, vol. 1376, pp. 91–145, 1998.

[21] J. F. Nagle and S. Tristram-Nagle, "Structure of lipid bilayers," *Biochim. Biophys. Acta*, vol. 1469, pp. 159–195, 2000.

[22] Y. F. Hifeda and G. W. Rayfield, "Evidence for first-order phase transitions in lipid and fatty acid monolayers," *Langmuir*, vol. 8, pp. 197–200, 1992.

[23] F. R. Maxfield, "Plasma membrane microdomains," *Curr. Op. Cell Biol.*, vol. 14, pp. 483–487, 2002.

[24] H. M. McConnell and A. Radhakrishnan, "Condensed complexes of cholesterol and phospholipids," *Biochim. Biophys. Acta*, vol. 1610, pp. 159–173, 2003.

[25] R. Faller and S.-J. Marrink, "Simulation of domain formation in DLPC–DSPC mixed bilayers," *Langmuir*, vol. 20, pp. 7686–7693, 2004.

[26] L. A. Bagatolli, "To see or not to see: Lateral organization of biological membranes and fluorescence microscopy," *BBA – Biomembranes*, vol. 1758, pp. 1541–1556, 2006.

[27] R. Langer, "Drug delivery and targeting," *Nature (supp.)*, vol. 392, pp. 5–10, 1998.

[28] D. D. Lasic, "Novel applications of liposomes," *Trends Biotechnol.*, vol. 16, pp. 307–321, 1998.

[29] G. Gregoriadis, C. P. Swain, E. J. Wills, and A. S. Tavill, "Drug-carrier potential of liposomes in cancer chemotherapy," *Lancet*, vol. 303, pp. 1313–1316, 1974.

[30] D. Needham, G. Anyarambhatla, G. Kong, and M. W. Dewhirst, "A new temperature-sensitive liposome for use with mild hyperthermia: Characterization and testing in a human tumor xenograft model," *Cancer Res.*, vol. 60, pp. 1197–1201, 2000.

[31] T. M. Allen, "Liposomal drug delivery," *Curr. Opin. Coll. Interf. Sci.*, vol. 1, pp. 645–651, 1996.

[32] R. Podgornik, D. Harries, J. DeRouchey, H. H. Strey, and V. A. Parsegian, "Interactions in macromolecular complexes used as non-viral vectors for gene delivery," in *Gene and Cell Therapy: Therapeutic Mechanisms and Strategies* (N. S. Templeton, ed.), ch. 7, (preprint), CRC, 3rd ed., 2008.

[33] D. D. Lasic, *Liposomes in gene delivery*. CRC Press, 1997.

[34] D. D. Lasic, H. Strey, M. C. A. Stuart, R. Podgornik, and P. M. Frederik, "The structure of DNA–liposome complexes," *J. Am. Chem. Soc.*, vol. 119, pp. 832–833, 1997.

[35] J. O. Rädler, I. Koltover, T. Salditt, and C. R. Safinya, "Structure of DNA-cationic liposome complexes: DNA intercalation in multilamellar membranes in distinct interhelical packing regimes," *Science*, vol. 275, pp. 810–814, 1997.

[36] B. Pitard, O. Aguerre, M. Airiau, A.-M. Lachagès, T. Boukhnikachvili, G. Byk, C. Dubertret, C. Herviou, D. Scherman, J.-F. Mayaux, and J. Crouzet, "Virus-sized self-assembling lamellar complexes between plasmid DNA and cationic micelles promote gene transfer," *P. Natl. Acad. Sci. USA*, vol. 94, pp. 14412–14417, 1997.

[37] R. Labas, F. Beilvert, B. Barteau, S. David, R. Chèvre, and B. Pitard, "Nature as a source of inspiration for cationic lipid synthesis," *Genetica*, vol. 138, pp. 153–168, 2010.

[38] L. Desigaux, M. Sainlos, O. Lambert, R. Chevre, E. Letrou-Bonneval, J.-P. Vigneron, P. Lehn, J.-M. Lehn, and B. Pitard, "Self-assembled lamellar complexes of siRNA with lipidic aminoglycoside derivatives promote efficient siRNA delivery and interference," *P. Natl. Acad. Sci. USA*, vol. 104, pp. 16534–16539, 2007.

[39] A. Schroeder, C. G. Levins, C. Cortez, R. Langer, and D. G. Anderson, "Lipid-based nanotherapeutics for siRNA delivery," *J. Intern. Med.*, vol. 267, pp. 9–21, 2010.

[40] F. Artzner, R. Zantl, G. Rapp, and J. O. Rädler, "Observation of a rectangular columnar phase in condensed lamellar cationic lipid-DNA complexes," *Phys. Rev. Lett.*, vol. 81, pp. 5015–5018, 1998.

[41] R. Zantl, F. Artzner, G. Rapp, and J. O. Rädler, "Thermotropic structural changes of saturated-cationic-lipid-DNA complexes," *Europhys. Lett.*, vol. 45, pp. 90–96, 1998.

[42] R. Zantl, L. Baicu, F. Artzner, I. Sprenger, G. Rapp, and J. O. Rädler, "Thermotropic phase behavior of cationic lipid-DNA complexes compared to binary lipid mixtures," *J. Phys. Chem. B*, vol. 103, pp. 10300–10310, 1999.

[43] W. Pohle, C. Selle, D. R. Gauger, R. Zantl, F. Artzner, and J. O. Rädler, "FTIR spectroscopic characterization of a cationic lipid DNA complex and its components," *Phys. Chem. Chem. Phys.*, vol. 2, pp. 4642–4650, 2000.

[44] S. Bandyopadhyay, M. Tarek, and M. L. Klein, "Molecular dynamics study of a lipid–DNA complex," *J. Phys. Chem. B*, vol. 103, pp. 10075–10080, 1999.

[45] A. A. Gurtovenko, M. Patra, M. Karttunen, and I. Vattulainen, "Cationic DMPC/DMTAP lipid bilayers: Molecular dynamics study," *Biophys. J.*, vol. 86, pp. 3461–3472, 2004.

[46] L. Zhang, T. A. Spurlin, A. A. Gewirth, and S. Granick, "Electrostatic stitching in gel-phase supported phospholipid bilayers," *J. Phys. Chem. B*, vol. 110, pp. 33–35, 2006.

[47] V. Levadny and M. Yamazaki, "Cationic DMPC/DMTAP lipid bilayers: Local lateral polarization of phosphatidylcholine headgroups," *Langmuir*, vol. 21, pp. 5677–5680, 2005.

[48] G. Cevc, "Membrane electrostatics," *Biochim. Biophys. Acta*, vol. 1031, pp. 311–382, 1990.

[49] D. Andelman, "Introduction to electrostatics in soft and biological matter," in *Proceedings of the Nato ASI & SUSSP on "Soft condensed matter physics in molecular and cell biology"* (W. Poon and D. Andelman, eds.), (New York), pp. 97–122, Taylor & Francis Ltd, 2006.

[50] R. M. Pashley, "Hydration forces between mica surfaces in aqueous electrolyte solutions," *J. Colloid Interf. Sci.*, vol. 80, pp. 153–162, 1981.

[51] R. M. Pashley and J. N. Israelachvili, "Molecular layering of water in thin films between mica surfaces and its relation to hydration forces," *J. Colloid Interf. Sci.*, vol. 101, pp. 511–523, 1984.

[52] G. Luo, S. Malkova, J. Yoon, D. G. Schultz, B. Lin, M. Meron, I. Benjamin, P. Vanysek, and M. L. Schlossman, "Ion distributions near a liquid-liquid interface," *Science*, vol. 311, pp. 216–218, 2006.

[53] J. Marra, "Direct measurement of the interaction between phosphatidylglycerol bilayers in aqueous electrolyte solutions.," *Biophys. J.*, vol. 50, pp. 815–825, 1986.

[54] P. Kekicheff, S. Marcelja, T. J. Senden, and V. E. Shubin, "Charge reversal seen in electrical double layer interaction of surfaces immersed in 2:1 calcium electrolyte," *J. Chem. Phys.*, vol. 99, pp. 6098–6113, 1993.

[55] M. L. Fielden, R. A. Hayes, and J. Ralston, "Oscillatory and ion-correlation forces observed in direct force measurements between silica surfaces in concentrated $CaCl_2$ solutions," *Phys. Chem. Chem. Phys.*, vol. 2, pp. 2623–2628, 2000.

[56] M. Quesada-Perez, E. Gonzalez-Tovar, A. Martin-Molina, M. Lozada-Cassou, and R. Hidalgo-Alvarez, "Ion size correlations and charge reversal in real colloids," *Coll. Surf. A*, vol. 267, pp. 24–30, 2005.

[57] T. E. Angelini, R. Golestanian, R. H. Coridan, J. C. Butler, A. Beraud, M. Krisch, H. Sinn, K. S. Schweizer, and G. C. L. Wong, "Counterions between charged polymers exhibit liquid-like organization and dynamics," *P. Natl. Acad. Sci. USA*, vol. 103, pp. 7962–7967, 2006.

[58] C. Holm, P. Kékicheff, and R. Podgornik, eds., *Electrostatic Effects in Soft Matter and Biophysics*, (Dordrecht), Kluwer Academic Publishers, 2001.

[59] Y. Burak and D. Andelman, "Hydration interactions: Aqueous solvent in electric double layers," *Phys. Rev. E*, vol. 62, pp. 5296–5312, 2000.

[60] A. Y. Grosberg, T. T. Nguyen, and B. I. Shklovskii, "The physics of charge inversion in chemical and biological systems," *Rev. Mod. Phys.*, vol. 74, p. 329, 2002.

[61] R. R. Netz, "Electrostatistics of counter-ions at and between planar charged walls: From Poisson-Boltzmann to the strong-coupling theory," *Eur. Phys. J. E*, vol. 5, pp. 557–574, 2001.

[62] M. Patra, M. Patriarca, and M. Karttunen, "Stability of charge inversion, Thomson problem and application to electrophoresis," *Phys. Rev. E*, vol. 67, p. 031402, 2003.

[63] O. Punkkinen, A. Naji, R. Podgornik, I. Vattulainen, and P.-L. Hansen, "Ionic cloud distribution close to a charged surface in the presence of salt," *Europhys. Lett.*, vol. 82, p. 48001, 2007.

[64] R. A. Böckmann, A. Hac, T. Heimburg, and H. Grubmüller, "Effect of sodium chloride on a lipid bilayer," *Biophys. J.*, vol. 85, pp. 1647–1655, 2003.

[65] D. P. Tieleman and H. J. C. Berendsen, "Molecular dynamics simulations of a fully hydrated dipalmitoylphosphatidylcholine bilayer with different macroscopic boundary conditions and parameters," *J. Chem. Phys.*, vol. 105, pp. 4871–4880, 1996.

[66] A. A. Gurtovenko and I. Vattulainen, "Calculation of the electrostatic potential of lipid bilayers from molecular dynamics simulations: Methodological issues," *J. Chem. Phys.*, vol. 130, pp. 215107–7, 2009.

[67] G. Ciccotti, D. Frenkel, and I. R. McDonald, eds., *Simulation of Liquids and Solids*. New York: North-Holland, 1990.

[68] E. H. Lee, J. Hsin, M. Sotomayor, G. Comellas, and K. Schulten, "Discovery through the computational microscope," *Structure*, vol. 17, pp. 1295–1306, 2009.

[69] D. Frenkel and B. Smit, *Understanding molecular simulation: From algorithms to applications, 2nd edition*. San Diego: Academic Press, 2002.

[70] A. L. Fetter and J. D. Walecka, *Theoretical Mechanics of Particles and Continua*. McGraw–Hill, 1980.

[71] M. E. Tuckerman and G. J. Martyna, "Understanding molecular dynamics: Techniques and applications," *J. Phys. Chem. B*, vol. 104, pp. 159–178, 2000.

[72] H. J. C. Berendsen, *Simulating the Physical World: Hierarchical Modeling from Quantum Mechanics to Fluid Dynamics*. Cambridge, UK: Cambridge University Press, 1st ed., 2007.

[73] T. Schlick, *Molecular Modeling and Simulation: An Interdisciplinary Guide*, vol. 21 of *Interdisciplinary Applied Mathematics*. Springer-Verlag, 2002.

[74] M. P. Allen, "Introduction to molecular dynamics simulation," in *Computational Soft Matter: From Synthetic Polymers to Proteins* (N. Attig, K. Binder, H. Grubmüller, and K. Kremer, eds.), vol. 23 of *NIC Series*, ch. 1, pp. 1–27, Forschungszentrum Jülich, Germany: John von Neumann Institute for Computing, 2004.

[75] J. P. Ryckaert, G.Ciccotti, and H. Berendsen, "Numerical-integration of Cartesian equations of motion of a system with constraints—molecular-dynamics of n-alcanes," *J. Comput. Phys.*, vol. 23, p. 1090, 1977.

[76] B. Hess, H. Bekker, H. J. C. Berendsen, and J. G. E. M. Fraaije, "LINCS: A linear constraint solver for molecular simulations," *J. Comp. Chem.*, vol. 18, pp. 1463–1472, 1997.

[77] S. Miyamoto and P. A. Kollman, "SETTLE: An analytical version of the SHAKE and RATTLE algorithms for rigid water models," *J. Comp. Chem.*, vol. 13, pp. 952–962, 1992.

[78] M. P. Allen and D. J. Tildesley, *Computer Simulation of Liquids*. Oxford: Oxford University Press, 1987.

[79] H. J. C. Berendsen, J. P. M. Postma, W. F. van Gunsteren, A. DiNola, and J. R. Haak, "Molecular dynamics with coupling to an external bath," *J. Chem. Phys.*, vol. 81, pp. 3684–3690, 1984.

[80] T. Morishita, "Fluctuation formulas in molecular-dynamics simulations with the weak coupling heat bath," *J. Chem. Phys.*, vol. 113, pp. 2976–2982, Aug. 2000.

[81] S. Nosé, "A molecular dynamics method for simulations in the canonical ensemble," *Mol. Phys.*, vol. 52, pp. 255–268, 1984.

[82] S. Nosé, "A unified formulation of the constant temperature molecular dynamics methods," *J. Chem. Phys.*, vol. 81, pp. 511–519, 1984.

[83] W. G. Hoover, "Canonical dynamics: Equilibrium phase-space distributions," *Phys. Rev. A*, vol. 31, pp. 1695–1697, 1985.

[84] M. Parrinello and A. Rahman, "Polymorphic transitions in single crystals: A new molecular dynamics method," *J. Appl. Phys.*, vol. 52, pp. 7182–7190, 1981.

[85] S. Nosé and M. L. Klein, "Constant pressure molecular dynamics for molecular systems," *Mol. Phys.*, vol. 50, pp. 1055–1076, 1983.

[86] M. Patra, M. Karttunen, M. T. Hyvönen, P. Lindqvist, E. Falck, and I. Vattulainen, "Molecular dynamics simulations of lipid bilayers: Major artifacts due to truncating electrostatic interaction," *Biophys. J.*, vol. 84, pp. 3636–3645, 2003.

[87] M. Patra, M. Karttunen, M. T. Hyvönen, E. Falck, and I. Vattulainen, "Lipid bilayers driven to a wrong lane in molecular dynamics simulations by truncation of long-range electrostatic interactions," *J. Phys. Chem. B*, vol. 108, pp. 4485–4494, 2004.

[88] P. P. Ewald, "Die Berechnung optischer und elektrostatischer Gitterpotentiale," *Ann. Phys. (Leipzig)*, vol. 369, pp. 253–287, 1921.

[89] M. Deserno and C. Holm, "How to mesh up Ewald sums. II. An accurate error estimate for the particle-particle-particle-mesh routines," *J. Chem. Phys.*, vol. 109, p. 7694, 1998.

[90] J. W. Cooley and J. W. Tukey, "An algorithm for the machine calculation of complex fourier series," *Math. Comput.*, vol. 19, pp. 297–301, 1965.

[91] T. Darden, D. York, and L. Pedersen, "Particle mesh Ewald: An N log(N) method for Ewald sums in large systems," *J. Chem. Phys.*, vol. 98, pp. 10089–10092, 1993.

[92] U. Essman, L. Perela, M. L. Berkowitz, H. L. T. Darden, and L. G. Pedersen, "A smooth particle mesh Ewald method," *J. Chem. Phys.*, vol. 103, pp. 8577–8592, 1995.

[93] T. Róg, K. Murzyn, and M. Pasenkiewicz-Gierula, "Molecular dynamics simulations of charged and neutral lipid bilayers: Treatment of electrostatic interactions," *Acta Biochim. Pol.*, vol. 50, pp. 789–798, 2003.

[94] A. Cordomì, O. Edholm, and J. J. Perez, "Effect of different treatments of long-range interactions and sampling conditions in molecular dynamic simulations of rhodopsin embedded in a dipalmitoyl phosphatidylcholine bilayer," *J. Comp. Chem.*, vol. 28, pp. 1017–1030, 2007.

[95] W. G. Hoover, *Computational Statistical Mechanics*. Elsevier Science Pub Co, 1991.

[96] B. Leimkuhler and S. Reich, *Simulating Hamiltonian Dynamics*, vol. 14 of *Cambridge monographs on applied and computational mathematics*. Cambridge, UK: Cambridge University Press, 1st ed., 2004.

[97] S. Toxvaerd, "Hamiltonians for discrete dynamics," *Phys. Rev. E*, vol. 50, pp. 2271–2274, 1994.

[98] E. Hairer, C. Lubich, and G. Wanner, *Geometric Numerical Integration: Structure-Preserving Algorithms for Ordinary Differential Equations*, vol. 31 of *Springer Series in Computational Mathematics*. Heidelberg, Germany: Springer-Verlag, 1st ed., 2002.

[99] P. Niemelä, *Computational Modelling of Lipid Bilayers with Sphingomyelin and Sterols*. PhD thesis, Helsinki University of Technology, Espoo, Finland, 2007.

[100] O. Berger, O. Edholm, and F. Jahnig, "Molecular dynamics simulations of a fluid bilayer of dipalmitoylphosphatidylcholine at full hydration, constant pressure, and constant temperature," *Biophys. J.*, vol. 72, pp. 2002–2013, 1997.

[101] H. J. C. Berendsen, D. van der Spoel, and R. van Drunen, "GROMACS: A message-passing parallel molecular dynamics implementation," *Comp. Phys. Comm.*, vol. 91, pp. 43–56, 1995.

[102] E. Lindahl, B. Hess, and D. van der Spoel, "GROMACS 3.0: A package for molecular simulation and trajectory analysis," *J. Mol. Model.*, vol. 7, pp. 306–317, 2001.

[103] D. van der Spoel, E. Lindahl, B. Hess, G. Groenhof, A. E. Mark, and H. J. C. Berendsen, "GROMACS: Fast, flexible, and free," *J. Comp. Chem.*, vol. 26, pp. 1701–1718, 2005.

[104] H. J. C. Berendsen, J. P. M. Postma, W. F. van Gunsteren, and J. Hermans, "Interaction models for water in relation to protein hydration," in *Intermolecular Forces* (B. Pullman, ed.), pp. 331–342, Dordrecht: Reidel, 1981.

[105] C. Anézo, A. H. de Vries, H.-D. Höltje, D. P. Tieleman, and S.-J. Marrink, "Methodological issues in lipid bilayer simulations," *J. Phys. Chem. B*, vol. 107, pp. 9424–9433, 2003.

[106] O. Enders, A. Ngezahayo, M. Wiechmann, F. Leisten, and H.-A. Kolb, "Structural calorimetry of main transition of supported DMPC bilayers by temperature-controlled AFM," *Biophys J.*, vol. 87, pp. 2522–2531, 2004.

[107] R. N. A. H. Lewis, S. Tristram-Nagle, J. F. Nagle, and R. N. McElhaney, "The thermotropic phase behavior of cationic lipids: Calorimetric, infrared spectroscopic and X-ray diffraction studies of lipid bilayer membranes composed of 1,2-di-O-myristoyl-3-N,N,N-trimethylaminopropane (DM-TAP)," *BBA - Biomembranes*, vol. 1510, pp. 70–82, 2001.

[108] H. Flyvbjerg and H. G. Petersen, "Error estimates on averages of correlated data," *J. Chem. Phys.*, vol. 91, pp. 461–466, 1989.

[109] S. A. Pandit, D. Bostick, and M. L. Berkowitz, "Molecular dynamics simulation of a dipalmitoylphosphatidylcholine bilayer with NaCl," *Biophys. J.*, vol. 84, pp. 3743–3750, 2003.

[110] A. A. Gurtovenko, "Asymmetry of lipid bilayers induced by monovalent salt: Atomistic molecular-dynamics study," *J. Chem. Phys.*, vol. 122, p. 244902, 2005.

[111] A. Cordomi, O. Edholm, and J. J. Perez, "Effect of ions on a dipalmitoyl phosphatidylcholine bilayer. A molecular dynamics simulation study," *J. Phys. Chem. B*, vol. 112, pp. 1397–1408, 2008.

[112] R. A. Böckmann and H. Grubmüller, "Multistep binding of divalent cations to phospholipid bilayers: A molecular dynamics study," *Angew. Chem. Int. Edn.*, vol. 43, pp. 1021–1024, 2004.

[113] A. A. Gurtovenko and I. Vattulainen, "Pore formation coupled to ion transport through lipid membranes as induced by transmembrane ionic charge imbalance: Atomistic molecular dynamics study," *J. Am. Chem. Soc.*, vol. 127, pp. 17570–17571, 2005.

[114] A. A. Gurtovenko and I. Vattulainen, "Ion leakage through transient water pores in protein-free lipid membranes driven by transmembrane ionic charge imbalance," *Biophys. J.*, vol. 92, pp. 1878–1890, 2007.

[115] S.-J. Lee, Y. Song, and N. A. Baker, "Molecular dynamics simulations of asymmetric NaCl and KCl solutions separated by phosphatidylcholine bilayers: potential drops and structural changes induced by strong Na^+-lipid interactions and finite size effects," *Biophys. J.*, vol. 94, pp. 3565–3576, 2008.

[116] A. A. Gurtovenko and I. Vattulainen, "Effect of NaCl and KCl on phosphatidylcholine and phosphatidylethanolamine lipid membranes: Insight from atomic-scale simulations for understanding salt-induced effects in the plasma membrane," *J. Phys. Chem. B*, vol. 112, pp. 1953–1962, 2008.

[117] K. Collins, "Sticky ions in biological systems," *P. Natl. Acad. Sci. USA*, vol. 92, pp. 5553–5557, 1995.

[118] K. D. Collins, "Charge density-dependent strength of hydration and biological structure.," *Biophys. J.*, vol. 72, pp. 65–76, 1997.

[119] H. Hauser, M. C. Phillips, B. A. Levine, and R. J. P. Williams, "Conformation of the lecithin polar group in charged vesicles," *Nature*, vol. 261, pp. 390–394, 1976.

[120] S. A. Tatulian, "Binding of alkaline-earth metal cations and some anions to phosphatidylcholine liposomes," *Eur. J. Biochem.*, vol. 170, pp. 413–420, 1987.

[121] H. Binder and O. Zschornig, "The effect of metal cations on the phase behavior and hydration characteristics of phospholipid membranes," *Chem. Phys. Lipids*, vol. 115, pp. 39–61, 2002.

[122] S. Garcia-Manyes, G. Oncins, and F. Sanz, "Effect of ion-binding and chemical phospholipid structure on the nanomechanics of lipid bilayers studied by force spectroscopy," *Biophys. J.*, vol. 89, pp. 1812–1826, 2005.

[123] S. Garcia-Manyes, G. Oncins, and F. Sanz, "Effect of pH and ionic strength on phospholipid nanomechanics and on deposition process onto hydrophilic surfaces measured by AFM," *Electrochim. Acta*, vol. 51, pp. 5029–5036, 2006.

[124] G. Pabst, A. Hodzic, J. Strancar, S. Danner, M. Rappolt, and P. Laggner, "Rigidification of Neutral Lipid Bilayers in the Presence of Salts," *Biophys. J.*, vol. 93, pp. 2688–2696, 2007.

[125] T. Fukuma, M. J. Higgins, and S. P. Jarvis, "Direct imaging of lipid-ion network formation under physiological conditions by frequency modulation atomic force microscopy," *Phys. Rev. Lett.*, vol. 98, p. 106101, 2007.

[126] J. N. Sachs and T. B. Woolf, "Understanding the Hofmeister effect in interactions between chaotropic anions and lipid bilayers: Molecular dynamics simulations," *J. Am. Chem. Soc.*, vol. 125, pp. 8742–8743, 2003.

[127] J. N. Sachs, H. Nanda, H. I. Petrache, and T. B. Woolf, "Changes in phosphatidylcholine headgroup tilt and water order induced by monovalent salts: Molecular dynamics simulations," *Biophys. J.*, vol. 86, pp. 3772–3782, 2004.

[128] U. R. Pedersen, C. Leidy, P. Westh, and G. H. Peters, "The effect of calcium on the properties of charged phospholipid bilayers," *BBA – Biomembranes*, vol. 1758, pp. 573–582, 2006.

[129] E. Lindahl and O. Edholm, "Mesoscopic undulations and thickness fluctuations in lipid bilayers from molecular dynamics simulations," *Biophys. J.*, vol. 79, pp. 426–433, 2000.

[130] S. A. Pandit, D. Bostick, and M. L. Berkowitz, "Mixed bilayer containing dipalmitoylphosphatidylcholine and dipalmitoylphosphatidylserine: Lipid complexation, ion binding, and electrostatics," *Biophys J.*, vol. 85, pp. 3120–3131, 2003.

[131] P. Mukhopadhyay, L. Monticelli, and D. P. Tieleman, "Molecular dynamics simulation of a palmitoyl-oleoyl phosphatidylserine bilayer with Na^+ counterions and NaCl," *Biophys. J.*, vol. 86, pp. 1601–1609, 2004.

[132] W. Zhao, T. Rog, A. A. Gurtovenko, I. Vattulainen, and M. Karttunen, "Atomic-Scale Structure and Electrostatics of Anionic Palmitoyloleoylphosphatidylglycerol Lipid Bilayers with Na^+ Counterions," *Biophys. J.*, vol. 92, pp. 1114–1124, 2007.

[133] K. Shinoda, W. Shinoda, and M. Mikami, "Molecular dynamics simulation of an archaeal lipid bilayer with sodium chloride," *Phys. Chem. Chem. Phys.*, vol. 9, pp. 643–650, 2007.

[134] M. Patra and M. Karttunen, "Systematic comparison of force fields for microscopic simulations of NaCl in aqueous solutions: Diffusion, free energy of hydration and structural properties," *J. Comp. Chem.*, vol. 25, pp. 678–689, 2004.

[135] A. A. Gurtovenko and I. Vattulainen, "Lipid transmembrane asymmetry and intrinsic membrane potential: Two sides of the same coin," *J. Am. Chem. Soc.*, vol. 129, pp. 5358–5359, 2007.

[136] J. Seelig, P. M. Macdonald, and P. G. Scherer, "Phospholipid head groups as sensors of electric charge in membranes," *Biochemistry*, vol. 26, pp. 7535–7541, 1987.

[137] S. W. Chiu, M. Clark, V. Balaji, S. Subramaniam, H. L. Scott, and E. Jakobsson, "Incorporation of surface tension into molecular dynamics simulation of an interface: A fluid phase lipid bilayer membrane," *Biophys. J.*, vol. 69, pp. 1230–1245, 1995.

[138] C. Hofsäß, E. Lindahl, and O. Edholm, "Molecular dynamics simulations of phospholipid bilayers with cholesterol," *Biophys. J.*, vol. 84, pp. 2192–2206, 2003.

[139] M. Patra, M. Karttunen, M. T. Hyvonen, E. Falck, P. Lindqvist, and I. Vattulainen, "Molecular Dynamics Simulations of Lipid Bilayers: Major Artifacts Due to Truncating Electrostatic Interactions," *Biophys. J.*, vol. 84, pp. 3636–3645, 2003.

[140] A. L. Hodgkin, A. F. Huxley, and B. Katz, "Measurement of current-voltage relations in the membrane of the giant axon of loligo," *J. Physiol.*, vol. 116, pp. 424–448, 1952.

[141] A. L. Hodgkin and A. F. Huxley, "The dual effect of membrane potential on sodium conductance in the giant axon of loligo," *J. Physiol.*, vol. 116, pp. 497–506, 1952.

[142] E. Hartmann, T. A. Rapoport, and H. F. Lodish, "Predicting the orientation of eukaryotic membrane-spanning proteins," *P. Natl. Acad. Sci. USA*, vol. 86, pp. 5786–5790, 1989.

[143] A. V. Samsonov, P. K. Chatterjee, V. I. Razinkov, C. H. Eng, M. Kielian, and F. S. Cohen, "Effects of membrane potential and sphingolipid structures on fusion of semliki forest virus," *J. Virol.*, vol. 76, pp. 12691–12702, 2002.

[144] A. K. Bhuyan, A. Varshney, and M. K. Mathew, "Resting membrane potential as a marker of apoptosis: studies on *xenopus* oocytes microinjected with cytochrome *c*," *Cell Death Differ.*, vol. 8, pp. 63–69, 2001.

[145] A. Filippov, G. Orädd, and G. Lindblom, "The effect of cholesterol on the lateral diffusion of phospholipids in oriented bilayers," *Biophys. J.*, vol. 84, pp. 3079–3086, 2003.

[146] R. B. Gennis, *Biomembranes. Molecular Structure and Function*.Springer Advanced Texts in Chemistry, New York, NY: Springer, 1989.

[147] E. Falck, T. Rog, M. Karttunen, and I. Vattulainen, "Lateral diffusion in lipid membranes through collective flows," *J. Am. Chem. Soc.*, vol. 130, pp. 44–45, 2008.

[148] E. Flenner, J. Das, M. C. Rheinstadter, and I. Kosztin, "Subdiffusion and lateral diffusion coefficient of lipid atoms and molecules in phospholipid bilayers," *Phys. Rev. E*, vol. 79, p. 011907, 2009.

[149] J. L. Rigaud and C. M. Gary-Bobo, "Cation diffusion selectivity in a pore model. the phosphatidylcholine/water lamellar phase," *BBA – Biomembranes*, vol. 469, pp. 246–256, 1977.

[150] M. Brändén, T. Sandén, P. Brzezinski, and J. Widengren, "Localized proton microcircuits at the biological membrane–water interface," *P. Natl. Acad. Sci. USA*, vol. 103, pp. 19766–19770, 2006.

[151] A. F. Huxley and R. Stampeli, "Evidence for saltatory conduction in peripheral myelinated nerve fibres," *J. Physiol.*, vol. 108, pp. 315–339, 1949.

[152] A. L. Hodgkin and A. F. Huxley, "Currents carried by sodium and potassium ions through the membrane of the giant axon of loligo," *J. Physiol.*, vol. 116, pp. 449–472, 1952.

[153] A. Y. Mulkidjanian, P. Dibrov, and M. Y. Galperin, "The past and present of sodium energetics: May the sodium-motive force be with you," *BBA – Bioenergetics*, vol. 1777, pp. 985–992, 2008.

[154] J. Heberle, J. Riesle, G. Thiedemann, D. Oesterhelt, and N. A. Dencher, "Proton migration along the membrane surface and retarded surface to bulk transfer," *Nature*, vol. 370, pp. 379–382, 1994.

[155] U. Alexiev, R. Mollaaghababa, P. Scherrer, H. Khorana, and M. Heyn, "Rapid long-range proton diffusion along the surface of the purple membrane and delayed proton transfer into the bulk," *P. Natl. Acad. Sci. USA*, vol. 92, pp. 372–376, 1995.

[156] Y. N. Antonenko and P. Pohl, "Coupling of proton source and sink via H^+-migration along the membrane surface as revealed by double patch-clamp experiments," *FEBS Letters*, vol. 429, pp. 197–200, 1998.

ISBN 978-952-60-3193-4
ISBN 978-952-60-3194-1 (PDF)
ISSN 1795-2239
ISSN 1795-4584 (PDF)